# Boundary Layer Velocity Structure in a Coldwater Coral Area of Haddock Channel, Southwest Grand Banks

by

© William A. Fowler
B.Sc (Physics)

A thesis submitted to the
School of Graduate Studies
in partial fulfillment of the
requirements for the degree of
Master of Science.

Environmental Science Program
Memorial University of Newfoundland

November 28, 2013

St. John's Newfoundland

# Contents

# Abstract

Gorgonian corals occur extensively at continental slope depths $> 200$ m off the southwest Grand Banks of Newfoundland. Among these corals, *Keratoisis grayi* forms gorgonian coral thickets on cobbles and boulders in otherwise muddy sand habitats. These thickets are believed to form a critical benthic habitat, in particular for juvenile fish, and as such are an integral part of the ecosystem. These coral thickets are impacted by bottom trawling activity which therefore could have far reaching consequences for the larger ecosystem. This thesis reports on a study of how the ocean bottom boundary layer is affected by the presence of coral thickets. This information is important both to establish the characteristics of coral habitat but also to demonstrate how the removal of corals modifies the boundary layer which would in turn modify the benthic environment.

Bottom boundary layer currents in coral habitat in Haddock Channel were characterized using two 2-MHz acoustic Doppler current profilers.The profilers were deployed on the seafloor at a depth of 700 m, looking upward, for 85 hours, beginning July 17th, 2007. The effective vertical profiling range was 4 meters, with 1 meter depth resolution, sampling every 2.7 minutes. One instrument was placed in an area where bamboo corals (*Keratoisis grayi*) extend approximately to 1 meter in height and occur with a density on the order of 1 colony per square meter (Coral Site). The second instrument was deployed 100 meters away in an area with visually similar

sea floor characteristics, but from which the corals had been removed by a research bottom trawl (Mud Site). Mean flow speeds at both the Mud and Coral Site are on the order of 10 cm $s^{-1}$, which is consistent with previous current data from the general area. Observed currents showed some evidence of tidal forcing but other non-linear processes clearly influence the current regime. Speed profiles were fitted to the logarithmic law of the wall to obtain bottom roughness $z_o$, and friction velocity $u_*$ estimates. Both the Mud and Coral Site appear to conform to the logarithmic law of the wall for turbulent boundary layers.

Friction velocity ($u_*$) estimates at flow speeds less than 5 cm $s^{-1}$, were consistently higher at the Coral Site, relative to the Mud Site; Mud Site $u_*$ values were $\sim$ 30% to 80% of Coral Site estimates, indicating increased turbulence due to the presence of corals. However, friction velocity increased faster with flow speed at the Mud Site, suggesting that at higher flow speeds coral induced bottom roughness is less important to friction velocity. There was significant uncertainty in bed roughness estimates, however bed roughness values at the Coral Site (mean $z_o = 0.51 \pm 0.28$ cm), were found to be generally higher at flow speeds below 5 cm $s^{-1}$, compared to the Mud Site (mean $z_o = 0.27 \pm 0.40$ cm), again possibly indicating that the coral are affecting the hydrodynamic roughness at low speeds.

Backscatter intensity was also examined as an indication of suspended organic material. It was impossible to make relative absolute comparisons between the two sites but relative changes in backscatter intensity could be compared. Backscatter levels from both sites increased as flow speeds increased, up to 7 cm $s^{-1}$. Backscatter increased faster with flow speed at the Mud Site, relative to the Coral Site, for speeds between 2.5 and 7 cm $s^{-1}$, which is broadly consistent with the suggestion of greater increase in friction velocity values seen at the Mud Site.

Above 7 cm $s^{-1}$, Coral Site backscatter intensity increased substantially, while the

corresponding Mud Site backscatter intensity declined. The reason for this change in trend is unclear, a possible explanation being a transition into a different flow regime whereby increased flow speeds interact favourably with the rough topography created by the corals. However, the large uncertainty estimates for backscatter levels at these higher speeds were such that it was very difficult to draw firm conclusions.

We conclude that higher $u_*$ and $z_o$ estimates at low flow speeds at the Coral Site, relative to the Mud Site, are consistent with the hypothesis that the enhancement of turbulence due to the coral behaving as roughness elements is significant only at low flow speeds, enabling coral polyps greater opportunities to extract organic material from the water column due to resuspension of organic material from the sea floor.

# List of Tables

# List of Figures

# Chapter 1

# Introduction

Deep-sea corals, also known as cold-water corals, are species whose habitat extends between shallow depths of 200 m to deeper than 2000 m. They are found mostly along continental slopes, seamounts, and mid-ocean ridges. Deep-sea coral species are globally distributed with habitats from coastal Antarctica to the Arctic Circle. Deep-sea coral species include representatives from both solitary and colonial scleractinian corals (stony corals), skeletal and non-skeletal octocorals (gorgonian and soft corals), and antipatharians (black corals) (*Cairns*, 2007). Unlike tropical corals, where colonies can form extensive reefs, many species of deep-sea corals exist as solitary individuals which require hard substrates such as bedrock, cobbles, or boulders (*Edinger et al.*, 2011). Groups of such individuals are referred as thickets or coral forests (dense aggregates of gorgonian coral) (*Roberts et al.*, 2009). Additionally, large reef-like structures called carbonate mounds, which consist of a sediment filled framework of carbonate material from dead corals, and live stony corals, such as *Lophelia pertusa*, have been extensively studied in the Northeast Atlantic (*Guihen et al.*, 2013; *White et al.*, 2007; *White*, 2007; *Davies et al.*, 2009; *Duineveld et al.*, 2007; **?**).

Over the last decade, the role of deep-sea corals as important components of

the deep-sea ecosystem has been well established (*Mortensen and Buhl-Mortensen*, 2004; *Friewald and Roberts*, 2005; *Mortensen and Buhl-Mortensen*, 2005a; *Gilkinson and Edinger*, 2009). Deep-sea coral species provide physical substrate, feeding sites, and shelter for many invertebrates and fish species, including both commercial and non-commercial stocks, and contribute to increased biodiversity (*Baillon et al.*, 2012; *Costello et al.*, 2005; *Edinger et al.*, 2007; *Henry and Roberts*, 2007). At the same time, there is clear evidence that deep-sea corals are highly susceptible to serious damage from human marine activities such as trawling (*Edinger et al.*, 2007; *Hall-Spencer et al.*, 2002; *Mortensen and Buhl-Mortensen*, 2005b; *Gass and Willison*, 2005). These activities are ongoing, which has added impetus to the need to further understand all aspects of coral ecology; habitat, distribution, nutrient uptake, and reproduction. This understanding is crucial in order for governments to formulate conservation policy, thereby safeguarding deep-sea corals and their habitat, and ensuring marine biodiversity (*Gilkinson and Edinger*, 2009).

Until recently, data regarding the distribution and ecology of deep-sea coral species in the Northwest Atlantic Ocean was limited (*Wareham and Edinger*, 2007). Within the last decade however, research into deep-sea coral species in Atlantic Canadian waters has increased substantially. Research efforts were initially focused on deep-water corals in Nova Scotian waters; the Scotian Shelf, the Northeast Channel, and the Sable Gully (*Breeze et al.*, 1997; *Mortensen and Buhl-Mortensen*, 2004, 2005a,b). Efforts to characterize and map the distribution of deep-sea corals in Newfoundland and Labrador waters; the Grand Banks, Northeast Newfoundland Shelf, and the Labrador shelf, have increased significantly over the past several years and are ongoing (*Baker et al.*, 2012; *Wareham and Edinger*, 2007; *Edinger et al.*, 2007; *Gilkinson and Edinger*, 2009; *Edinger et al.*, 2011). At last count, more than 45 species of deep-sea corals have been identified in Nova Scotian and Newfoundland and Labrador waters

(*Wareham*, 2009).

Characterization of the physical habitat of deep-sea corals involves examining the surficial geology of the seabed and the physical characteristics of the local water column and regional water masses, such as temperature, density, salinity, dissolved oxygen, as well as the local and regional current regimes. Many types of corals require hard substrates, therefore surficial geological features play a key role in the distribution of deep-sea corals (*Edinger et al.*, 2011). Deep-sea corals are benthic organisms, and as such, their interaction with currents in the bottom boundary layer is also an important factor in understanding many aspects of their biological and physical processes. Additionally, understanding the structure and flow of bottom currents is necessary for predicting which areas may be suitable habitat for a given coral species. The interaction of bottom currents with the characteristically rough topography of coral reefs and thickets gives rise to a turbulent bottom boundary layer (BBL). The dynamics and structure of this turbulent boundary layer play an important role in food supply and uptake, exchange of dissolved and particulate matter, larval dispersal and settlement, and sediment transport, as well as growth and productivity for many benthic organisms including corals (*Frechette et al.*, 1989; *Sebens et al.*, 2003; *Mills and Sebens*, 2004; *Ribes and Atkinson*, 2007; *Davies et al.*, 2009; *Reidenbach et al.*, 2009).

Cold-water coral areas are distinct from coastal coral reefs in that there is no mixing due to wave action and therefore the flow regime is markedly different. Previous studies of coral habitat have relied on mean current measurements, tidal data, or circulation model output to assist with evaluation of the local current regime (*White et al.*, 2005; *Mortensen and Buhl-Mortensen*, 2005b; *Bryan and Metaxas*, 2007; *White et al.*, 2007; *White*, 2007). This approach is sufficient when characterizing general habitat conditions and coral distributions over large areas, but is of limited use for

analysis of processes involving the turbulent bottom boundary layer directly (adjacent to coral). Laboratory studies involving flume tanks have been used to simulate flow dynamics and model turbulence over coral reefs (*Sebens et al.*, 2003; *Ribes and Atkinson*, 2007; *Reidenbach et al.*, 2007, 2009). However, relatively few studies have involved *in situ* direct measurements of current flows within the bottom boundary layer over the rough topography associated with coral reefs, carbonate mounds, or coral thickets (*Reidenbach et al.*, 2006a,b; *Lavaleye et al.*, 2009; *Guihen et al.*, 2013; *Khripounoff et al.*). The biological and physical processes mentioned previously are directly related to the shear and turbulent mixing in the bottom boundary layer flowing over coral areas (*Reidenbach*, 2004). Direct measurements of the current flow are therefore necessary in order to accurately characterize small scale turbulent effects. (*Grant and Madsen*, 1979, 1982; *Cacchione and Drake*, 1982; *Gross and Nowell*, 1983; *Grant et al.*, 1984; *Drake et al.*, 1992; *Cheng et al.*, 1999; *Reidenbach et al.*, 2006a). It is important to note the distinction between boundary layer studies from tropical, shallow water coral reefs (e.g. *Reidenbach et al.* (2006a, 2009)) and those from deep cold-water coral habitats (e.g. *White* (2007); *Lavaleye et al.* (2009); *Guihen et al.* (2013). While similar techniques can be used to evaluate the boundary layer dynamics, the hydrodynamic regimes can be very different. Tropical coral reefs experience strong oscillatory water motion from waves, more pronounced tidal signatures, and generally do not have strong unidirectional currents (with some exceptions). Deep-sea coral habitats on the other hand are more likely to experience strong unidirectional flows from mean currents, but tidal signatures may also be present.

## 1.1 Research Questions

The sea floor topography that arises due to the presence of coral reefs, thickets, and carbonate mounds is characteristically rough. Rough surfaces influence shear stress, drag, velocity structure, and turbulent mixing processes within the bottom boundary layer (*Cacchione and Drake*, 1982; *Drake et al.*, 1992; *Cheng et al.*, 1999). Quantifying the turbulent bottom boundary layer and frictional parameters is important in better understanding the role played by the physical structure of coral in food capture and related processes such as resuspension of sediment due to turbulent mixing.

In this thesis, the behaviour of gorgonian corals as surface roughness elements contributing to turbulence was studied through a comparison of bottom boundary layer currents over two adjacent coral habitat areas in Haddock Channel, southwest Grand Banks. Both areas present the same surficial geological features; a flat, muddy bottom with scattered cobbles, which is characterized as suitable coral habitat. Thickets of the deep-sea coral species *Keratoisis ornata* (now synonymized with *Keratoisis grayi*) are present in one area (Coral Site), but not the other (Mud Site), allowing for a comparison of the effects of coral on the turbulent bottom boundary layer. Corals are absent from the Mud Site due to one pass of a previous research bottom trawl. In fact, trawling bycatch data was used to initially identify the site as favourable for *Keratoisis grayi*, thereby strongly indicating that the two study sites are comparable in all ways except for the presence (or absence) of corals. Acoustic Doppler current profilers were deployed at both sites to study the flow structure and obtain velocity profiles. Profiles were then fitted to the logarithmic "law of the wall" for turbulent boundary layer flows to obtain values for the friction velocity (also called shear stress) and bed roughness. The two primary research questions pursued in this analysis are:

1. *Based on the values of the flow parameters, does the local bottom boundary*

*layer at the Coral Site agree with the logarithmic "law of the wall" theory which is used to describe turbulent boundary layers?*

*2. Does the presence of corals and their characteristic roughness affect the velocity profile, friction velocity, and mixing properties in a turbulent bottom boundary layer flow?*

## 1.2 Overview of Work

The work presented in this thesis is part of a larger, ongoing research project to characterize and understand the habitat, distribution, and ecology of deep-sea corals in Atlantic Canadian waters. The project is an inter-disciplinary partnership between biologists, geologists, physical oceanographers, and other marine scientists from Dalhousie University, Memorial University, and Fisheries and Oceans Canada (DFO) (*Edinger et al.*, 2011; *Edinger and Sherwood*, 2012; *Wareham and Edinger*, 2007; *Gilkinson and Edinger*, 2009; *Sherwood et al.*, 2008; *Sherwood and Edinger*, 2009; *Cogswell et al.*, 2009). The field work described in this thesis was carried out during a July 2007 cruise of the *CCGS Hudson*, which surveyed the upper continental slope off northeast Nova Scotia and the southwest Grand Banks of Newfoundland. Deployment and recovery of instruments was facilitated by the use of the remotely operated vehicle (ROV) Remote Operated Platform for Ocean Science (ROPOS) deployed from *CCGS Hudson*. Acoustic Doppler Profilers, designed for deep-sea deployment, and configured for maximum data acquisition over a short term deployment, were deployed at two locations in Haddock Channel, southwest Grand Banks (SWGB). Velocity profiles were collected in a thicket of *Keratoisis grayi* and an adjacent area with similar surficial geology but lacking corals, to determine how the characteristic roughness of the coral thicket affects the flow structure, turbulent properties, and mixing within

the bottom boundary layer.

This thesis is divided into the following chapters: Chapter 2 presents the relevant theory for boundary layer flow over smooth and rough surfaces, and provides a review of existing literature regarding both *in situ* and laboratory measurements and analysis of friction velocity, bed roughness, turbulent mixing, and the application and validation of turbulent boundary layer theory, to coral communities. Chapter 3 describes the experiment carried out in Haddock Channel, southwest Grand Banks; the instrumentation, configuration, deployment, and site characteristics, as well as data quality issues. Chapter 4 discusses the data processing methods and presents the results of the experiments including the velocity profile analysis and fitting of data to the logarithmic "law of the wall". Chapter 5 presents the results of backscatter intensity and suspended sediment analysis and the implications regarding turbulent mixing events and the availability of suspended organic material to the coral. Chapter 6 is a summary of results and conclusions and makes recommendations for further study.

# Chapter 2

# Theory and Literature Review

This chapter reviews the theory and body of research concerning the hydrodynamics and flow structure of turbulent boundary layers over rough topography, and the interaction of benthic organisms, such as corals, with the BBL. The interaction of currents and sea floor topography has been studied at scales ranging from regional circulation over the continental shelf and slope to small scale turbulence over coral reefs in shallow waters (*Armi and Robert C. Millard*, 1976; *D'Asaro*, 1982; *White*, 1994; *Reidenbach et al.*, 2006a). Interest in benthic boundary layers is related to their hydrodynamic characteristics: turbulent eddies and friction in the bottom boundary layer are important for the dissipation and transfer of energy in the form of heat and momentum from larger to smaller scales (*Kundu and Cohen*, 2004), and turbulent mixing plays an important role in the exchange of particulate and organic matter between the sea floor and water column. The topic of sediment transport and deposition due to the interaction of boundary layer flows and sea bed topography is important for understanding geological processes, pollutant transport, oceanographic engineering applications, and biological and ecological processes such as primary productivity on the continental shelf (*Grant and Madsen*, 1986). The marine sciences

are also interested in the role played by near bottom currents in influencing nutrient availability, growth, distribution of larvae, and habitat suitability for coral and other sessile benthic organisms reliant on suspension feeding mechanisms (*Frechette et al.*, 1989; *Sebens et al.*, 2003; *Mills and Sebens*, 2004; *White et al.*, 2005, 2007; *White*, 2007; *Reidenbach et al.*, 2009; *Davies et al.*, 2009; *Khripounoff et al.*). Understanding how the morphology of various coral species influences the bottom boundary layer is also an important area of research. How coral behave as roughness elements affecting the bottom boundary layer is studied on scales ranging from individual coral branches of a few millimeters in diameter, to thickets of coral a meter or two in height, and up to carbonate mounds and reefs, which can be tens of meters high, and hundreds of meters or kilometers in length (*Mortensen and Buhl-Mortensen*, 2005b; *Reidenbach et al.*, 2006a; *White*, 2007; *Monismith*, 2007; *Lavaleye et al.*, 2009; *Guihen et al.*, 2013). At all of these scales, the interaction of the roughness elements and the bottom boundary layer is critical to understanding the overall hydrodynamics.

## 2.1 Turbulent Boundary Layer Theory

The primary objective of this work is to characterize the flow regime in a deep-sea coral habitat and determine if the velocity profile and other characteristics can be understood using a turbulent bottom boundary layer (BBL) model over rough topography. Specifically, the flow within a group of coral colonies can be scaled using the logarithmic "law of the wall" which is also applied to an area without coral to provide a comparison of the flow dynamics inside and outside the coral area. The coral are treated as large scale roughness elements on the sea floor which interfaces with the bottom boundary layer. This approach has been used in other studies of turbulent flow over rough surfaces involving coral habitats (*Reidenbach et al.*, 2006a;

*Lavaleye et al.*, 2009).

According to *Kundu and Cohen* (2004), the turbulent boundary layer can be divided into two regions: an inner region comprised of a viscous sublayer closest to the wall, and an outer region where the flow is inviscid. Between the two regions, there is an overlap or inertial sublayer. It is in this layer where the logarithmic "law of the wall" is applied. The different regions of the boundary layer are described in the following sections.

### 2.1.1 Inner Region: Viscous Sublayer

In the case of a smooth wall, close to the surface, the velocity depends only on parameters that are important near the surface, therefore the overall thickness of the boundary layer $\delta$, and the free stream velocity $U_\infty$, are not important considerations. The flow is dominated by viscosity, and is referred to as the viscous sublayer (Figure 2.1). The velocity can be expressed as:

$$U = U(\rho, \tau_o, \nu, z) \tag{2.1}$$

where $\rho$ is the density of the fluid, $\tau_o$ is the shear stress at the wall, $\nu$ is the kinematic viscosity, and $z$ is the height above the boundary. In terms of a dimensional analysis of the parameters involved, only $\tau$ and $\rho$ involve units of mass, so to acquire the dimensions for velocity it is necessary to combine these parameters. The ratio of shear stress to fluid density gives

$$u_* \equiv \sqrt{\frac{\tau_o}{\rho}} \tag{2.2}$$

which has the dimensions of velocity and is called the friction velocity, also referred as the shear velocity. The friction velocity is the primary velocity scale for turbulent

boundary layer flows (*Kundu and Cohen*, 2004). Because it has units of velocity, $u_*$ allows for the comparison of shear or drag due to the surface with the actual flow velocities in the boundary layer flow.

The velocity distribution can be expressed as a function of the viscosity, the friction velocity, and the height above the surface:

$$\frac{U}{u_*} = f(\frac{zu_*}{\nu}) = f(z^+) \tag{2.3}$$

where $z^+ \equiv zu_*/\nu$, is the distance from the surface or boundary normalized by the viscous scale $\nu/u_*$. Equation 2.3 is called the "law of the wall" for the viscous sublayer. The stress in the viscous sublayer is uniform and equal to the wall shear stress $\tau_o$. The velocity distribution is uniform and linear over the sublayer. Experimental evidence shows that the linear velocity distribution holds for distances up to $z\nu/u_* \sim 5$ (Figure 2.1), which is taken as the limit of the viscous sublayer (*Kundu and Cohen*, 2004).

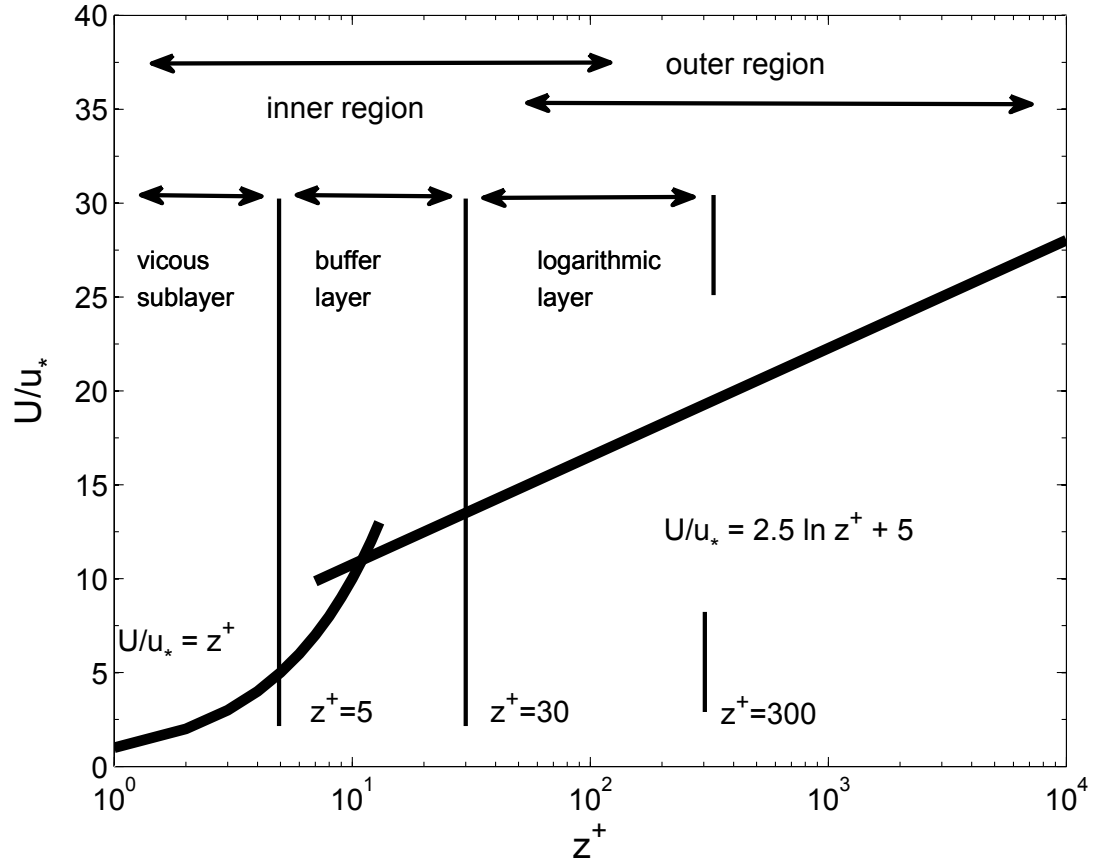


Figure 2.1: The Law of the Wall and the various regions of the boundary layer, after *Kundu and Cohen, 2004.*

### 2.1.2 Outer Region: Velocity Defect Law

The outer region of the flow is generally independent of viscosity, and turbulent effects are the dominant factor. Far from the boundary, the velocity distribution approaches the free stream velocity $U_\infty$. However, drag on the flow due to Reynolds stresses generates a velocity defect $(U_\infty - U)$, which is proportional to the friction velocity $u_*$. The velocity distribution in this region is dependent on the thickness of the boundary layer $\delta$, and the distance from the surface:

$$\frac{U_\infty - U}{u_*} = f(\frac{z}{\delta}) \tag{2.4}$$

Equation 2.4 is referred to as the velocity defect law.

### 2.1.3 Overlap Layer: Logarithmic Law of the Wall

The velocity distributions in the inner and outer regions are dominated by different scaling factors; the boundary layer thickness $\delta$, in the case of the outer region, and the viscous scale $\nu/u_*$, in the inner region. However, there is a region of overlap between the two layers where the solutions to Equations 2.3 and 2.4 must be matched.

The velocity distribution for this layer takes the following form as shown in *Kundu and Cohen* (2004):

$$U(z) = \frac{u_*}{\kappa} ln(\frac{z u_*}{\nu}) + \mathbb{K} \tag{2.5}$$

where $\kappa$ is a dimensionless constant called von Kármán constant used to describe the logarithmic velocity profile of a turbulent flow near a boundary ($\kappa = 0.41$), and $\mathbb{K}$ is a constant of integration. For a smooth flat surface, experiments show that $\mathbb{K} = 5$. Equation 2.5 is valid for $30 < z^+ < 300$ (Figure 2.1) i.e. for large $z^+$ and small $\frac{z}{\delta}$, and is called the logarithmic law of the wall. The velocity at any point in this layer is proportional to the logarithm of the distance of that point from the boundary. This area is referred to as the overlap or logarithmic layer, and alternatively, as the inertial sublayer, owing to the fact that turbulent effects dominate (*Kundu and Cohen*, 2004).

### 2.1.4 Buffer Layer

Between the viscous sublayer and the overlap (logarithmic) layer there is a region referred to as the buffer layer from $5 < z^+ < 30$ (Figure 2.1). In the buffer layer the

velocity distribution is neither linear nor logarithmic. Neither the viscous stress nor Reynolds stress are negligible here.

### 2.1.5 Hydrodynamically Rough Surfaces

The flow in the inner region is assumed to be viscous, resulting from a hydrodynamically smooth surface in which the average height of roughness elements is smaller than the height of the viscous sublayer. However, when the average height of the roughness elements becomes larger than the thickness of the viscous sublayer, the surface can be characterized as hydrodynamically rough, and viscosity no longer becomes an important scaling parameter. Wakes form behind each roughness element and the resulting drag transmits stress to the surface (*Kundu and Cohen*, 2004). As in the previous case, the flow is still logarithmic in nature, but the velocity distribution is no longer viscosity dependent.

A general form of the logarithmic law of the wall, given in (*Kundu and Cohen*, 2004), is

$$U(z) = \frac{u_*}{\kappa} ln(z) + \mathbb{K}. \tag{2.6}$$

The constant of integration can be adjusted to yield Equation 2.5 for the case of a smooth surface.

In the case of a rough surface, the constant of integration is determined by noting that the mean velocity *U(z)* is expected to go to zero within the roughness elements, $z_0$ is therefore defined as the characteristic height of the roughness elements and the distance from the surface at which the velocity goes to zero (Figure 2.2).

Setting $U = 0$ at $z = z_o$ in Equation 2.6 and rearranging to solve for the constant of integration gives

$$\mathbb{K} = -\frac{u_*}{\kappa} ln(z_o). \tag{2.7}$$

Equation 2.6 can then be rewritten as

$$U(z) = \frac{u_*}{\kappa} ln(z) - \frac{u_*}{\kappa} ln(z_o) \tag{2.8}$$

or

$$U(z) = \frac{u_*}{\kappa} ln(\frac{z}{z_o}) \tag{2.9}$$

Equation 2.9 is the logarithmic law for a turbulent boundary layer over a rough surface. The characteristic roughness height $z_o$ which depends on the effective size of roughness, and the friction velocity $u_*$ which, as noted, identifies the magnitude or intensity of the turbulent velocities, are the only important scaling parameters, and the velocity distribution becomes independent of viscosity.

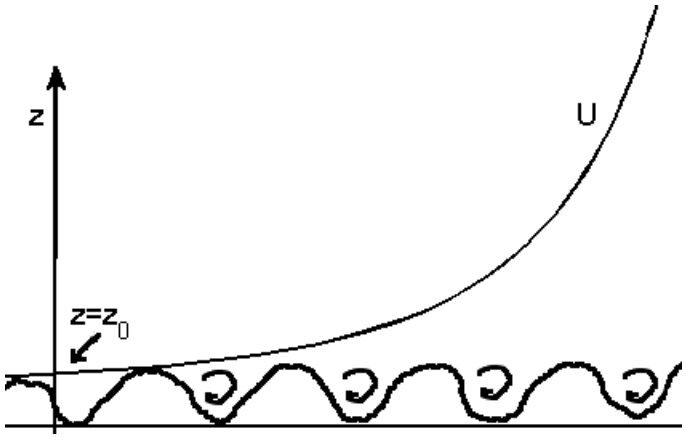


Figure 2.2: Logarithmic velocity distribution over a rough surface with wakes and eddies formed behind each roughness element. The mean velocity goes to zero at $z = z_0$. After *Kundu and Cohen, 2004*.

## 2.2 Logarithmic Boundary Layer

Using the bottom boundary layer theory presented it is possible to interpret velocity profiles for flows over rough surfaces using *in-situ* field measurements and Equation 2.9. Estimates of friction velocity and bed roughness can then be obtained. If the horizontal velocity $U(z)$, is plotted as a function of height above the bottom $ln(z)$, then the slope of the line will be $\frac{u_*}{\kappa}$ and the intercept on the z-axis will be $ln(z_0)$. This method for estimating friction velocity and bed roughness is alternately referred to as the log-profile technique, logarithmic law technique, the von Karman-Prandtl logarithmic expression, or simply the law of the wall technique (*Cacchione and Drake*, 1982; *Gross and Nowell*, 1983; *Grant et al.*, 1984; *Frechette et al.*, 1989; *Reidenbach et al.*, 2006a; *Guihen et al.*, 2013). Both *Gross and Nowell* (1983) and *Frechette et al.* (1989) note that this approach assumes equilibrium flow conditions where the boundary layer is self-similar. *Gross and Nowell* (1983) also note that in this steady state approach, it is assumed that the "adjustment of turbulent shear stress to changes in the mean velocity profile will be fast enough that the mean and turbulent quantities will always scale together through the friction velocity."

Experiments involving the application of the log-profile technique to oscillatory flows such as tidal boundary layers have been carried out to determine over what time scales the flow could be described as steady state for the purposes of obtaining logarithmic velocity profiles through various averaging periods (*Gross and Nowell*, 1983). In flow regimes involving wind forcing, wave-current interactions, internal waves or other oscillatory states with large spatial or temporal gradients, the velocity profile cannot be assumed to be constant and more complex wave-boundary layer coupled models are used (*Grant and Madsen*, 1979, 1986; *Drake et al.*, 1992). In the experiments described in this thesis the current flow regime is considered steady over

the data averaging period and can be described using the logarithmic law technique.

### 2.2.1 Boundary Layer and Benthic Interaction

The interaction of turbulent bottom boundary layer currents with the rough topography of the sea bed plays an important role in the biological and physical processes of many benthic organisms including coral colonies, thickets, reefs, and carbonate mounds (*Davies et al.*, 2009; *Duineveld et al.*, 2007; *Khripounoff et al.*). When the uptake of particulate matter by suspension feeders is very high, it is possible for a particle-depleted layer to form within the momentum boundary layer adjacent to the benthos (*Ribes and Atkinson*, 2007). Both downward fluxing and resuspended sediments and organic material have been shown to be a food source for coral, therefore resupply of organic material may be dependent on both vertical diffusion due to turbulent mixing, and increased horizontal transport due to higher current speeds (*Frechette et al.*, 1989; *Mills and Sebens*, 2004; *Wheeler et al.*, 2008). Bottom roughness is an important factor governing turbulent eddy diffusion in the bottom boundary layer. Increased bottom roughness (and increased $u_*$) will therefore increase turbulent mixing and thus contribute to the transport and resuspension of food to corals (*Frechette et al.*, 1989; *Davies et al.*, 2009). The bottom topography associated with coral reefs and carbonate mounds have been shown to enhance turbulent mixing, drag, and friction velocity, over both the reef scale and the local colony level, allowing coral and other reef organisms to more effectively exchange dissolved and particulate matter with the water column (*Reidenbach et al.*, 2006a; *Wheeler et al.*, 2008). Because friction velocity is directly proportional to the mean current speed (Equation 2.9), increased current speeds can also lead to in an increase in drag over a coral area and result in further turbulent mixing and resuspension of suspended organic material

(*Reidenbach et al.*, 2006a).

### 2.2.2 Corals in Atlantic Canada

Deep-sea corals in Atlantic Canada have received increased attention due to an increased appreciation of their contribution to the biodiversity of marine ecosystems, and the need for conservation measures to protect against ongoing damage from fisheries and other human activities. As of 2013, over 60 deep-sea coral species have been identified in Atlantic Canadian waters (*Cogswell et al.*, 2009; *Wareham*, 2009). Most coral species have been located at depths $> 200$ m, mainly along the continental shelf edge and continental slope (*Wareham and Edinger*, 2007). Study has focused on submarine canyons and deep channels such as The Gully, the Northeast Channel, and the Stone Fence in the Maritimes region (see Figure 2.3), where multiple coral species have been located (*Mortensen and Buhl-Mortensen*, 2005a, 2004; *Gass and Willison*, 2005). Such areas are considered good coral habitat, in part, because they are associated with strong currents which remove or prevent sediment build up, thereby exposing harder substrates (*Wareham and Edinger*, 2007; *Edinger et al.*, 2011). The strong currents also transport fine particulate organic matter which is important for suspension feeding coral (*Wareham and Edinger*, 2007). *Mortensen and Buhl-Mortensen* (2005b) noted "that the pattern and velocity of currents are important factors in determining the abundance and shape of certain types of deep-sea corals, particularly gorgonians." Current measurements recorded in the Northeast Channel, which crosses the Scotian Shelf between Browns Bank and Georges Bank (a rich fishing ground), are on the order of 40-60 cm $s^{-1}$ with mean maximum velocities near 1 m $s^{-1}$ , which is largely due to strong semidiurnal tidal currents (*Mortensen and Buhl-Mortensen*, 2005b; *Metaxas and Davis*, 2005). Generally, the coral habi-

tat protected to date in the Maritimes is characterized by strong currents and hard substrates.

The creation of Atlantic Canada's first Marine Protected Area (MPA), The Gully MPA, located off the coast of Nova Scotia near Sable island (see Figure 2.3), under the federal *Oceans Act*, originally intended to protect Northern Bottlenose Whales, also benefits the numerous deep-sea coral species found in the Gully which contribute to the region's biodiversity. Further research and the discovery of other coral hotspots has lead to fisheries closures in two additional areas in the Maritimes Region (The Northeast Channel, and the Stone Fence) specifically as coral conservation zones (*Breeze and Fenton*, 2007).

The distribution of coral species off the coast of Newfoundland and Labrador were mapped by *Wareham and Edinger* (2007) and *Edinger et al.* (2007) based on coral samples and fisheries bycatch records obtained between 2000-2007. Data were compiled from Department of Fisheries and Oceans multi-year fisheries and scientific survey reports listing coral bycatch, and more recently through the use of *in situ* video footage obtained using the ROPOS ROV (*Edinger et al.*, 2007; *Baker et al.*, 2012). Forty-five coral species have been documented and mapped in Newfoundland and Labrador and adjacent Arctic waters (*Wareham*, 2009). The distribution of large gorgonian coral species, a subset of the Order Alcyonacea off the coast of Newfoundland and Labrador is shown in Figure 2.3.

Unlike the Maritimes region, there are currently no permanent measures in place to protect deep-sea coral habitat in Newfoundland and Labrador waters (i.e. no existing Marine Protected Areas or Fishery Closures). There are now however numerous coral closure zones in place outside of Canada's Exclusive Economic Zone (EEZ) in which bottom trawling and any other commercial fishing activity involving the sea bed are prohibited. These zones have been established by the North Atlantic Fish-

eries Organization (NAFO). Within Newfoundland and Labrador waters there is a fishing industry led coral protection zone in the Northern Labrador Sea. Also in Newfoundland waters is the *CAD-NAFO Coral Protection Zone*, a mandatory temporary closure, jointly agreed upon by the Canadian government and NAFO, originally implemented in 2007, which was due to expire at the end of 2012 but has now been renewed until December 31, 2014. The zone is located on the slope of the Grand Bank in NAFO regulatory division 3O between 800-2000 m, encompassing an area of 14,040 $km^2$, see Figure 2.3.

In Newfoundland and Labrador waters, deep-sea corals are located with greatest density at the mouths of shelf-crossing troughs on the Grand Banks, Northeast Newfoundland Shelf, and Labrador Shelf (*Edinger et al.*, 2011). The most common large gorgonian species in Newfoundland and Labrador waters are *Keratoisis ornata* (now synomized with *Keratoisis grayi*, and *Paramuricea* spp. (a mix of *Paramuricea placomus* and *Paramuricea grandis*). Unlike *Primnoa* and *Paragorgia*, the dominant large gorgonian species in key coral areas of the Maritimes, *Keratoisis* (also found in high-current settings elsewhere) is thought to better tolerate the low-current regimes which characterize several coral hot spots in Newfoundland waters (*Edinger et al.*, 2011), its range also extends deeper than either *Primnoa* or *Paragorgia*.

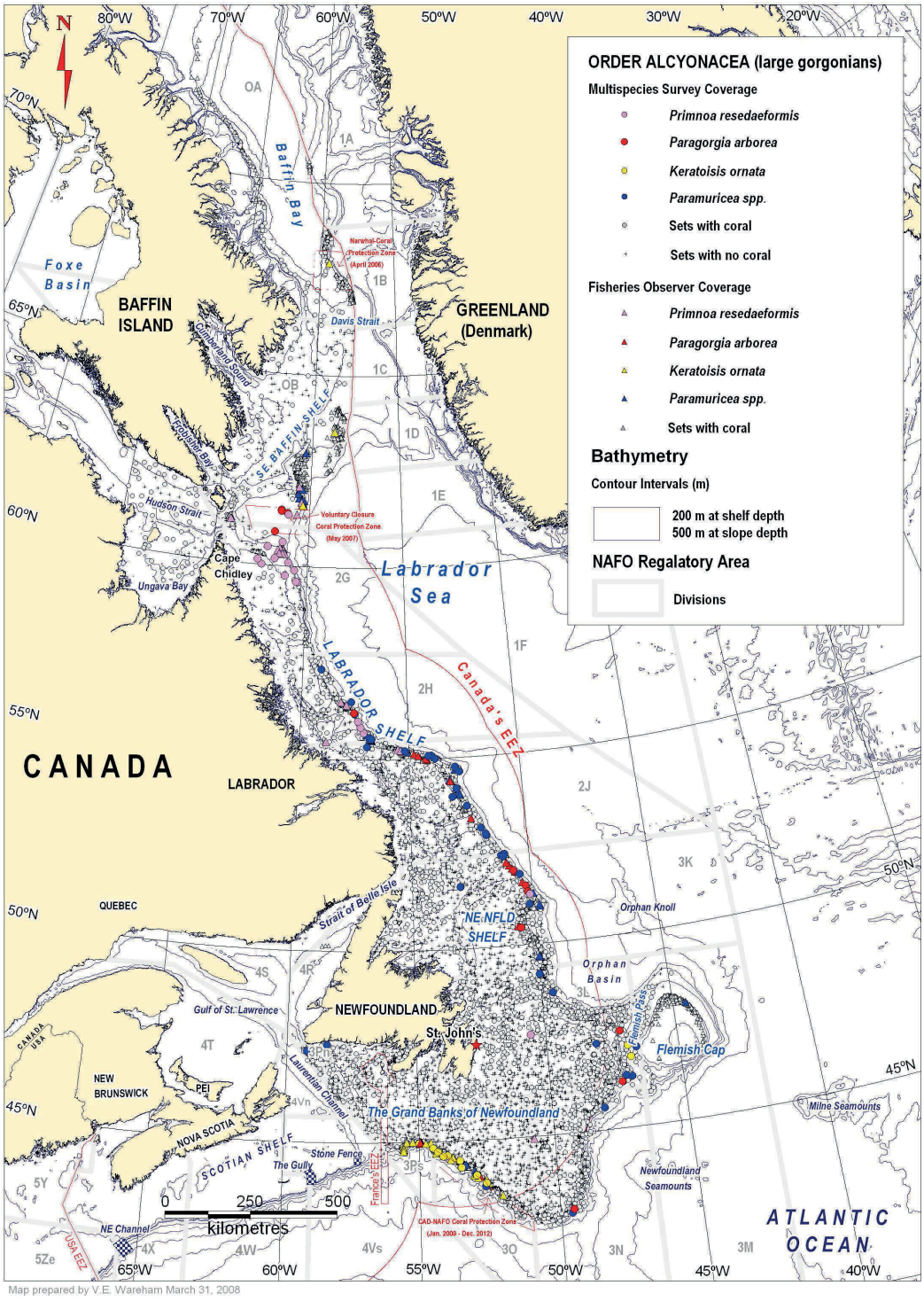


Figure 2.3: Distribution of deep-sea corals from the Order Alcyonacea (large gorgonians) off the coast of Newfoundland and Labrador. Data was compiled from multiple fisheries surveys between 2000-2007. Map prepared by V.E. Wareham, May 2010, based on maps in *Wareham* (2009), used with permission.

# Chapter 3

# Experimental Site Characteristics and Instrumentation

This chapter describes instrument deployments carried out in Haddock Channel, on the slope of the southwest Grand Banks (SWGB), approximately 250 km south of Newfoundland in mid July, 2007. Two Doppler profilers were deployed on the sea bed via the ROPOS (Remotely Operated Platform for Ocean Science) ROV operated from the Canadian Coast Guard vessel Hudson, during a two week research cruise (2007 ROPOS Discovery Cruise, hereinafter ROPOS 2007). The instruments were deployed to characterize the turbulent benthic boundary layer (BBL) in a coral thicket as part of a larger, ongoing study of the ecology of deep-sea corals off the coast of Newfoundland and Labrador (*Gilkinson and Edinger*, 2009).

Section 3.1 gives a basic overview of Haddock Channel, southwest Grand Banks, with respect to deep-sea corals. Section 3.2 discusses St. Pierre Bank, which was used as a predictor of general flow conditions prior to deployment. Section 3.3 explains the Doppler Effect and the instrumentation specifications used during the experiments. Section 3.4 discusses instrument mounting on specially designed settlement plates,

instrumentation configurations, and deployment procedures. Section 3.5 provides details on the specific site characteristics. Finally, Section 3.6 addresses troubleshooting issues that were encountered during the deployment as well as recommendations for future deployments.

## 3.1 Haddock Channel, Southwest Grand Banks

Haddock Channel, located on the slope of the southwest Grand Banks, was chosen for the deployment of Doppler Profilers during the ROPOS 2007 cruise due to the presence of large gorgonian corals, which were known to exist in the area based on previous coral distribution studies (*Edinger et al.*, 2007). Specifically, clusters of *Keratoisis grayi* colonies, known as thickets, were present in the channel. Gorgonians such as *Keratoisis*, are characterized by rigid to semi-flexible skeletons which are composed of calcium carbonate branches with joints made up of a protein called gorgonin. *Keratoisis ornata* (order *Alcyonacea*, family *Isididae*), commonly referred to as bamboo coral, are colonial octocoral which attach themselves to hard substrates such as bedrock, cobbles or boulders. They can range in height from tens of centimeters to 1.5 m. *Keratoisis* are suspension feeders; each coral polyp contains eight tentacles that are used to capture prey such as plankton or particulate matter suspended in the water column, which is carried into range by the local currents, turbulent eddies, or falls down from the above water column.

The location of *Keratoisis* thickets in Haddock Channel, southwest Grand Banks (NAFO Div. 3Ps), that were explored during the ROPOS 2007 cruise are shown in Figure 3.1. They are located just outside the *CAD-NAFO Coral Protection Zone* (NAFO Div. 3O) and are therefore still susceptible to damage from commercial fishing activity (*Gilkinson and Edinger*, 2009).

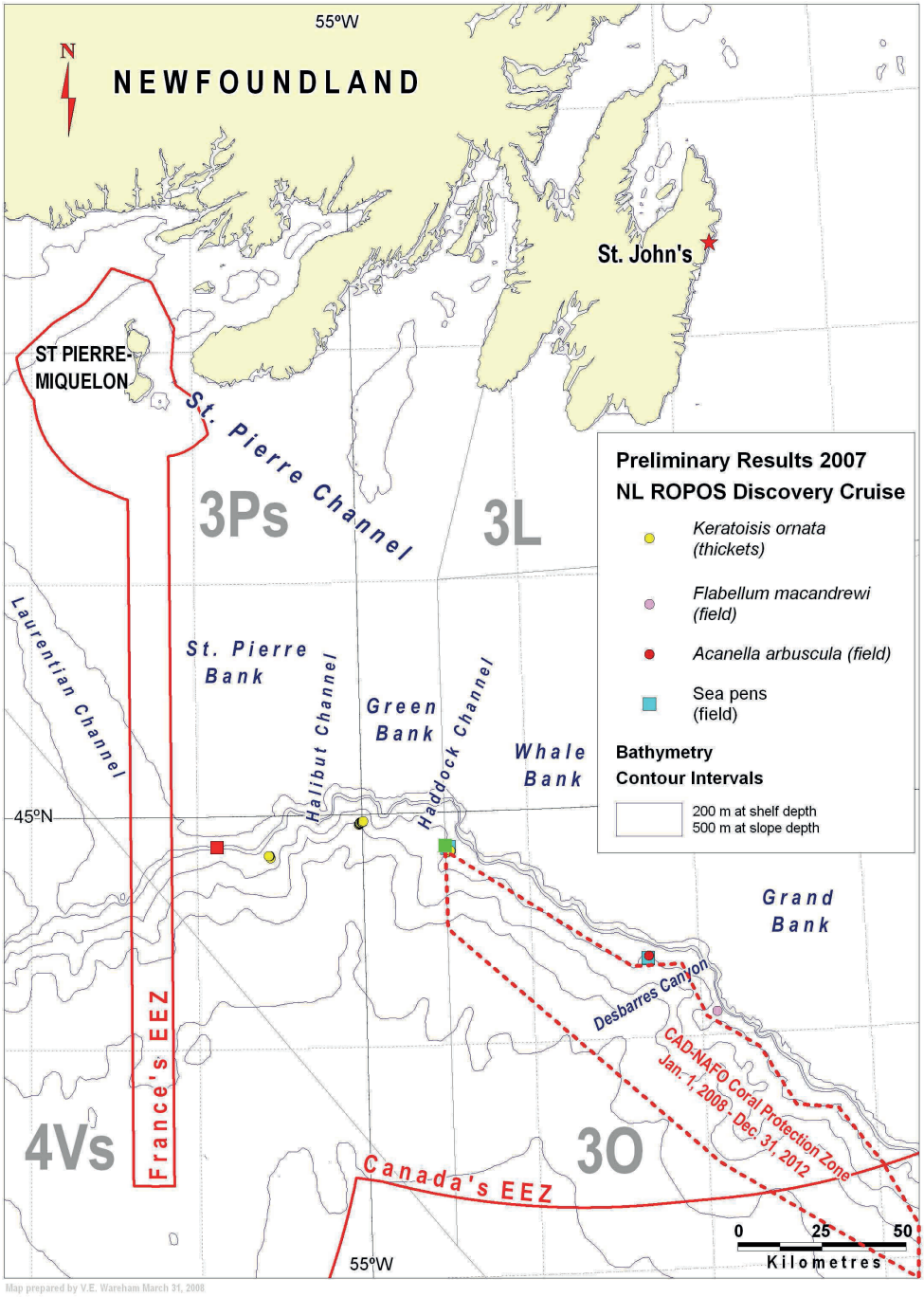


Figure 3.1: Preliminary results of unique deep-sea coral habitats on the southwest Grand Banks from NL ROPOS Discovery Cruise (2007). Locations of undisturbed thickets of *Keratoisis ornata* Haddock Channel,outside the CAD-NAFO Coral Protection Zone. The green square represents the deployment area for the two Doppler profilers used in the field measurements discussed in this thesis. The red square represents the location of a previous DFO current meter deployment to St. Pierre Bank. Map prepared by V.E. Wareham, May 2010, based on maps in *Wareham* (2009), used

## 3.2 St. Pierre Bank Currents

As part of the cruise planning stage, current measurements from the nearest available station - St. Pierre Bank, were obtained from the Science Branch of DFO in order to get preliminary estimates of the local current regime in the Haddock Channel area. St. Pierre Bank, 44.83 N, 55.83 W, is approximately 100 km west of Haddock Channel, the location of the St. Pierre Bank current meter is denoted by a red square in Figure 3.1. A current record from an Aanderaa current meter, deployed from April 29th to November 19th, 2000, at a depth of 683 m is shown in Figure 3.2. The mean speed at this location was 3.6 cm $s^{-1}$, with a maximum speed of 18 cm $s^{-1}$. Because of the design of the Aanderaa RCM-8 current meter, the instrument is unable to register speeds below a minimum starting speed which accounts for the visible data cutoff at 1.1 cm $s^{-1}$ in the speed plot. The dominant current direction was southwest, with a tidal component in the southwest/eastward directions. The temperature record indicates suitable conditions for cold water coral. We anticipated that these observations were representative of velocities we expected to see at the Haddock Channel location.

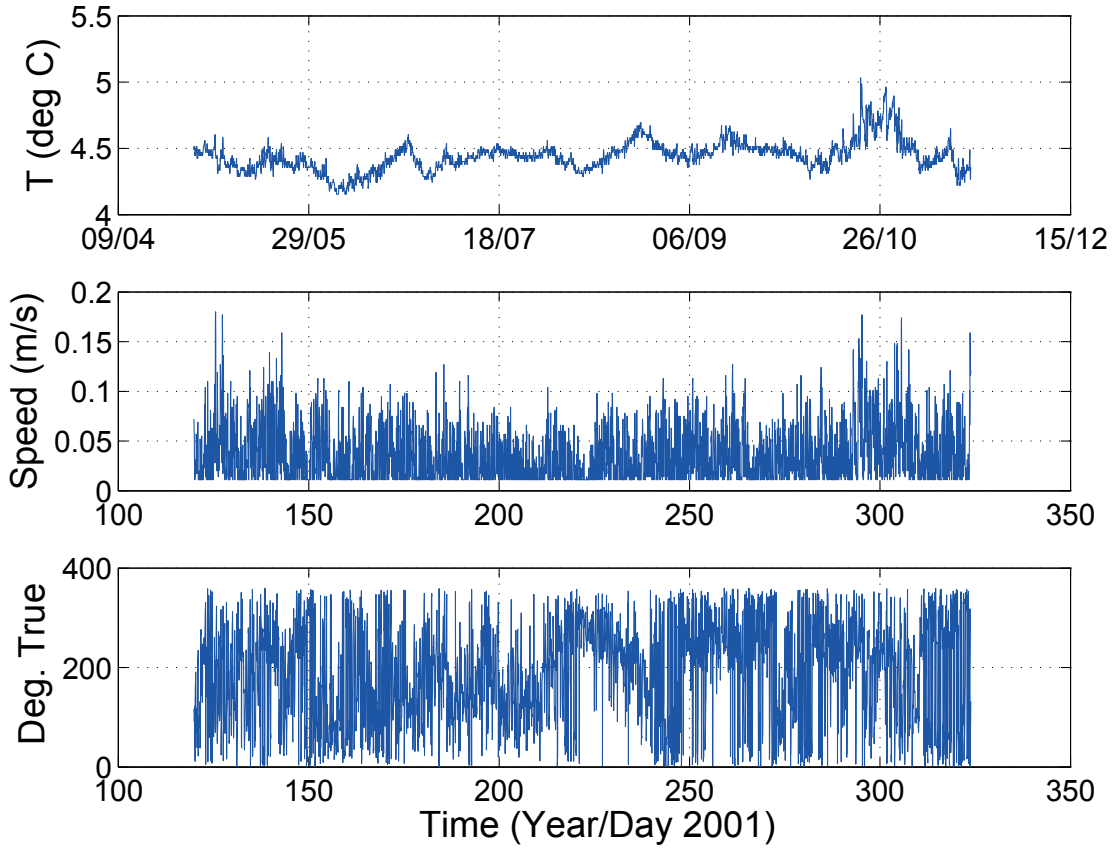


Figure 3.2: Time series of (a) temperature, (b) speed, and (c) current direction (heading) on St. Pierre Bank during the period 29 April - 19 November, 2000. Data from an Aanderaa current meter, deployed at a depth of 683 m, maximum depth at station is 703 m.

## 3.3 ROV and Instrumentation

### 3.3.1 ROPOS Remotely Operated Vehicle

The deployment of instruments and visual survey of the Haddock Channel coral thickets was carried out using the ROPOS (Remotely Operated Platform for Ocean Sciences) ROV, shown in Figure 3.3, which is owned and operated by the Canadian Scientific Submersible Facility of Victoria (North Saanich), BC. The ROPOS ROV is a 40 HP science/work class ROV, it is a tethered vehicle which is controlled and powered from a mobile operating station onboard CCGS Hudson. ROPOS can be configured for maximum dive depths of 1000, 3000 and 5000 m depending on the mission requirements. The ROV is equipped with an array of video and still cameras as well as two hydraulically powered, robotic manipulator arms which can perform various tasks such as sample collection and instrument placement. In the mid-depth dive configuration the ROV weighs 2400 kg.


Figure 3.3: The ROPOS ROV deployed from CCGS Hudson, July 17, 2007. Doppler Profilers are attached to ROPOS for deployment to the sea floor.

### 3.3.2 Doppler Current Profilers

Doppler current profilers were used during this experiment. Acoustic transducers transmit short pulses of sound (pings) at a constant frequency into the water. As these pulses radiate through the water column they encounter sound scatterers such as particles of sediment, organic material, or plankton, which are suspended in and assumed to move at the same speed at the water. These scatterers reflect a portion of the outgoing pulse back to the transducer. The portion of the pulse which is reflected to the transducer is Doppler shifted in frequency due to the relative motion between the scatterer and the instrument. The Doppler shifted frequency $f_d$, according to *Medwin and Clay* (1998) is given as

$$f_d = 2f_t\frac{v}{c} \tag{3.1}$$

where $f_t$ is the frequency of the transmitted pulse at the transducer, $v$ is the relative velocity between the sound source and receiver, and $c$ is the speed of sound in water. The frequency shift of the backscatter is then used to calculate the relative velocity of the scatterers and therefore the velocity of the current. The factor of two in the equation arises because the scatterer behaves as both a receiver and a transmitter of the sound pulses which are, in a sense, Doppler shifted twice. Doppler profilers typically use three or four transducers which necessarily point in different directions. Each transducer beam measures a different component of the water velocity parallel to the major axis of the acoustic beam. Data from multiple beams are therefore required to reconstruct the velocity of the current. Since echoes or backscatter from scatterers at different distances in the water column arrive back at the transducer at different times, the instrument can sort data into depth cells (bins), a method known as range gating, and therefore create velocity profiles over a range of different depths.

The choice of transducer frequency is an important consideration in choosing the correct Doppler profiler for use in a given experiment. While higher frequencies provide higher spatial resolution because of higher bandwidth, sound attenuation increases with frequency thereby decreasing the profiling range. Lower operating frequencies increase the profiling range of the instrument since lower frequency sound travels further and suffers less attenuation. Critically, the choice of transducer frequency is a compromise between spatial resolution and profiling range. Depending on the application, one may desire to profile a large portion of the water column (i.e. hundreds of meters), with relatively low spatial resolution, 2 to 4 meter bins using frequencies of several hundred kHz, or a small section of the water column, on the order of tens of meters or less, with smaller depth cells of 1 meter to tens of centimeters, with frequencies in the higher kHz or MHz range.

Another important consideration is the nature and quantity of backscatterers present in the water column. More backscatterers provide increased signal intensity as more of the outgoing signal is reflected back, and these associated higher signal levels enable greater profiling ranges. Conversely, insufficient backscatter concentrations results in lower signal intensity which leads to reduced profiling range.

### 3.3.3 Nortek Aquadopp Profiler

The Nortek 2 MHz Aquadopp Doppler profilers used in the Haddock Channel experiment are high resolution instruments designed for stationary deployments on the sea floor, for use on moorings or other fixed structures, or attached to buoys. They were chosen specifically for their ability to operate in deep sea environments; the operational maximum depth rating is 2000 m. The instrument uses three acoustic transducers with beams slanted at 45° to vertical, sending pings at a frequency of

2 MHz. Sample bin size was set at 1 m, with a blanking distance of 0.20 m. The blanking distance is the minimum distance away from the instrument for which measurements can be obtained due to the requirement of the transducer to completely relax after transmitting an outgoing pulse before listening for incoming backscatter signals. The accuracy stated by Nortek is 1% of the measured value or ± 0.5 cm $s^{-1}$. The maximum profile range for these profilers is 4 to 8 meters depending on the turbidity of the water being sampled, with acoustically turbid water offering better range than clear water due to availability of acoustic scatterers. Profilers can be configured to output velocity in Beam, XYZ, or East North Up (ENU) coordinate axis, conversion between coordinate systems is discussed in Chapter 4. The profilers are equipped with standard sensors including an embedded thermistor for temperature, an internal compass, tilt sensor, and pressure sensor.

## 3.4 Experiment

### 3.4.1 Settlement Plates and Instrument Mounting

The two Nortek Aquadopp 2-MHz Doppler profilers (AQD1 and AQD2) were deployed on July 17, 2007, via the ROPOS ROV and recovered on July, 21, 2007. Both profilers were configured for high duty cycles meaning a higher sampling rate which resulted in increased power consumption and shorter battery life. Each profiler was coupled to the side of a stainless steel box, referred to as a settlement plate (Figures 3.4 and 3.5). The settlement plate with attached Doppler profiler is 121 cm long, 45 cm wide, and 30 cm in height. The settlement array (grid of twelve steel plates) was originally intended to serve as platform for an extended biological study of coral polyp grown on various substrate types which were to be attached to the plates. Due

to the short nature of the profiler deployment, the biological experiment was carried out on several stand-alone settlement arrays which were placed in the same coral thicket (*Baker et al.*, 2009). The basic experiment configuration, shown in Figure 3.6, involved placing a Doppler profiler within a coral thicket to measure any possible effects on the bottom boundary layer due to the presence of coral, which might impede or create drag on the flow.

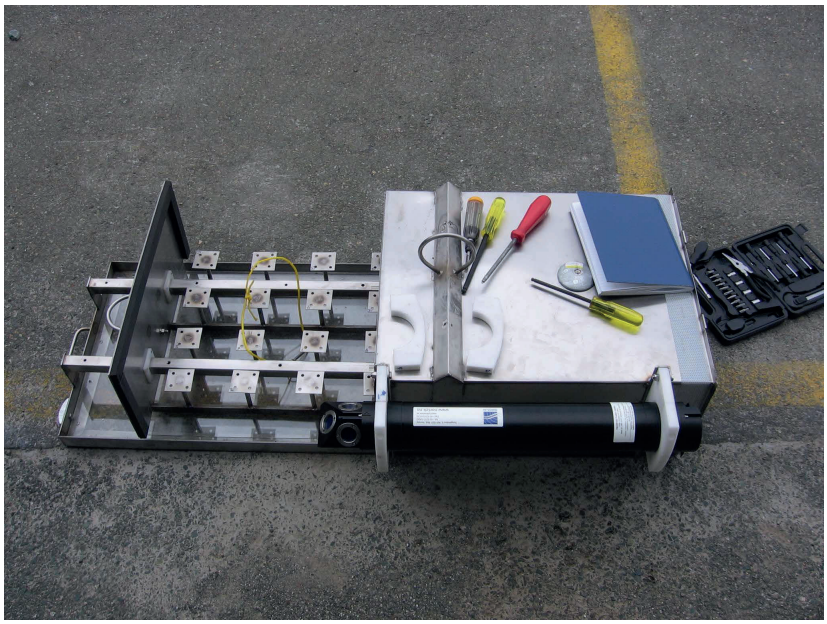

Figure 3.4: Settlement plate with Nortek Aquadopp 2 MHz Doppler profiler at the Ocean Sciences Centre, Logy Bay, Newfoundland, during initial fitting of the profilers and settlement plates. The settlement plate with attached Doppler profiler is 121 cm long, 45 cm wide, and 30 cm in height. The settlement plate was originally designed for remote recovery by acoustic release, which would protect the settlement substrates inside the large stainless steel box.

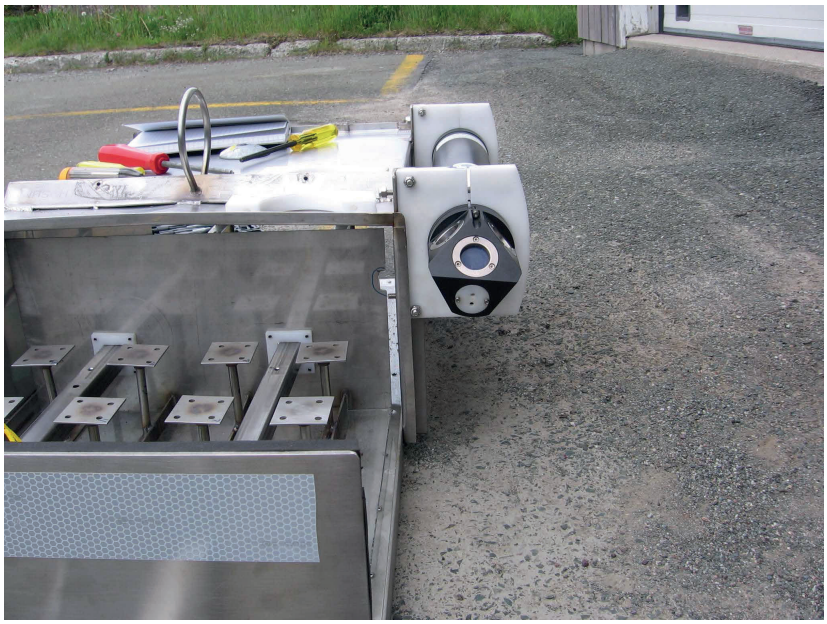

Figure 3.5: Front view of the Nortek Aquadopp profiler mounted on the side of the settlement plate box. The Aquadopp's transducer head is 26 cm above the bottom of the box.

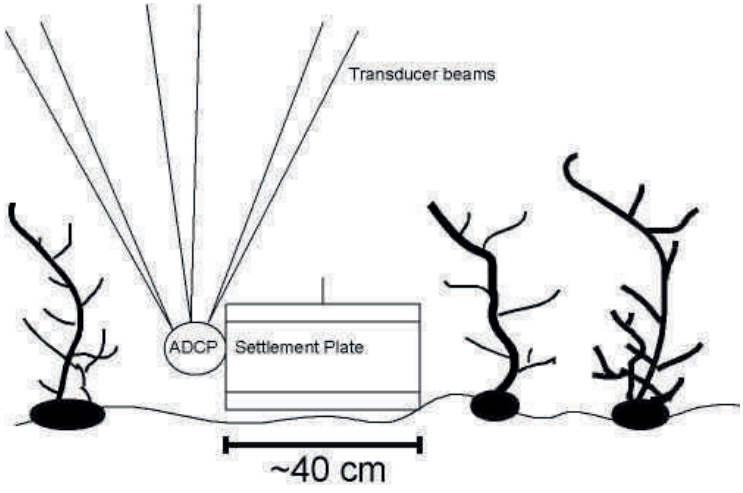


Figure 3.6: Basic deployment concept: the upward looking Doppler profiler, labeled ADCP, is mounted on a settlement plate which is positioned on the sea floor inside a coral thicket. The instrument's transducer beams then record velocity profiles within the bottom boundary layer and any potential influence on the flow regime due to the presence of the coral structures.

### 3.4.2 Instrument Configuration

The instrument's sampling rate was one velocity profile every 5 seconds (later post deployment averaging reduced this to one profile every 2.7 minutes). The bin size was programmed for 1 m, with 8 bins in total, and a blanking distance of 20 cm. Velocity measurement were recorded in Beam coordinates; the instrument measures velocity components parallel to the direction of the transducer beams. Velocity measurements were transformed post-deployment into East North Up (ENU) coordinates using MatLab code provided by Nortek USA.

### 3.4.3 Deployment Procedure

The choice of Haddock Channel as the deployment location was based upon high bycatch of *Keratoisis ornata* in several DFO survey trawls, specifically the deployment target was chosen midway along the path of a 0.8 mile trawl that recovered *K. ornata*. The two deployment sites, denoted by the green square in Figure 3.1, within Haddock Channel were then selected based upon visual assessment using real time video feed from the ROPOS ROV. Aquadopp profilers were carried down to the sea floor via ROPOS on July 17, 2007. The area of sea bed where the ROV reached the bottom was characterized as suitable coral habitat, but devoid of corals, the first Doppler profiler (AQD1) was positioned here. A coral thicket comprised of multiple, large *Keratoisis* individuals, was discovered approximately 100 m from the location of AQD1 during the same transect. The second Doppler profiler (AQD2) was positioned amongst the corals, to study the effects of coral on the bottom boundary layer. Both sites are located at a depth of approximately 700 m. The coordinates, deployment duration, and depths for both sites are listed in Table 3.1. AQD1 was deployed at the site lacking corals, which was used as a control or reference site, and subsequently referred to as

the Mud Site. AQD2 was deployed in the coral thicket, referred to as the Coral Site, with the front of both settlement plates facing due North. The Doppler profilers were approximately 26 cm off the sea bed. Total deployment time for each instrument was ∼85 hours.

| Site Name | Lat. | Long. | Deployment Date | Recovery Date | Depth (m) |
|---|---|---|---|---|---|
| Site 1: Mud Area | N 44 49.8023 | W 54 29.0484 | 17/07/2007 17:10 UTC | 21/07/2007 17:24 UTC | 707 |
| Site 2: Coral Thicket | N 44 49.7639 | W 54 29.1070 | 17/07/2007 21:10 UTC | 21/07/2007 17:30 UTC | 696 |

Table 3.1: Location and Depth of Doppler Profiler Deployments in Haddock Channel, July 2007.

## 3.5 Site Characteristics

The location of Aquadopp profiler AQD1, referred to as Mud Site, shown in Figure 3.7, is at a depth of 707 m. The site is typical of the topography of Haddock Channel; the sea bed is flat, with no large surface features. The substrate consists of dense mud, silt, and cobbles. The area is devoid of coral, and as such was chosen as a suitable control or reference site to characterize the local bottom boundary layer, free from the potential effects of coral thickets.

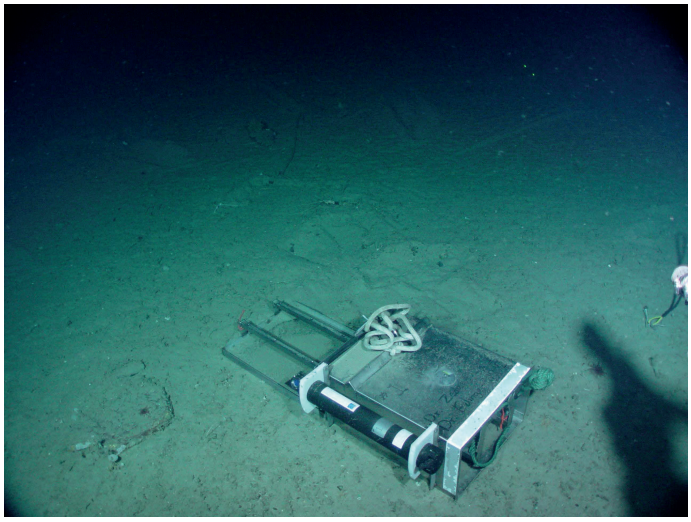

Figure 3.7: The Mud Site, with settlement plate and attached Doppler profiler. This location is typical of the benthic environment in Haddock Channel.

The Coral Site, located at a depth of 696 m, consists of a thicket of *Keratoisis grayi*, with individual colonies ranging in height from tens of centimeters to approximately 1.5 meters (visual inspection from ROV video). Figure 3.8 is a still frame from video of the thicket taken by ROPOS during instrument deployment. The sea floor in this area consists of the same muddy substrate with scattered cobbles that is found at the Mud Site.

Analysis of the ROPOS video log from the profiler deployment dive was used to identify approximate locations of coral along the transect from the Mud Site to the Coral Site. Each time a coral was seen in the video the time index corresponding to when the ROV passed closest to it (usually within a couple of meters or less) was recorded. The set of recorded times was then matched with the coordinate log from the ROPOS ROV's Ultra-short baseline (USBL) acoustic positioning system, to obtain the corresponding latitude and longitude of the coral colonies. The locations of individual *Keratoisis* within the thicket, and those coral encountered during the

ROV transect from the Mud Site to the Coral Site are shown in Figure 3.9. The two sites are approximately 100 meters apart.

The relative location of *Keratoisis grayi* colonies directly adjacent to the Doppler profiler in the coral thicket as estimated using the ROPOS video log, are shown in Figure 3.10. The position of large coral relative to the placement of the Doppler profiler is important when examining any directional biases present in the flow regime.

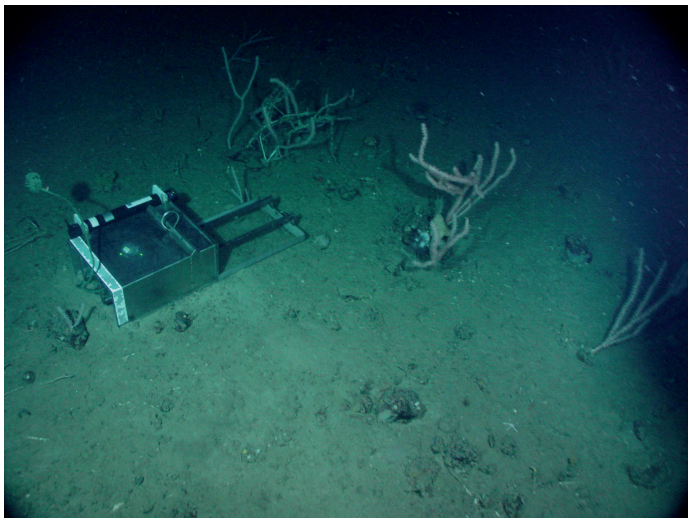

Figure 3.8: *Keratoisis ornata* thicket in Haddock Channel at a depth of 696 m. The settlement plate and attached Doppler profiler are pointed due north.

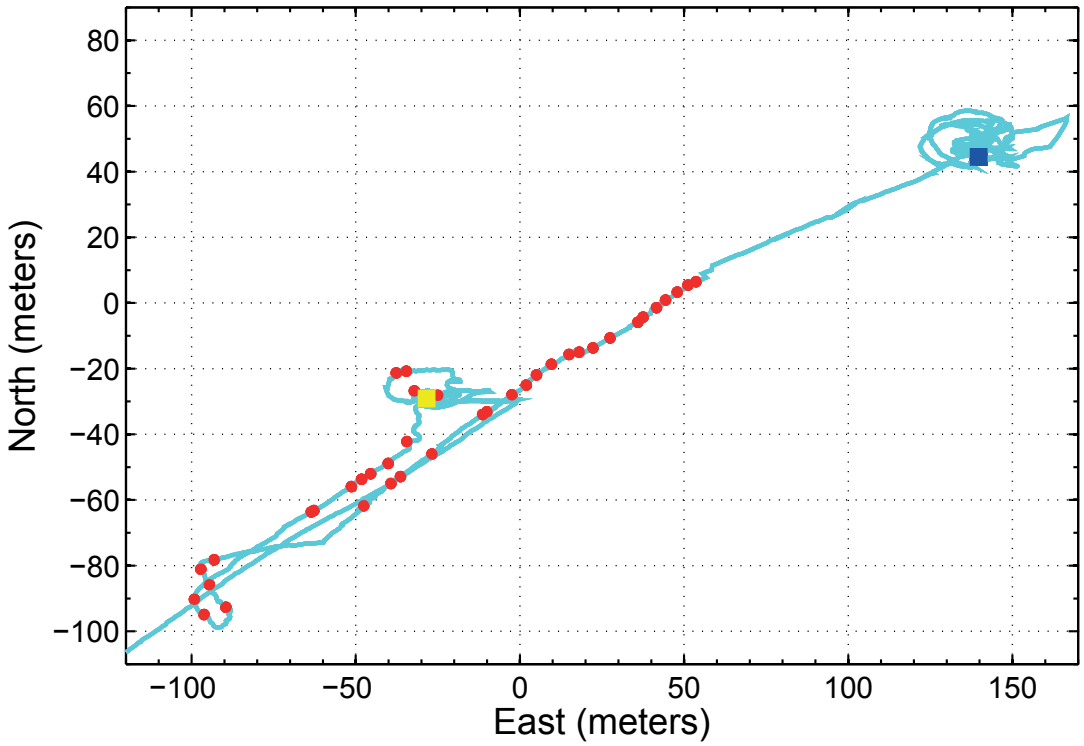


Figure 3.9: Approximate location of coral colonies (red dots) in the Doppler profiler deployment area of Haddock Channel based on visual analysis of the ROPOS video log. The blue square represents the location of the Mud Site, the yellow square is the location of the Coral Site within the *Keratoisis* thicket. The cyan line is the ROPOS ROV transect. The sites are approximately 100 m apart.

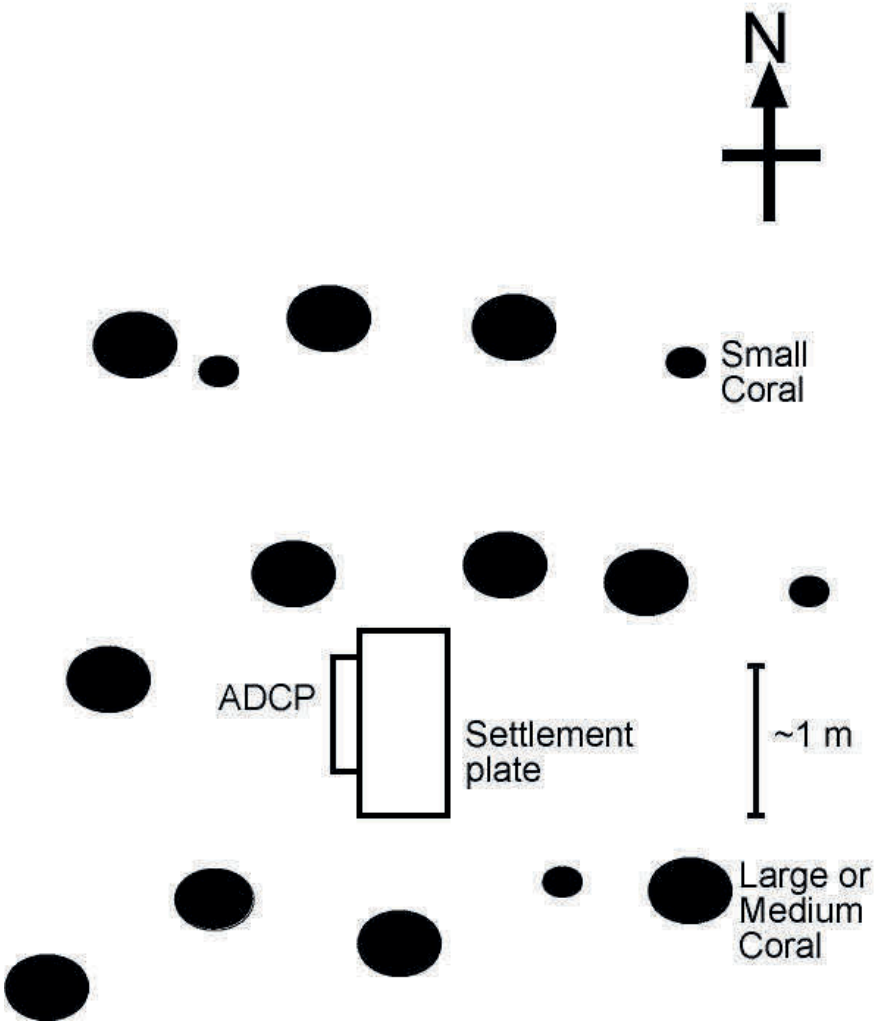


Figure 3.10: Approximate locations of coral colonies relative to the settlement plate and attached Doppler profiler at the Coral Site based on ROPOS video log. 1 m horizontal scale indicates distance from settlement plate. Height estimates for large coral 0.5 - 1 m and above, medium coral 0.25 - 0.5 m, small coral 0.1 - 0.25 m.

## 3.6 Temperature and Duty Cycle Considerations

The Nortek Aquadopp profilers used in the deployment were new and untested in this type of environment: deep water, low temperature (mean bottom temperature of 4.5°C during deployment). Analysis of the onboard battery voltage record (Figure 3.11) showed a voltage drop from 8.5 V at the time of deployment to 8.1 V approximately 40 minutes later. The battery then showed some voltage recovery, as expected for lithium batteries, but approximately 78 hours after the initial battery drop the voltage began to cycle between 8 and 8.3 volts which was insufficient to maintain the original 5 second sampling rate, thus changing the period between acquisition of velocity profiles.

Based on personal communication with the manufacturers it was determined that the low voltage is due to the combination of high duty cycle (short period between profiles) and low temperatures ($\leq 10$°C). Essentially, the low temperature environment, combined with a configuration for short term deployment and maximum data acquisition, resulted in insufficient time for the cell chemistry to recover and avoid the excessive voltage drop. For future deployments using these Nortek instruments it is recommended that the sampling rate be decreased to mitigate the effects of the low temperatures ($\sim 4$°C) on the battery voltage.

Data obtained after $\sim$ 78 hours into the deployment was considered unreliable because time intervals between profiles were not consistent after this time. The low operating voltages were also seen to introduce velocity offsets in data of AQD1 (Mud Site). Details of how data were recovered are provided in Section 4.1.1.

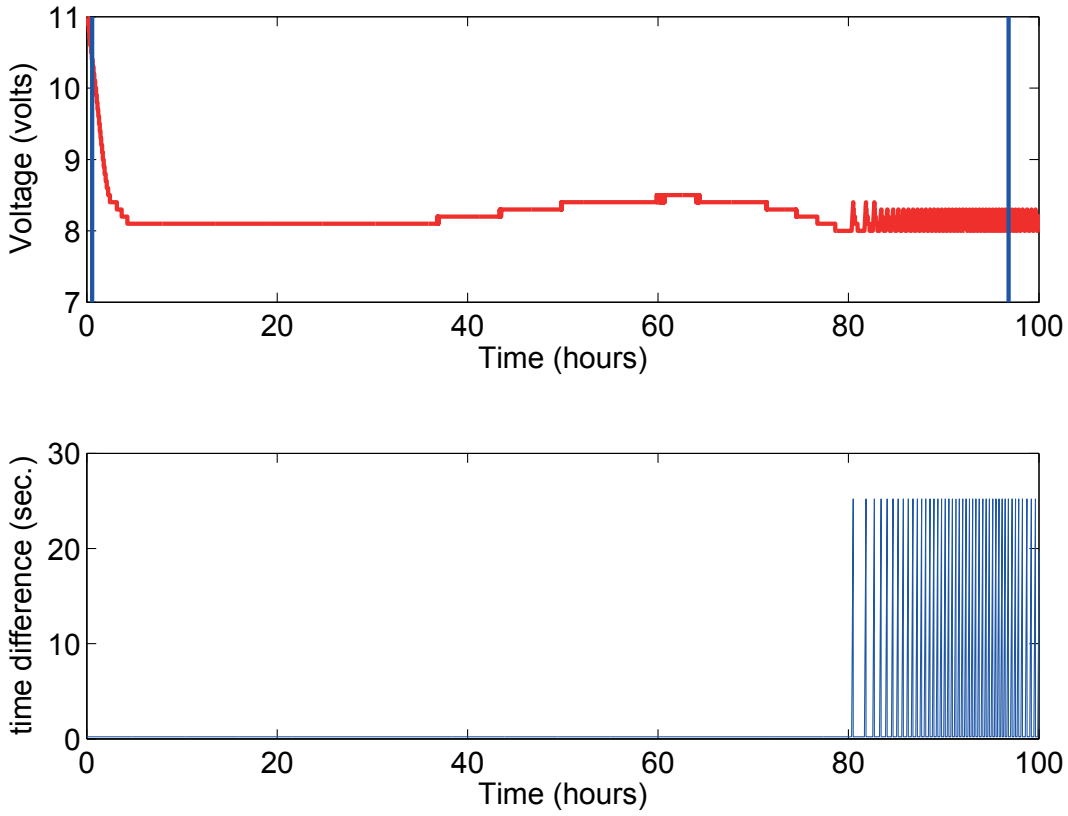


Figure 3.11: Top: Battery voltage for AQD2 during deployment, note the voltage oscillation. The two blue lines represent the deployment period. Bottom: Time difference between profile intervals.

# Chapter 4

# Analysis of Doppler Profiler Data

This chapter describes the processing and analysis of data from Aquadopp Doppler Profilers deployed at two locations in Haddock Channel in July 2007. The main focus of the chapter is the fitting of velocity profiles from both experiment sites to the logarithmic law of the wall, and subsequently obtaining values for friction velocity and bottom roughness as these are important parameters for characterizing the bottom boundary layer.

Section 4.1 discusses the raw acoustic backscatter and velocity in beam coordinates as well as detailing the cropping of data due to battery voltage issues discussed in Section 3.6. Section 4.2 presents an analysis of power spectra. This analysis provides insight into appropriate cutoff frequencies for subsampling of the data and attempts to determine if the power spectra exhibit a characteristic $-5/3$ slope, thereby linking energy transfer in the inertial subrange in spectral space with the logarithmic layer in physical space. Section 4.3 discusses the selection of velocity data based on minimum amplitude thresholds arising from an instrument hardware issue whereby velocity measurements corresponding to low backscatter intensity display a bias. The transformation of velocity data from Beam coordinates to the East North Up coor-

dinate systems is also discussed. Section 4.4 presents mean velocity profiles as well as detailing a directional decomposition method to assess any directional dependence present in the data as well as mean velocity profiles for four directional quadrants. Section 4.5 details the fitting of data to the logarithmic law of the wall and presents the results; estimates of bottom roughness $z_o$, friction velocity $u_*$, and the regression of $u_*$ versus speed.

A variety of data analysis approaches were explored. Multiple averaging periods were examined for use in constructing mean velocity profiles, thereby limiting the effects of changes in the flow on estimates of friction velocity and bed roughness (*Gross and Nowell*, 1983; *Grant et al.*, 1984; *Cheng et al.*, 1999). Alternatively, velocity data from each Doppler Profiler measurement point was sorted into speed bins for which a series of log fits was carried out over a range of speeds following *Lacy and Sherwood* (2004). Both approaches to velocity profiles were examined.

Individual profiles were screened to identify those that are consistent with the logarithmic law of the wall. Velocity profiles which have high correlation coefficients $r^2$, in the log-linear least squares regression of $U(z)$ and $ln(z)$ were considered acceptable for further analysis, and other profiles were rejected (*Frechette et al.*, 1989). *Drake et al.* (1992) note that confidence intervals on $u_*$ and $z_o$ from the log profile technique depend on the number of profile points used and the correlation coefficient $r^2$, and will have excessively large error bars if $r^2$ is less than 0.994. Therefore only velocity profiles with $r^2$ greater than 0.994 were selected for further analysis. However, *Cheng et al.* (1999) and *Reidenbach et al.* (2006a) apply a less stringent cutoff value, and reject only velocity profiles having an $r^2$ value less than 0.8 which allows them to average more data into their final analysis thus reducing uncertainties. Overall, three variations on the velocity profile processing approach, each yielding different numbers of usable profiles for use in the regression, were examined and the results and analysis

of all three variants are presented.

## 4.1 Acoustic Backscatter Intensity

Doppler sonar profilers rely on acoustic backscatter from particulates suspended in the water column. If there are inadequate concentrations of such scatterers, the signal level becomes too low to extract accurate velocity estimates. Backscattered intensity always decreases with increasing range due to spherical spreading and absorption (see Chapter 5) and this imposes a maximum profiling range on the instrument. It is possible in cases of extremely high concentration (that might occur in a river or close to the bottom in a very high velocity flow), that backscatter from greater distances is masked by the high concentrations closer to the instrument: this situation is not a concern in the present study.

Preliminary analysis of the acoustic backscatter from both the Coral and Mud sites indicated that of the eight meters of water column above the seabed that were profiled, only the bottom four meters provided sufficient backscatter signal strength to yield reliable velocity measurements. Figures 4.1 and 4.2 show profiles of the acoustic backscatter as uncalibrated digitizer counts, and velocity from transducer beam 3 at the Mud and Coral Site, respectively. At both sites, signal strength from the upper four meters was relatively low ($< 30$ counts) and homogeneous with minimal visible structure. The velocity data at both sites show a similar lack of water column velocity structure associated with the reduced backscatter intensity beyond $\sim$5.5 above the seabed.

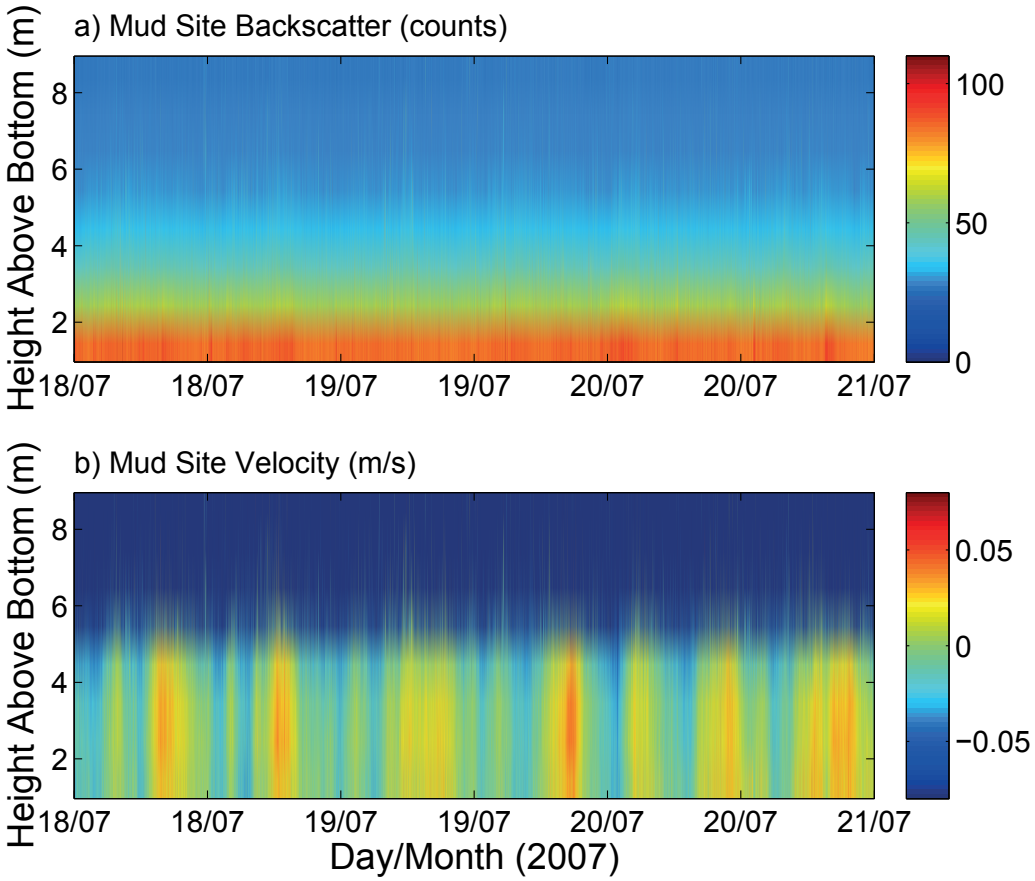


Figure 4.1: Mud Site a) Backscatter intensity (counts) from AQD1, transducer Beam 3, b) Beam velocity (m/s) from AQD1, transducer Beam 3.

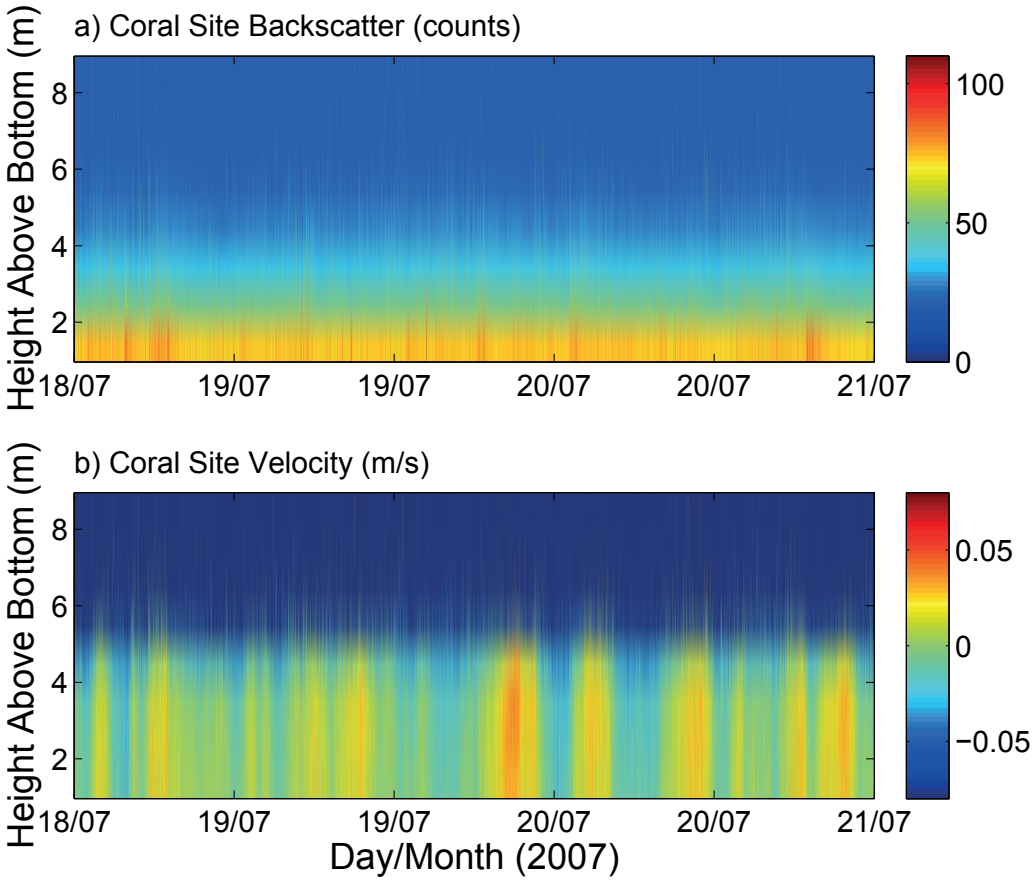


Figure 4.2: Coral Site a) Backscatter intensity (counts) from AQD2, transducer Beam 3, b) Beam velocity (m/s) from AQD2, transducer Beam 3.

### 4.1.1 Data Cropping Due to Instrument Voltage Issues

As discussed in Section 3.6, the low temperature and high duty cycle regime imposed upon the instruments during the deployment resulted in a battery voltage that dropped below minimum operating levels in 3 days. This caused the sampling rate to fluctuate due to insufficient power, see Figure 3.11. The data recorded after 78 hours into the deployment was not deemed acceptable.

Data quality was assessed by plotting component velocities from individual transducer beams from each profiler and inspecting for any inconsistencies in the velocity records. An inconsistent bias was visually identified in the bin 1 velocities, relative to bins 2 through 4, of two beams of AQD1 (Mud Site). This bias can be seen as a velocity offset across all velocities in bin 1 relative to bin 2, as shown in Figure 4.3, (all three time series were filtered to remove noise for the purposes of clarity in the figure). For example, in Figure 4.3 panel c, all bin 1 (Blue) velocities of Beam 3 clearly show a positive bias relative to bin 2 (Red). Bin 1 speeds are consistently offset from bin 2 by approximately +2.1 cm $s^{-1}$. Similarly, bin 1 (Blue) of Beam 1 (Figure 4.3 panel a), exhibits a negative velocity bias, of -0.94 cm $s^{-1}$ relative to the respective bin 2 (Red) speeds. No bias was observed in Beam 2. It is important to note that these biases are present in bin 1 only, and are not observed in the higher bins. The biases were determined to be the result of a DC voltage offset present in the hardware of the AQD, and are associated with a voltage "draw down" that occurs when the instrument transmits sound into the water. Bin 1 is most affected because it is the first bin processed by the instrument, however for subsequent bins, the voltage has recovered.

Correcting the issue requires a velocity bin from each transducer with no offset to be used as a reference to correct data for each respective beam. Velocity data from

the reference bin was subtracted from the bin with an offset to yield a time series of the bias signal which was then filtered with a third order Butterworth filter with cutoff frequency of $1 \times 10^{-3}$ Hz (Equation 4.1). The mean of the filtered bias signal was then subtracted from the affected velocity bin to remove the offset (Equation 4.2). That is:

$$V_B = V_O - V_R \tag{4.1}$$

where $V_R$ is the reference bin velocity, $V_O$ is the offset bin velocity, and $V_B$ is the velocity bias signal, and the corrected velocity was arrived at as:

$$V_C = V_O - mean(V_{FB}) \tag{4.2}$$

where $V_{FB}$ is the filtered velocity bias signal, and $V_C$ is the corrected bin velocity. The corrected bin 1 velocities (Black dashed) are shown in Figure 4.3.

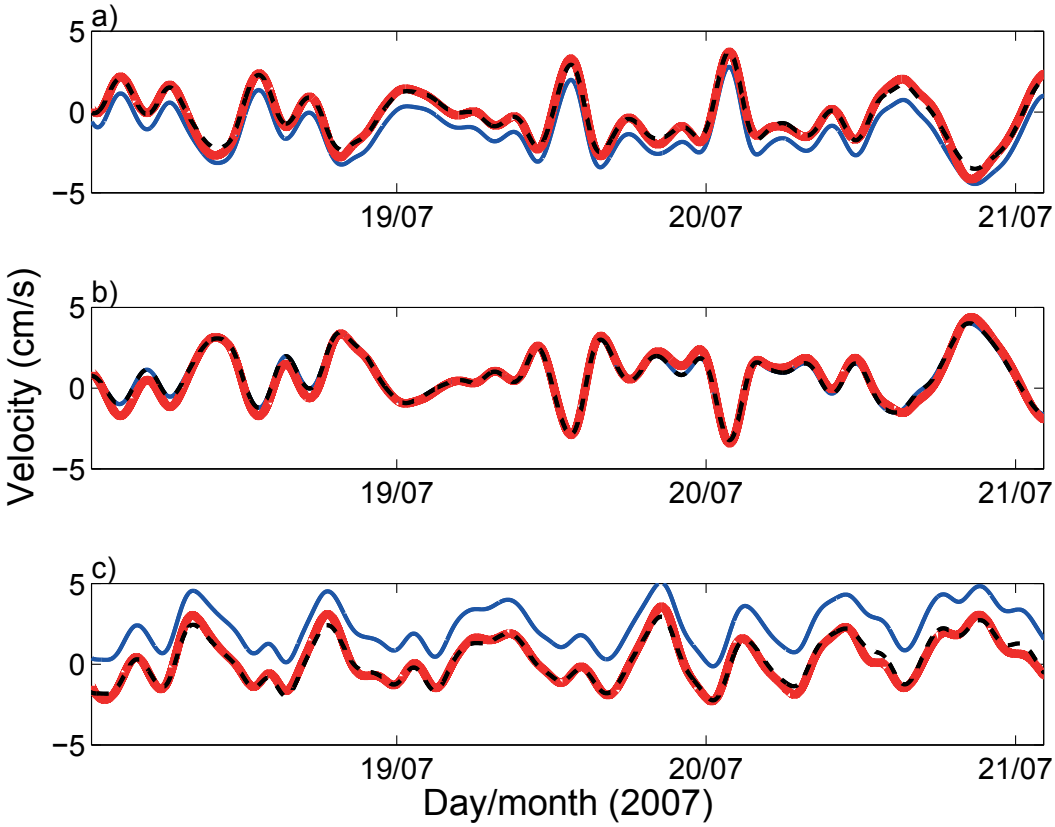


Figure 4.3: Beam velocity records for a) Beam 1, b) Beam 2, and c) Beam 3 of AQD1. Solid blue line is bin 1, red line is bin 2, and black dashed line is bias corrected bin 1.

## 4.2 Power Spectral Density

Power spectra of the data were analyzed in order to determine important time scales in the data, such as tidal and inertial forcing terms or the frequency at which measurement noise begins to dominate the signal. The spectral shape can also reveal the nature of turbulent energy transfer characteristic of the inertial subrange where energy is only transferred by inertial forces i.e. vortex stretching (*Kundu and Cohen*, 2004). Within the boundary layer, turbulent kinetic energy (TKE) is transferred from larger eddies, which may be the width of the boundary layer, to smaller and smaller scale eddies. Both production and dissipation are small in the inertial subrange in the frequency domain corresponding to the inertial sublayer or logarithmic layer in physical space. Ultimately, at the smallest scale of the turbulent eddies, known as the Kolmogorov microscale, the turbulent energy is dissipated via molecular viscosity (*Kundu and Cohen*, 2004).

The power spectral density (PSD) for profile bins 1, 2, and 3, were examined for both the Coral and Mud sites to determine if the power spectra exhibited a $-5/3$ slope (*Reidenbach et al.*, 2006a; *Lacy and Sherwood*, 2004). Figure 4.4 is a plot of the PSD at the Coral Site, 3.46 m above the seafloor, for all three beams. Power spectra are estimated using the Welch method with a 4096 point Hamming window, overlapped at 50% on time series of 50363 points sampled at 0.2 Hz. At frequencies greater than approximately $3 \times 10^{-3}$ Hz the power spectrum has the characteristics of white noise. At lower frequencies the spectrum is more characteristic of red noise likely resulting from large scale geophysical processes. Also shown in Figure 4.4 is a power spectrum with no averaging from Beam 3 (Blue dashed) in order to show the peak at $3.5 \times 10^{-5}$ Hz ($\tilde{1}2$ hours) representing the semi-diurnal tidal signal, which is the only forcing visible in the PSD. The absence of the $-5/3$ slope in the power

spectra for the Coral Site suggests that the data does not resolve the inertial subrange above the range of the measurement noise. Based on this power spectral analysis, data at frequencies above $3 \times 10^{-3}$ Hz are dominated by noise and subsequent data have been filtered to eliminate these high frequency components.

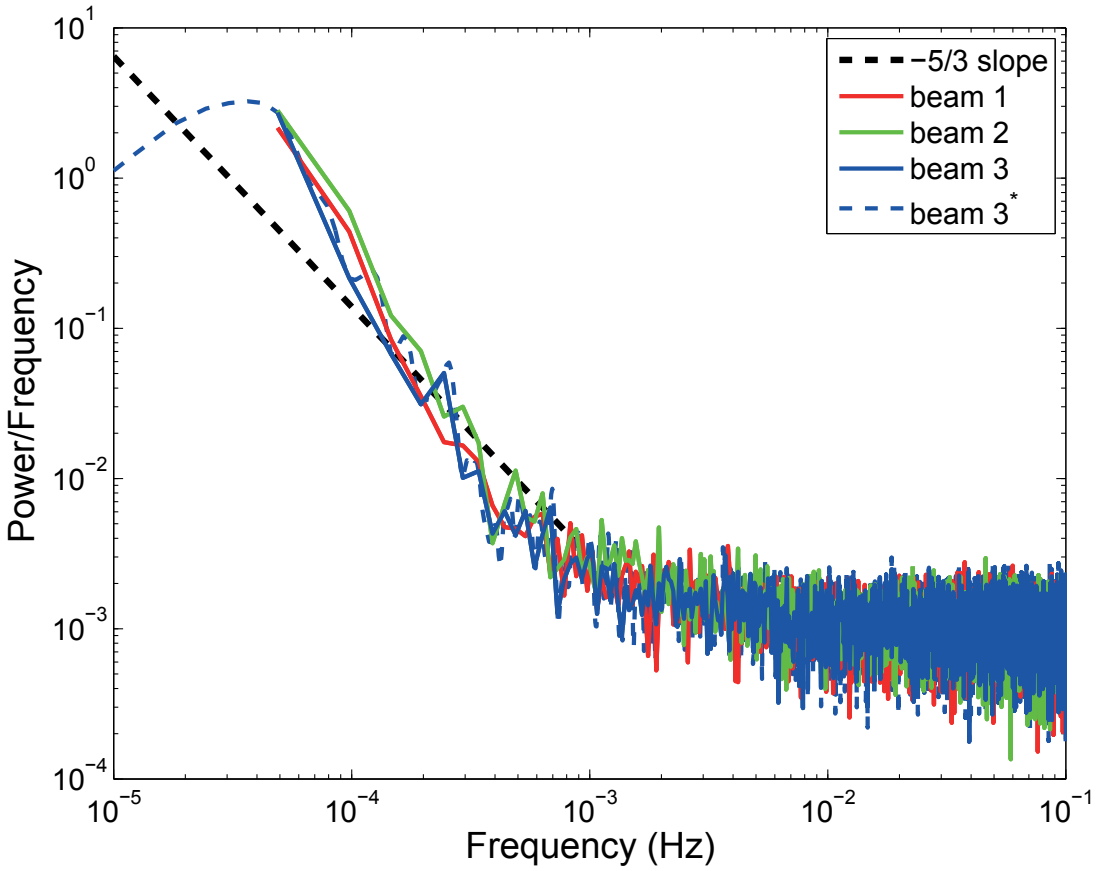


Figure 4.4: Coral Site: Power spectral density for Beams 1, 2, and 3, bin 3, 3.46 m above the bottom. The blue dashed line represents Beam 3 without averaging to show the peak at $3.5 \times 10^{-5}$ Hz ($\tilde{1}2$ hours).

## 4.3 Data Selection Based On Amplitude Threshold

The quality of the velocity measurements made by the Doppler Profilers is directly related to the signal amplitude or backscatter intensity. If the backscatter intensity is too low then the velocity measurements will not be reliable. Additionally, based on personal communication with the manufacturer, it was known that at low signal strength the Aquadopp Profiler can yield biased (negative or positive) velocity measurements. It is important to note that this bias issue is separate and independent of the biases discussed in Section 4.1.1 where backscatter strength was not an issue.

As seen in Figures 4.1 & 4.2, the range at which backscatter signal levels become insufficient for data analysis occurs between approximately 4.46 m and 5.46 m above the bottom (bins 4 and 5 respectively). For both the Mud and Coral Site, bin 4 is taken as the maximum range from which good data could be recovered. In order to ensure that only reliable data was selected from bin 4, only velocity data with corresponding backscatter strength above a minimum intensity threshold was accepted. To determine an appropriate minimum backscatter thresholds for the Mud and Coral site, the difference in velocity between bins 4 and 3 ($\Delta V_{4-3}$) were plotted (Figures 4.5 and 4.6) as a function of backscatter intensity (counts), for each beam. Assuming a uniform distribution of velocity and direction, we would expect there to be no systematic bias in the $\Delta V_{4-3}$ values. Where there is evidence of a bias associated with a reduced backscatter level, it indicates a threshold below which data from bin 4 are unreliable.

At the Mud Site (Figure 4.5), for backscatter intensities lower than $\sim 37$ counts, there is a significant negative bias $\Delta V_{4-3}$. Above 37 counts, the difference in velocities is uniformly centered about zero as expected since there should be no significant

variation in velocities between bin 3 to bin 4 for any given backscatter intensity. At the Coral Site (Figure 4.6), the negative bias occurs at backscatter intensities of 30 counts or lower. For each instrument, the observed velocity biases occur at approximately the same backscatter intensity in each of the three transducer beams, which is consistent with an instrument hardware issue. Based on this bias analysis, data for which signal amplitudes fell below 37 counts in the Mud Site (AQD1) and 30 counts in the Coral Site (AQD2) were omitted from further analysis.

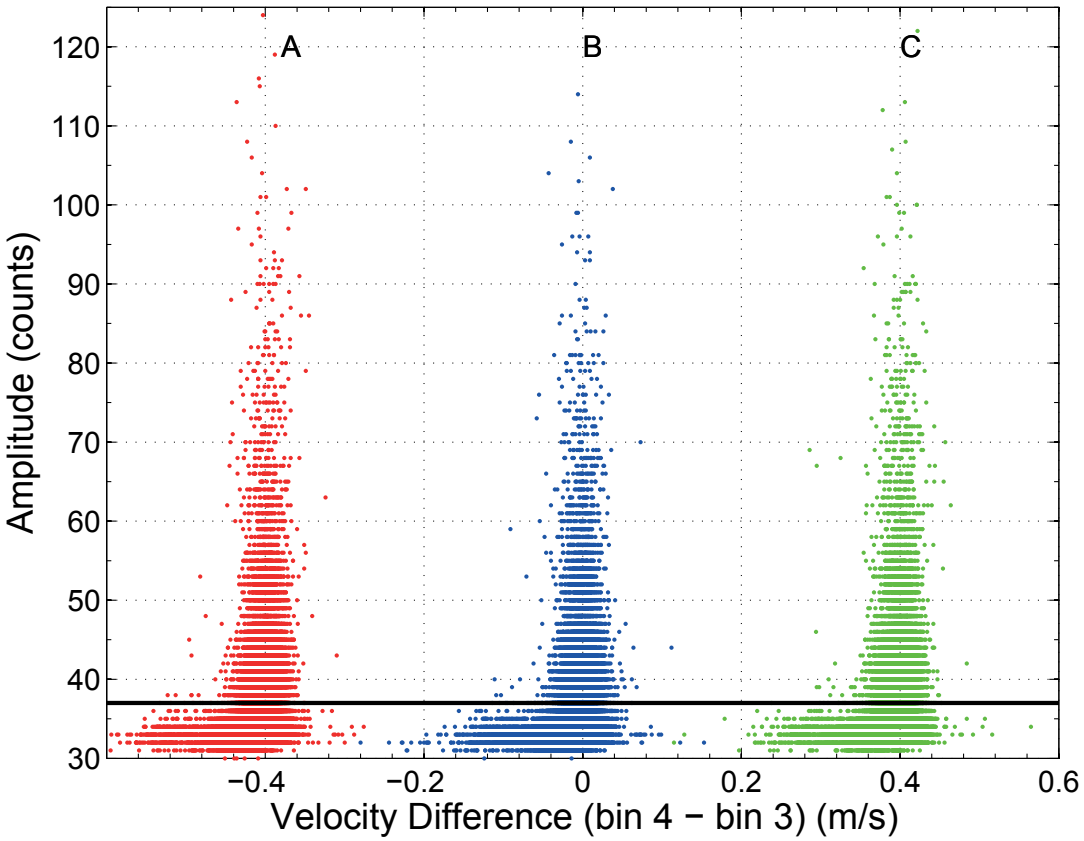


Figure 4.5: Mud Site: backscatter (counts) versus velocity difference (m $s^{-1}$) between bins 4 and 3. Minimum amplitude threshold (black line) for A: Beam 1 (Red), B: Beam 2 (Blue), C: Beam 3 (Green) at the Mud site. For all three beams, there is a negative bias in $\Delta V_{4-3}$ at amplitudes below approximately 37 counts. Note that $\Delta V_{4-3}$ for Beams 1 and 3 have been offset from zero by -0.4 m/s and +0.4 m/s respectively in the plot for the purposes of clarity.

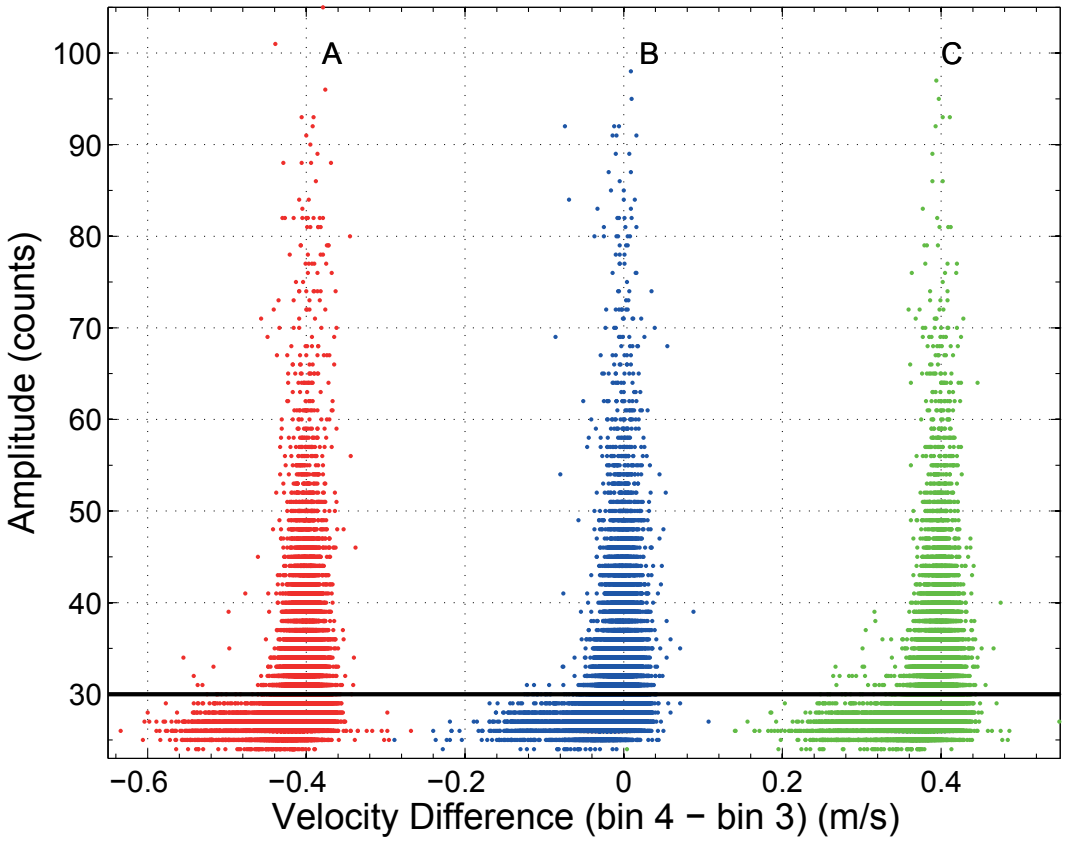


Figure 4.6: Coral Site; backscatter (counts) versus velocity difference (m $s^{-1}$) between bins 4 and 3. Minimum amplitude threshold (black line) for A: Beam 1 (Red), B: Beam 2 (Blue), C: Beam 3 (Green). For all three beams, there is a negative bias in $\Delta V_{4-3}$ at amplitudes below approximately 30 counts. Note that $\Delta V_{4-3}$ for Beams 1 and 3 have been offset from zero by -0.4 m/s and +0.4 m/s respectively in the plot for the purposes of clarity.

### 4.3.1 Averaging the Velocity Data Based on Amplitude Threshold

The power spectrum (Figure 4.4) indicates that the data are dominated by noise at frequencies above $f_c = 3 \times 10^{-3}$ Hz. The data as collected is therefore highly over sampled and needs to be resampled at a rate consistent with the $f_c = 3{\times}10^{-3}$ Hz cutoff frequency. Velocity data meeting the minimum intensity threshold were identified and a new resampled data set was created for each beam. This resampling was achieved by using a 33 point average. To avoid aliasing and to ensure reconstruction of the time series requires a minimum sampling rate, referred to as the Nyquist rate, defined as twice the highest frequency present in the signal. In this case, it is based on the highest frequency containing meaningful information before the signal becomes dominated by noise. The Nyquist rate is therefore $f_N = 6 \times 10^{-3}$ Hz, with a corresponding period of T =166.6 seconds. With the original data sampled at a rate of one sample every five seconds, the number of averaged data points required to meet the new sampling rate is 33 (166.6 x 0.2 Hz).

### 4.3.2 Transformation of Coordinate System: Beam to ENU

Individual beam velocity data as measured by the three acoustic beams must be converted to an Earth coordinate system. This conversion is accomplished in a two step process: First the observed beam velocities are used to estimate the velocity ($u$, $v$, and $w$) relative to the doppler profiler itself. The instrument referenced velocities are then rotated using measured heading, pitch and roll to recover Earth referenced coordinates. The three beam velocities expressed in terms of $u$, $v$, and $w$ for the Nortek Aquadopp are:

$$\begin{aligned} B_1 &= 0 + v\sin\theta + w\cos\theta \\ B_2 &= 0 - v\sin\theta + w\cos\theta \\ B_3 &= u\sin\theta + 0 + w\cos\theta \end{aligned} \tag{4.3}$$

where $u$, $v$, and $w$ are the x, y, and z components of the flow velocities relative to the instrument, and $\theta = 45°$ which is the transducer tilt angle from vertical.

A transformation matrix T can be defined from Equation 4.3:

$$T \equiv \begin{bmatrix} 0 & \sin\theta & \cos\theta \\ 0 & -\sin\theta & \cos\theta \\ \sin\theta & 0 & \cos\theta \end{bmatrix}. \tag{4.4}$$

such that

$$\vec{B} = \begin{bmatrix} B_1 \\ B_2 \\ B_3 \end{bmatrix} = T\vec{U} \tag{4.5}$$

Equation 4.5 can be rearranged to solve for $\vec{U}$ given $\vec{B}$ (the measured beam velocities):

$$\vec{U} = T^{-1}\vec{B}. \tag{4.6}$$

Velocity data were transformed using Equation 4.6 with the MATLAB routine 'Transform.m' obtained from Nortek.

The velocity components $u$, $v$, and $w$ calculated with Equation 4.6 are in a coordinate system with respect to the instrument. Rotation of the velocity data into the Earth coordinate system (East-West, North-South, and Up) is carried out using the pitch (p), heading (h), and roll (r) of the instrument, along with a correction for local magnetic declination as the heading is measured with respect to magnetic

north. These parameters are then used to make heading and tilt matrices, $H$ and $P$ respectively,

$$H = \begin{bmatrix} \cos h & \sin h & 0 \\ -\sin h & \cos h & 0 \\ 0 & 0 & 1 \end{bmatrix} \tag{4.7}$$

$$P = \begin{bmatrix} \cos p & -\sin p \sin r & -\cos r \sin p \\ 0 & \cos r & -\sin r \\ \sin p & \sin r \cos p & \cos p \cos r \end{bmatrix} \tag{4.8}$$

which are combined with $T$ to create a resultant transformation matrix, $R = H \times P \times T$. When linearly multiplied by $R$, the three beam velocity components: $B_1$, $B_2$, and $B_3$, can be converted directly into ENU coordinates

$$\begin{bmatrix} E \\ N \\ U \end{bmatrix} = R \times \begin{bmatrix} B_1 \\ B_2 \\ B_3 \end{bmatrix}. \tag{4.9}$$

## 4.4 Mean Flow Conditions

Profiles of velocities in the East, North, and Up directions for both the Mud and Coral Site are shown in Figures 4.7 and 4.9, respectively. Maximum East-West and North-South velocities at both sites are on the order of 10 cm $s^{-1}$. Overall, flow speeds magnitudes are consistent with those seen in the St. Pierre Bank record. Tidal analysis was inconclusive, due to the short duration of the deployment (i.e. insufficient number of tidal cycles available to analyze). The decrease in backscatter intensity above 4 m is also visible in the velocity profile at both sites. Profile averaged time

series (mean of bins 1 to 3) of East, North, and Up components are shown in Figures 4.8 and 4.10 for the Mud and Coral Site, respectively.

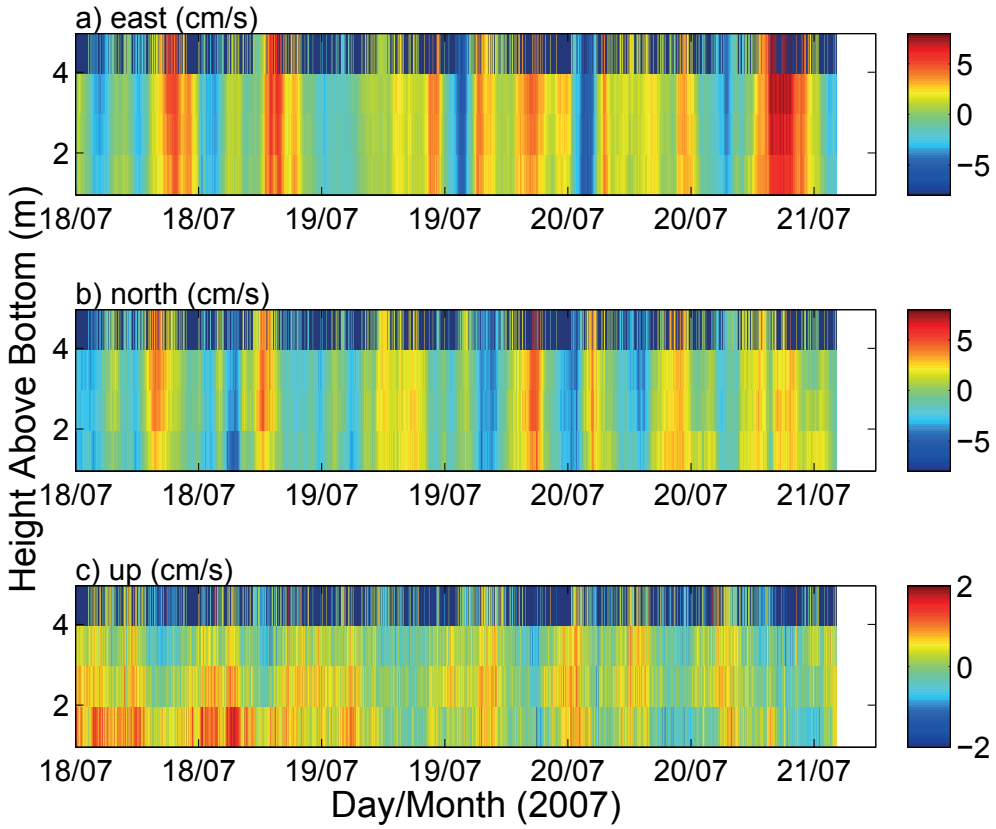


Figure 4.7: Mud Site: ENU Velocities for bins 1 to 4 (1.46 to 4.46 m above the bottom). A) East-West flow, with positive flow to the East, B) North-South flow, with positive flow to the North, C) Vertical flow, with positive flow upwards, and negative flow toward the seafloor. Time axis is days in July, 2007, at 12:00 AM and 12:00 PM respectively.

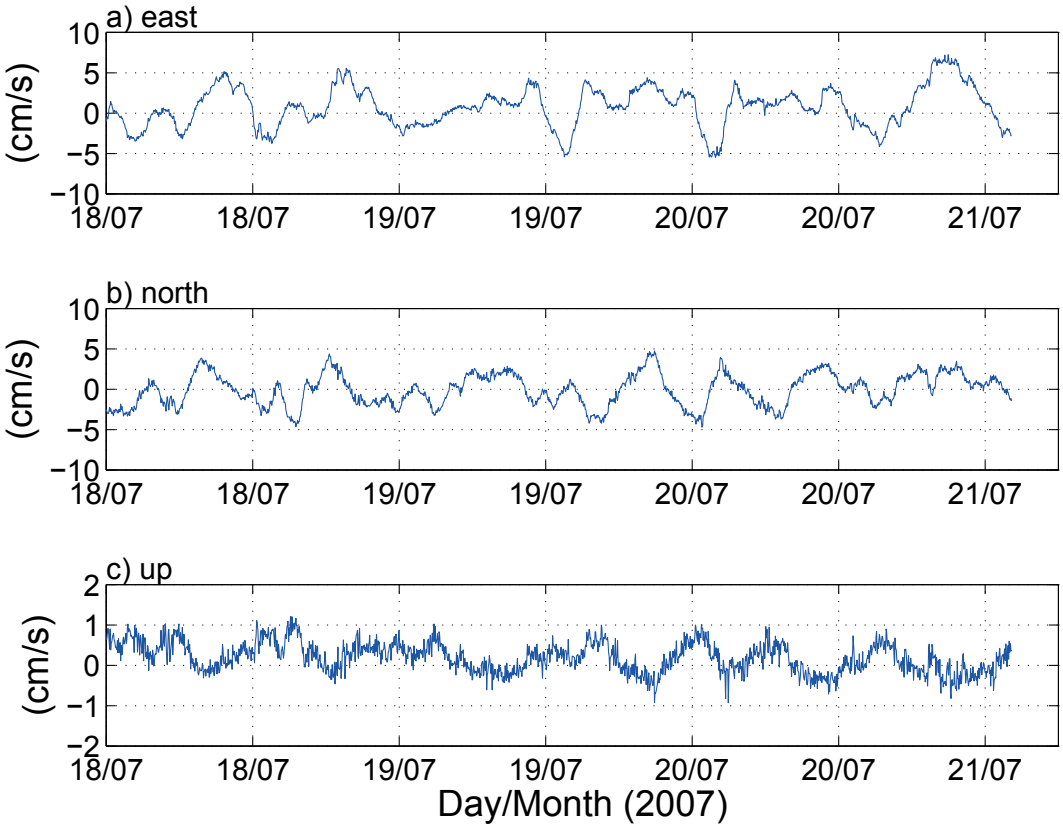


Figure 4.8: Mud Site: ENU Profile averaged velocities (mean of bins 1 to 3). A) East-West flow, with positive flow to the East, B) North-South flow, with positive flow to the North, C) Vertical flow, with positive flow upwards. Time axis is days in July, 2007, at 12:00 AM and 12:00 PM respectively.

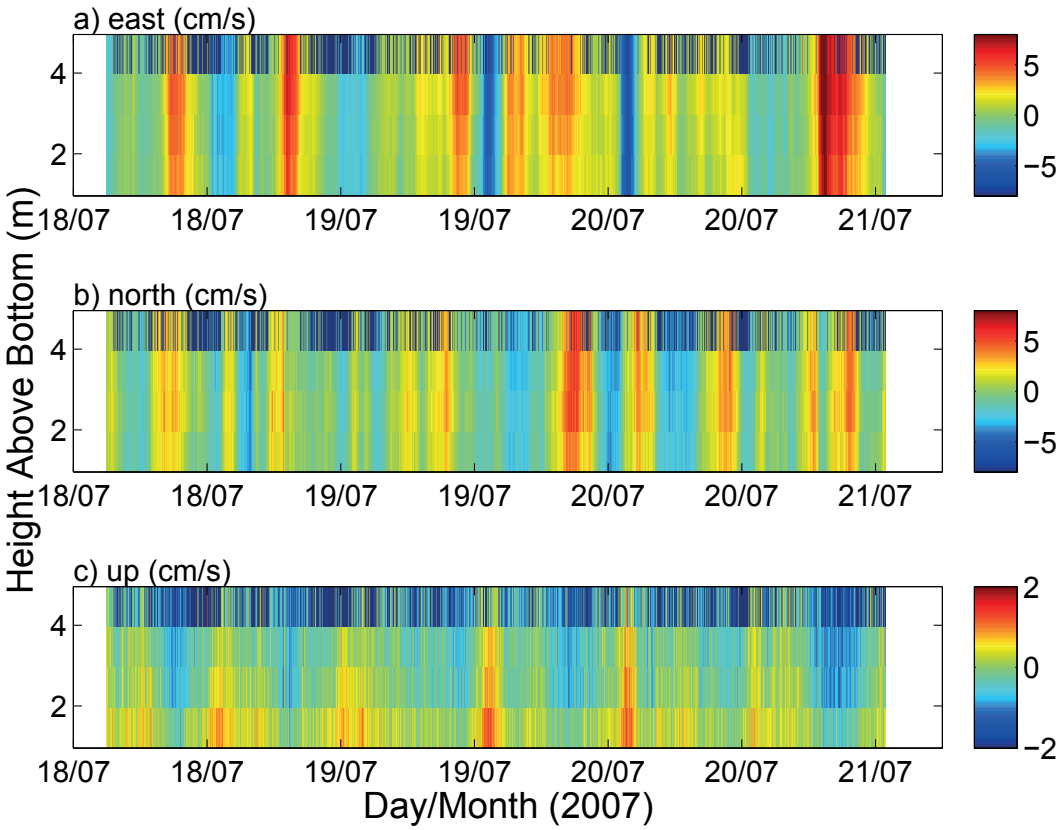


Figure 4.9: Coral Site: ENU Velocities for bins 1 to 4 (1.46 to 4.46 m above the bottom). A) East-West flow, with positive flow to the East, B) North-South, flow direction with positive flow to the North, C) Vertical flow, with positive flow upwards. Time axis is days in July, 2007, at 12:00 AM and 12:00 PM respectively.

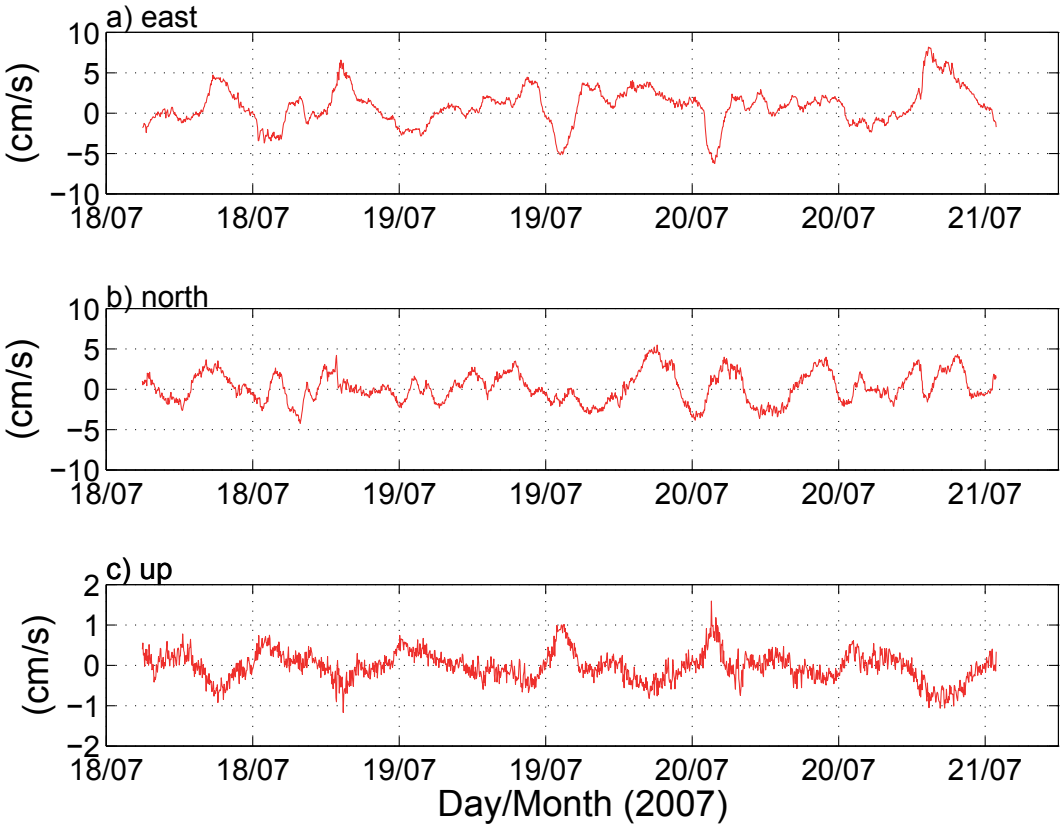


Figure 4.10: Coral Site: ENU Profile averaged velocities (mean of bins 1 to 3). A) East-West flow, with positive flow to the East, B) North-South, flow direction with positive flow to the North, C) Vertical flow, with positive flow upwards. Time axis is days in July, 2007, at 12:00 AM and 12:00 PM respectively.

### 4.4.1 Mean Speed Profiles and Directional Decomposition of ENU Velocities

Mean speed profiles $s(z)$ as a function of height above the sea floor were created to characterize the bottom boundary layer. The magnitude and direction of mean currents at both sites were obtained using Euler's Formula with the East (E) and North (N) velocities represented as components of the complex number along the real and imaginary axes respectively, shown in equation 4.10,

$$S = E + iN \tag{4.10}$$

which can also be written in as

$$S = |S|e^{i\phi} = se^{i\phi} \tag{4.11}$$

where $|S| = s$ is the velocity magnitude, and the direction of the current is $\phi = tan^{-1}\frac{N}{E}$.

Speeds from each bin $s_z(t)$, were normalized by dividing by the bin 3 speed $s_3(t)$, therefore removing the time component from the data:

$$s(z) = \frac{s_z(t)}{s_3(t)}. \tag{4.12}$$

Normally the velocity bin furthest away from the bottom would be used as the free stream or reference velocity for normalization. However, bin 3 was selected to be the reference bin due to larger uncertainties in the bin 4 data associated with low backscatter intensity. A minimum speed threshold of 2 cm $s^{-1}$ was imposed on data from each bin to compensate for higher uncertainties in directions associated with lower speeds, in other words, only speeds greater than 2 cm $s^{-1}$ were accepted.

The entire normalized speed data set was then averaged to produce a single representative speed profile $\overline{s}_{total}(z)$. Characteristic profiles created in this way for both the Mud and Coral Site are shown in Figure 4.11.

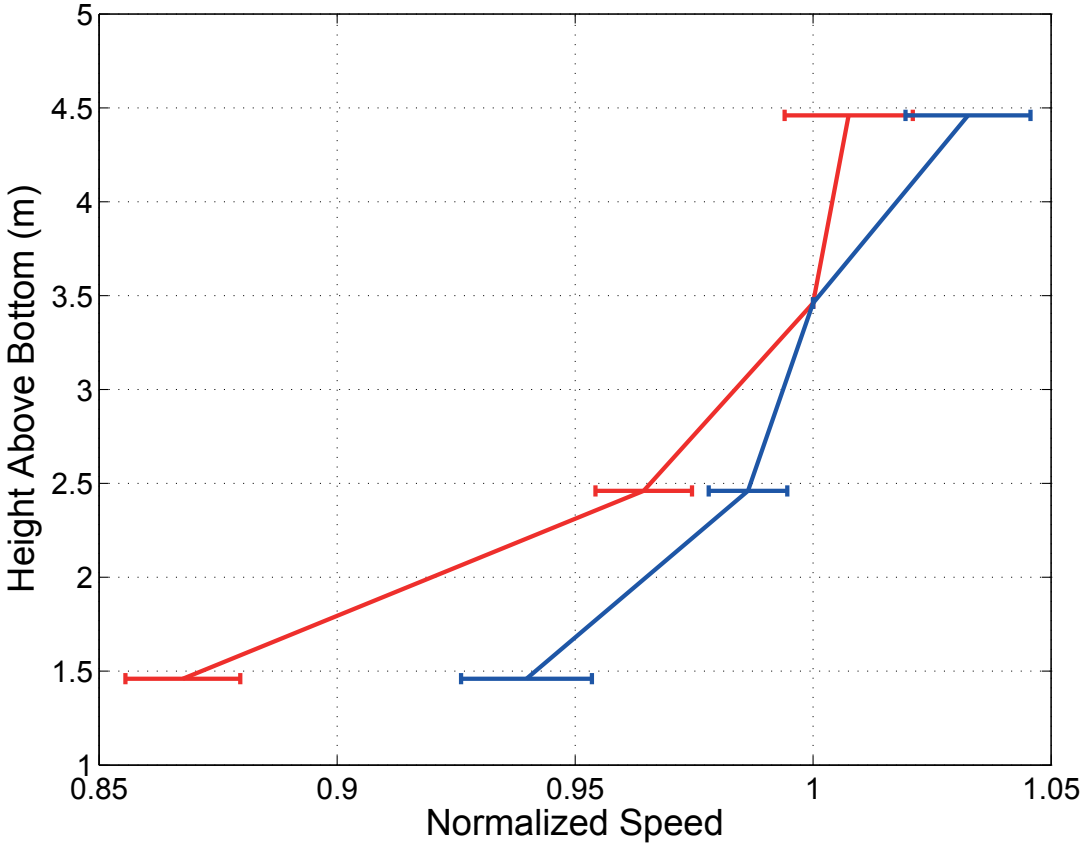


Figure 4.11: Mean normalized speed as a function of height above the bottom at the Coral (Red) and Mud Site (Blue), see Equation 4.12, Error bars are 95% confidence intervals. There are no error bars on bin 3 because it is used as the reference depth for normalization.

A weakness in the present study is that observations are only available at one location in a coral thicket. That weakness can be somewhat overcome by breaking the data down by flow direction. In a sense, observations from different flow directions

sample flow conditions downstream of separate coral areas and support the assertion that the observations as a whole are characteristic of flow in the respective coral area.

Directional dependence is suppressed in the characteristic velocity profile, due to averaging of data from all directions. $\phi$ was therefore divided into four sub-sets representing different directional quadrants, centered on the North East, North West, South West, and South East directions. Corresponding speed sub-sets were created, and again speeds less than 2 cm $s^{-1}$ were discarded. Table 4.1 gives the number of mean speed data points in each directional quadrant for both the Mud and Coral Site. This approach has the advantage of essentially simulating four independent data sets from a single deployment, with different directional flow regimes and coral distributions.

The directional distribution of the flow was evaluated using rose plots. Figure 4.12 are rose plots of the flow distribution, in bin 3 (3.46 m above the bottom), by directional quadrant, divided into ten degree bins (polar angles) for both the Mud and Coral Site. At both locations, the dominant flow directions appear to be to the North East and South East, with little flow toward the North West. The speed distribution within each directional quadrant are plotted separately in Figures 4.13 and 4.14. Again, for both the Mud and Coral Site, flows to the North East and South East show a good distribution of speeds and number of occurrences, although lower magnitude values tend to dominate. For the Mud Site, speed distributions and occurrences from the North East, South West, and South East quadrants appear comparable with the Coral Site data. For the Coral Site, the histograms reflect the same North East and South East flow dominance seen in the rose plots of flow direction. While there is general agreement between the histograms for both sites, the magnitude of the flow speeds in the South West quadrant is noticeably higher at the Mud Site when compared to the Coral Site.

| Directional Quadrant | Mud Site | Coral Site |
|---|---|---|
| North East | 451 (40%) | 430 (46%) |
| North West | 79 (7%) | 93 (10%) |
| South West | 278 (25%) | 127 (14%) |
| South East | 318 (28%) | 279 (30%) |

Table 4.1: Number of mean speed data in each of the four directional quadrants (data points as a percentage of total).

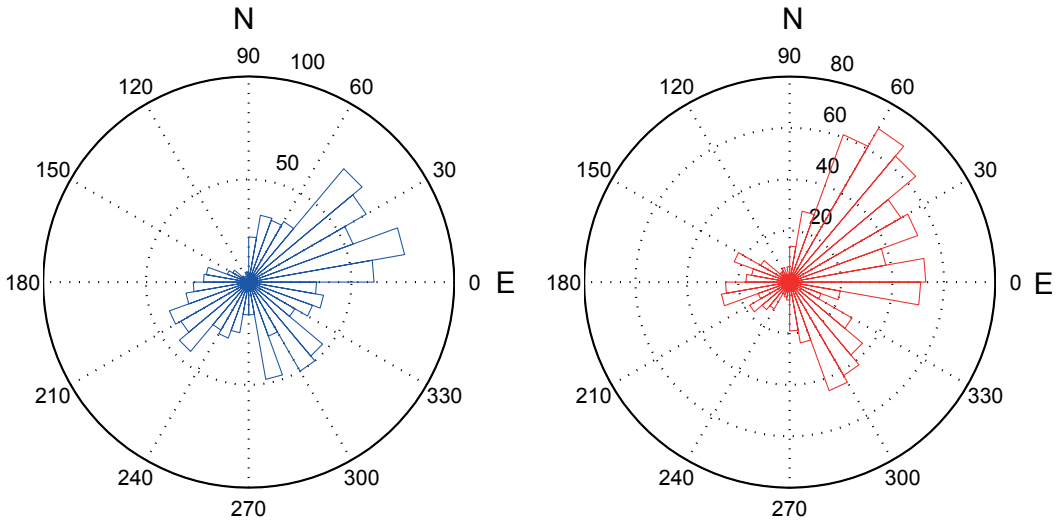


Figure 4.12: Flow distribution by directional quadrant: number of mean speed data in ten degree intervals (polar coordinates, 90 deg = True North) for the Mud (Blue) and Coral Site (Red).

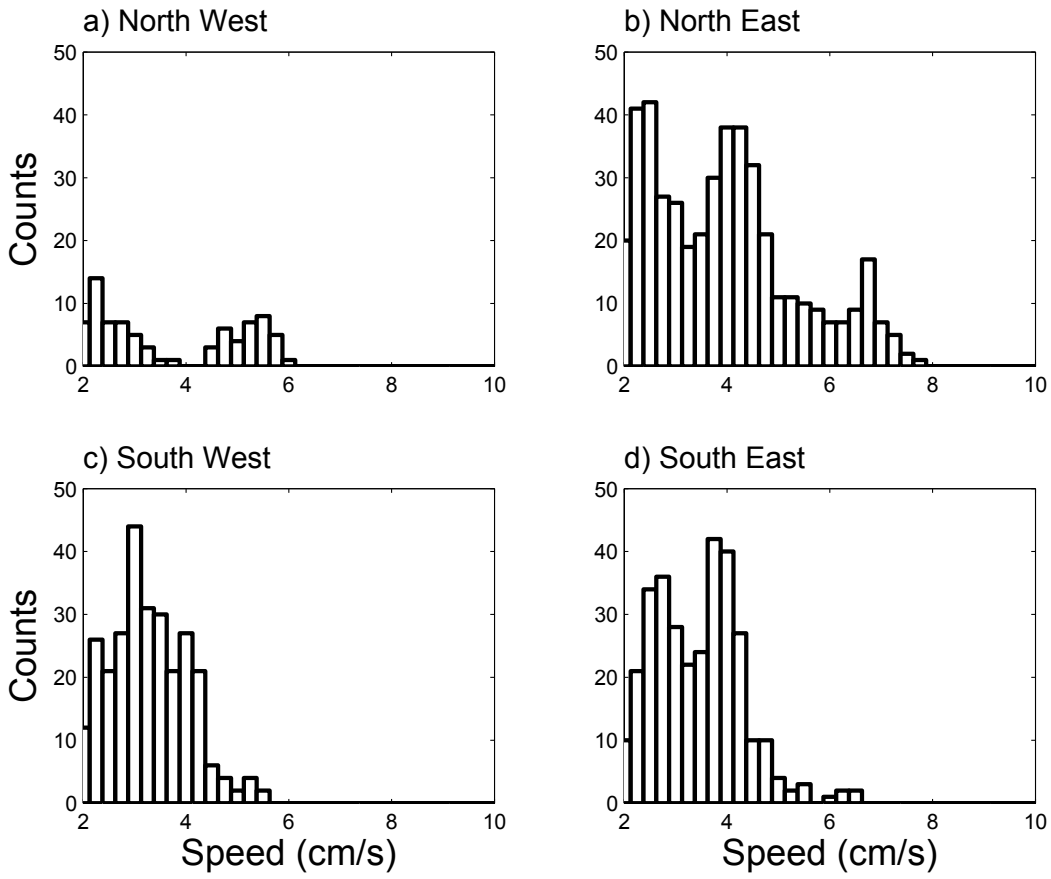


Figure 4.13: Mud Site: Histograms of mean speeds (average of mean speeds from bins 1 to 3) in each directional quadrant, speeds are binned in 0.25 cm $s^{-1}$ intervals.

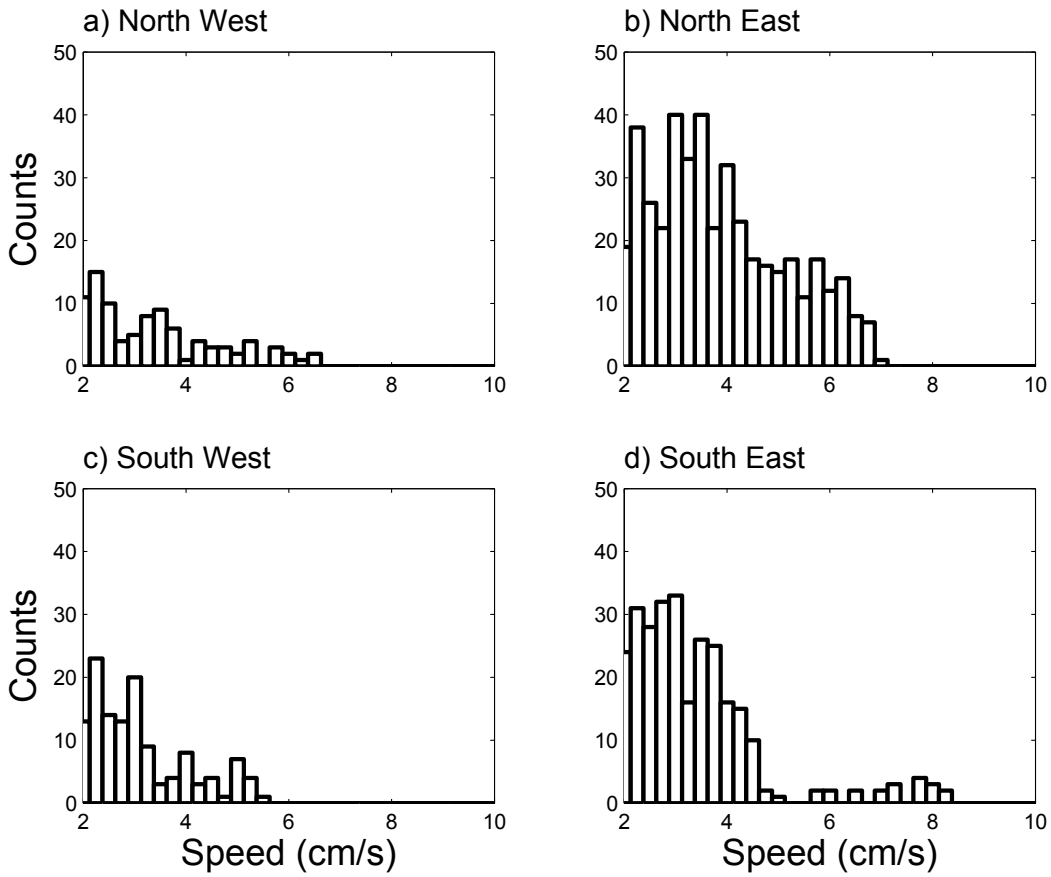


Figure 4.14: Coral Site: Histograms of mean speed (average of mean speeds from bins 1 to 3) for each directional quadrant, speeds are binned in 0.25 cm $s^{-1}$ intervals.

### 4.4.2 Speed Profiles by Quadrant

Mean speed profiles for both sites were created for the four directional quadrants; North East, North West, South West, and South East. These are shown in Figure 4.15.

Overall, speed profiles at the Mud Site, Figure 4.15 (Blue), are self similar for the North East, South West, and South East. This similarity supports the assumption of bottom homogeneity. At the Coral Site, Figure 4.15 (Red), profiles for the North East (top right) and South East (bottom right) quadrants shows speeds which are less than those at the Mud Site, which is consistent with the interpretation that the bottom boundary layer is influenced by the presence of corals. In the North West quadrant, Figure 4.15 (top left), the Coral profile is not consistent with boundary layer theory as it shows speeds at 2.46 m above the bottom which are higher than those in the bins above it (i.e. increasing speed with depth rather than the reverse). Table 4.1 and Figure 4.12 show that there is relatively little flow in the North West quadrant (7% of total flow at the Mud Site, 10% of total flow at the Coral Site), which results in significantly higher errors in those quadrants because of the poor statistics i.e. low sample size. The primary comparison is between flows to the North East and South East, where there is sufficient data and flow distribution. In these quadrants we conclude that the directional profiles at the Coral Site do show consistent evidence of increased drag due to the presence of corals. Furthermore, consistent behaviour between quadrants supports the assumption of no directional dependence in this data which is consistent with the impression of uniformly distributed corals shown in Figure 3.10.

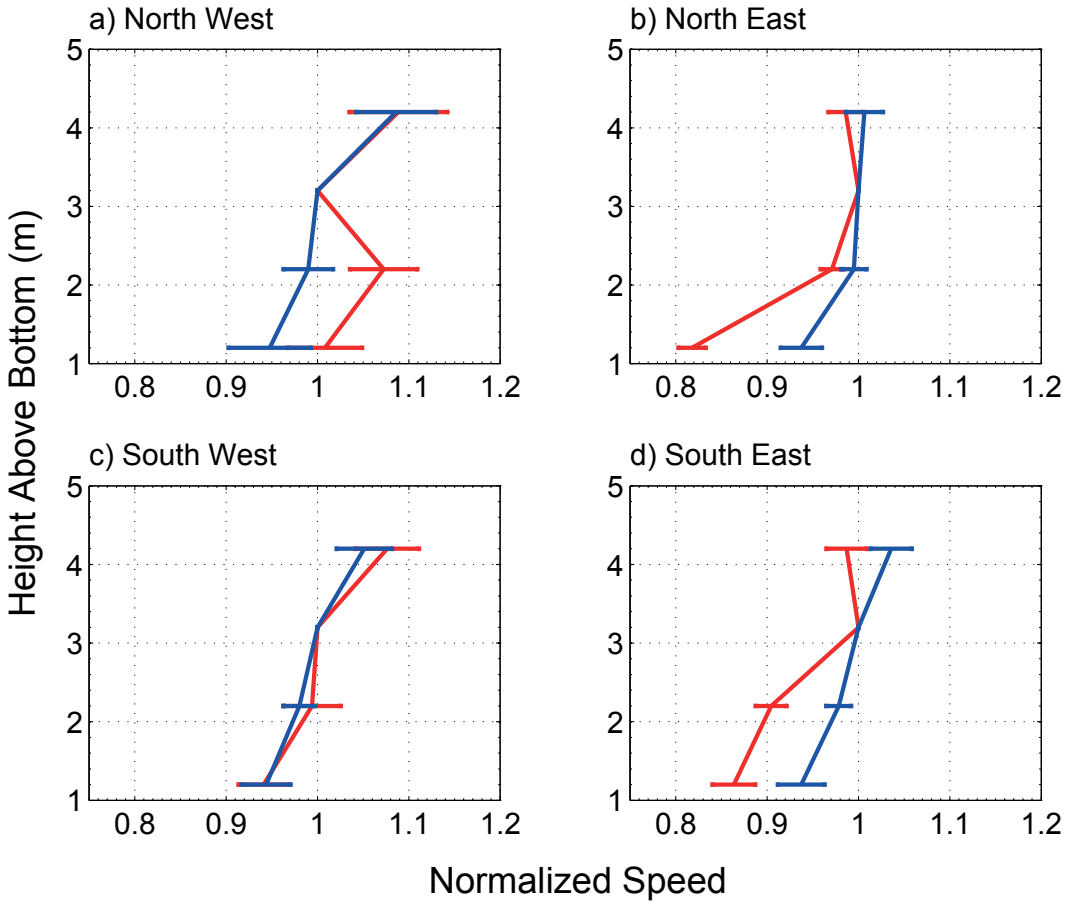


Figure 4.15: Mean speed profiles for the four directional quadrants for both the Mud Site (Blue), and Coral Site (Red); A) North West, B) North East, C) South West, and D) South East.

## 4.5 Logarithmic Regression

The logarithmic law of the wall model is used to characterize the bottom boundary layer and in particular to define the values of $u_*$ and $z_o$. Rewriting the law of the wall, according to *Cacchione and Drake* (1982) for mean speed distributions, Equation 2.9 takes the form:

$$\overline{s} = \frac{u_*}{\kappa} ln(\frac{z}{z_o}) \tag{4.13}$$

where $\overline{s}$ is the mean flow speed at height $z$ above the bottom ($z$ positive upwards), $\kappa$ = 0.41 is von Karman's constant, and $z_o$ is the bottom roughness height.

Equation 4.13 can be expanded as:

$$\overline{s} = \frac{u_*}{\kappa} ln(z) - \frac{u_*}{\kappa} ln(z_o) \tag{4.14}$$

and shows that the slope of the log-linear line is $u_*/\kappa$, from which $u_*$ can be extracted. Values of the bottom roughness height $z_o$ can then be obtained from the intercept $\frac{u_*(t)}{\kappa} ln(z_o)$. Rather than average all of the velocity data into a single profile yielding one value for $u_*$ and $z_o$, it is advantageous to create multiple profiles averaged over shorter time periods to obtain a set of values for both parameters in order to see any time dependence. Alternatively, since $u_*$ is related to the flow speed, data can be sorted by speed which allows for greater averaging of data and greater accuracy in the $u_*$ and $z_o$ estimates

### 4.5.1 Multiple Analysis Methods: Criteria for Mean Speed Profiles and Curve Fitting

*Cacchione and Drake* (1982); *Drake et al.* (1992) used time-averaged speed profiles $\overline{s}(z)$ to obtain fits to the logarithmic law. The results of these log-linear regressions of selected velocity profiles yields a time series for $u_*$ and $z_o$. This analysis method

is referred to as the Drake Approach. Two variants of the Drake Approach; the 'All Data Binned' and the 'Binned Drake' approaches, were also used to analyze the data. The results of the three techniques will be compared.

Mean speed profiles are constructed by averaging the speed data at each of the bottom four bins. It was not clear a-priori what averaging interval would be optimal, therefore four different averaging periods: 5.5, 13.75, 27.5, and 57.75 minutes, corresponding to 2, 5, 10, and 21 data point averages were examined, similar to the approach used by *Grant et al.* (1984). Profiles were discarded if the bin 3 mean speed $\overline{s_3} < 2$ cm s$^{-1}$. Fit quality was assessed based on the goodness-of-fit $Q$ value and the correlation coefficient $r^2$.

The goodness-of-fit $Q$ value is used to evaluate the agreement between the data and the fit, and is given as a value between 0 and 1. $Q$ is calculated using the Chi-Square Distribution, also known as the Chi Square Merit Function, defined for a linear regression of $y = bx + a$ as

$$\chi^2(a,b) = \sum_{i=1}^{N} \left(\frac{y_i - a - bx_i}{\sigma_i}\right)^2 \tag{4.15}$$

where $\sigma_i$ are the individual uncertainties associated with $N$ measurements of the variables $y_i$ and $x_i$. $\chi^2$ is a measure of the quality of the agreement between the data and the model (*Press et al.*, 1986), it allows for the calculation of best-fit model parameters and associated errors. In this case it is used to determine how well the individual speed profiles $x = \ln(z)$), agree with the log profile curve fitting technique.

After calculating respective best-fit model parameters, estimating uncertainties, and $\chi^2$, the incomplete gamma function $Q$ is used to provide a quantitative measure of how well the data and fit agree:

$$Q = f(\frac{\chi^2}{2}, \frac{N-2}{2}). \tag{4.16}$$

.

where N is the number of data points in the fit.

$Q$ is the probability that the calculated value of $\chi^2$ corresponding to the best-fit parameters should occur by chance. If $Q$ is larger than, say, 0.1, then the goodness-of-fit is believable. If $Q > 0.001$, then the fit may be acceptable. However, if $Q < 0.001$ then the model and/or estimation procedure could be questionable, therefore data with $Q < 0.001$ should be rejected (*Press et al.*, 1986) .

The choice of an acceptable regression coefficient ($r^2$) threshold was also examined. *Drake et al.* (1992) argued that $u_*$ and $z_o$ will have excessively large errors bars if the r value is below 0.997 ($r^2 \leq 0.994$) and therefore used only mean profiles with $r^2 > 0.994$. However, *Cheng et al.* (1999) and *Reidenbach et al.* (2006a) used profiles with $r^2 \geq 0.8$, with both groups citing acceptable results. The *Drake et al.* (1992) $r^2 > 0.994$ criteria proved too stringent in the present analysis and resulted in an unacceptably low number of profiles for use in the analysis (only 3 Coral Site velocity profiles met the $r^2 > 0.994$ criteria).

Normally, the quality of the regression statistics alone would be the primary indicator of the most appropriate time average to use. However, the availability of a larger set of $u_*$ values, resulting from a shorter averaging interval, contributes to better fit agreements and reduces error in subsequent linear regressions of $u_*$ and $\overline{s}$.

The optimal averaging interval was determined by comparing the results of the regression considering 1) the number of mean speed profiles produced from each averaging interval, and 2) the percentage of profiles having $r^2 > 0.8$ and $Q > 0.001$. The results of the comparison of the four averaging intervals for both the Mud and

| Time Interval (minutes) | No. Points Averaged | Profiles Created (Mud / Coral) (2 cm $s^{-1}$ threshold) | No. Profiles w/ $r^2 > 0.8$, Q $> 0.001$ (Mud / Coral) | % Profiles (Mud / Coral) |
|---|---|---|---|---|
| 5.5 | 2 | 376/416 | 104/141 | 28/34 |
| 13.75 | 5 | 184/185 | 60/66 | 33/36 |
| 27.50 | 10 | 96/110 | 30/44 | 27/46 |
| 57.75 | 21 | 47/59 | 24/23 | 41/49 |

Table 4.2: Comparison of averaging intervals and regression statistics for log linear fits.

Coral Site are given in Table 4.2.

It was concluded that a 13.75 minute averaging period (5 data point average) presented the best compromise between the requirements for $r^2$ and $Q$ from the logarithmic fit, and the number of $u_*$ values available for use in further analysis.

The 306 realizations of the mean speed profile at the Coral Site, resulting from a 13.75 minute (5 point) average, are shown in Figure 4.16. The four red boxes isolate one representative profile. Use of the 2 cm/s minimum speed threshold reduces the set to 185 profiles. Further thresholding these points for $r^2 \geq 0.8$ and $Q > 0.001$, results in 66 acceptable profiles for the Coral Site. It is from these profiles that estimates of $u_*$ and $z_o$ are obtained.

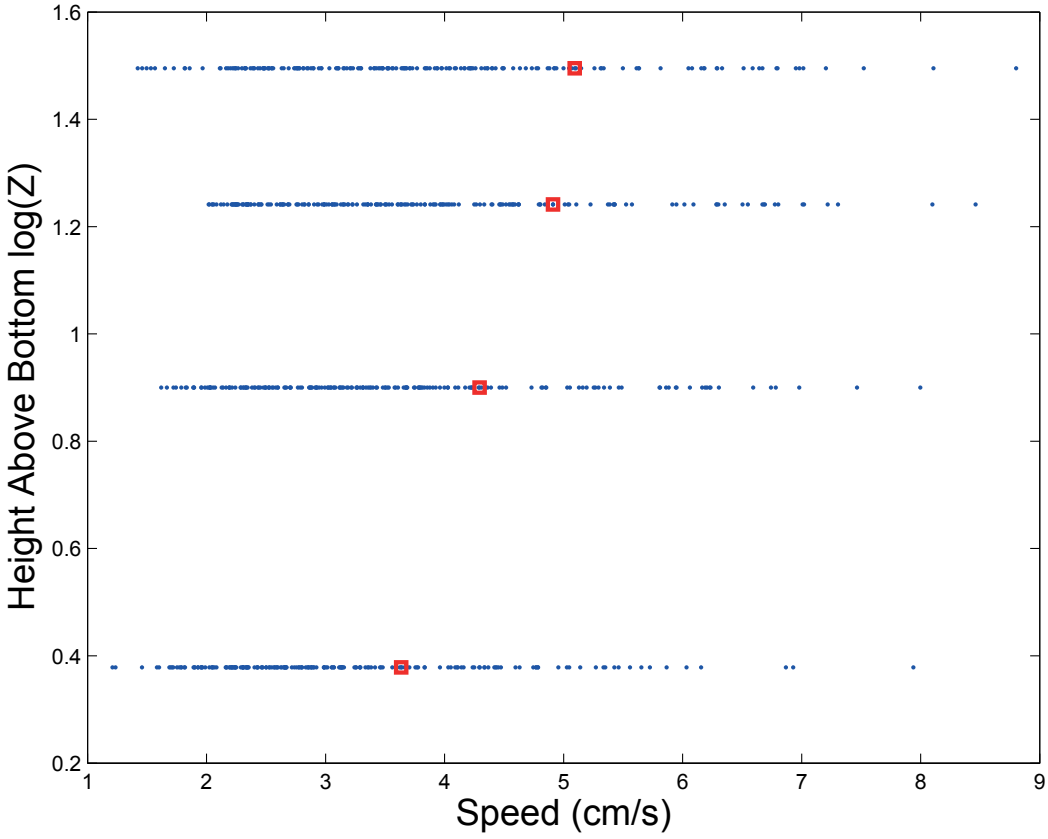


Figure 4.16: Multiple realizations of the velocity profile resulting at the Coral site. Each profile is composed of a 13.75 minute (5 point) average of the speed data, yielding a maximum of 306 profiles. The four red boxes isolate one individual profile.

### 4.5.2 Drake Approach: Results of Log-Linear Regression

Time series of $u_*$ values estimated from mean speed profiles which met the regression criteria outlined in Section 4.5.1 are shown in Figure 4.17 for the Mud Site (panel a) and Coral Site (panel b), representative speeds from bin 3 of the Coral Site are shown in panel c. At the Mud Site, on July 19, between midnight and noon, there is a gap in the distribution of $u_*$ values where no profiles meet the regression criteria. Coral Site $u_*$ values are distributed more uniformly in time suggesting no temporal bias in terms of which profiles meet the regression criteria. The mean friction velocity at the Mud Site is $\overline{u}_* = 0.46 \pm 0.20$ cm s$^{-1}$, and at the Coral Site $\overline{u}_* = 0.43 \pm 0.15$ cm s$^{-1}$. Peak $u_*$ values at the Coral Site coincide with spikes in flow speed. There are no significant differences between mean friction velocity values at the two sites.

Overall bed roughness is a complicated function of material grain size diameter at the bed interface, form drag due to bed forms, and sediment transport near the bed (*Cheng et al.*, 1999). *In situ* variable bed roughness could result from changes in bed morphology, increasing drag effects related to mean flow conditions, or various other causes. In the present case, given the short duration, no changes in bed roughness are expected. Time series of bottom roughness are shown for the Coral Site, Figure 4.18 panel a, and the Mud Site, Figure 4.18 panel b, again representative speeds from bin 3 of the Coral Site are shown in panel c. Error bars are large and have been omitted from the plot for the purposes of clarity. The mean value of the bottom roughness parameter at the Mud Site is $z_o = 11 \pm 13$ cm and at the Coral Site is $z_o = 10 \pm 10$ cm, these values appear larger than expected. Resorting the data by flow speed shows that at both locations, larger $z_o$ values are observed at low flow speeds (Figure 4.19). This variable bed roughness, and the trend toward more stable $z_o$ values with increasing flow speed was also observed by *Cheng et al.* (1999). The trend observed

in Figure 4.19 is suggestive of measurement error. Increased uncertainties at low flow speeds explain the higher corresponding roughness values, which decrease as flow speed increases. This is due to the fact that the log law profile fits are better defined at higher speeds as velocity uncertainties become a smaller proportion of the observed velocity at higher speeds. Bed roughness and bottom structure are not expected to change over the time frame involved in this experiment and given that roughness estimates at the highest speeds are most reliable, values of $z_o$ are likely well below the 10 cm level suggested in the averages shown in Figure 4.19. This behaviour is also seen by *Reidenbach* (2004), who notes that "at low flows, values of $z_o$ overestimate actual bottom roughness."

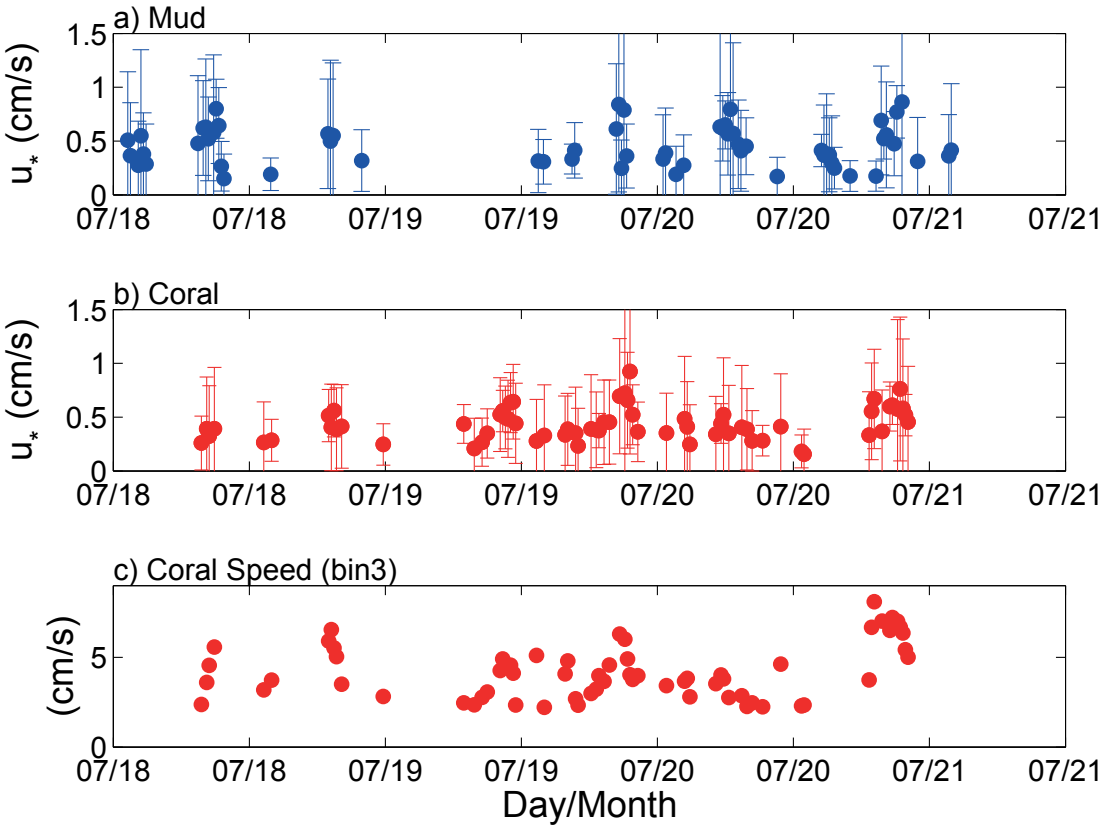


Figure 4.17: Drake Method: Time series of $u_*$ values from a) Mud Site, b) Coral Site, which meet the regression criteria, c) Coral Site representative speed in bin 3 (3.46 m above the bottom).

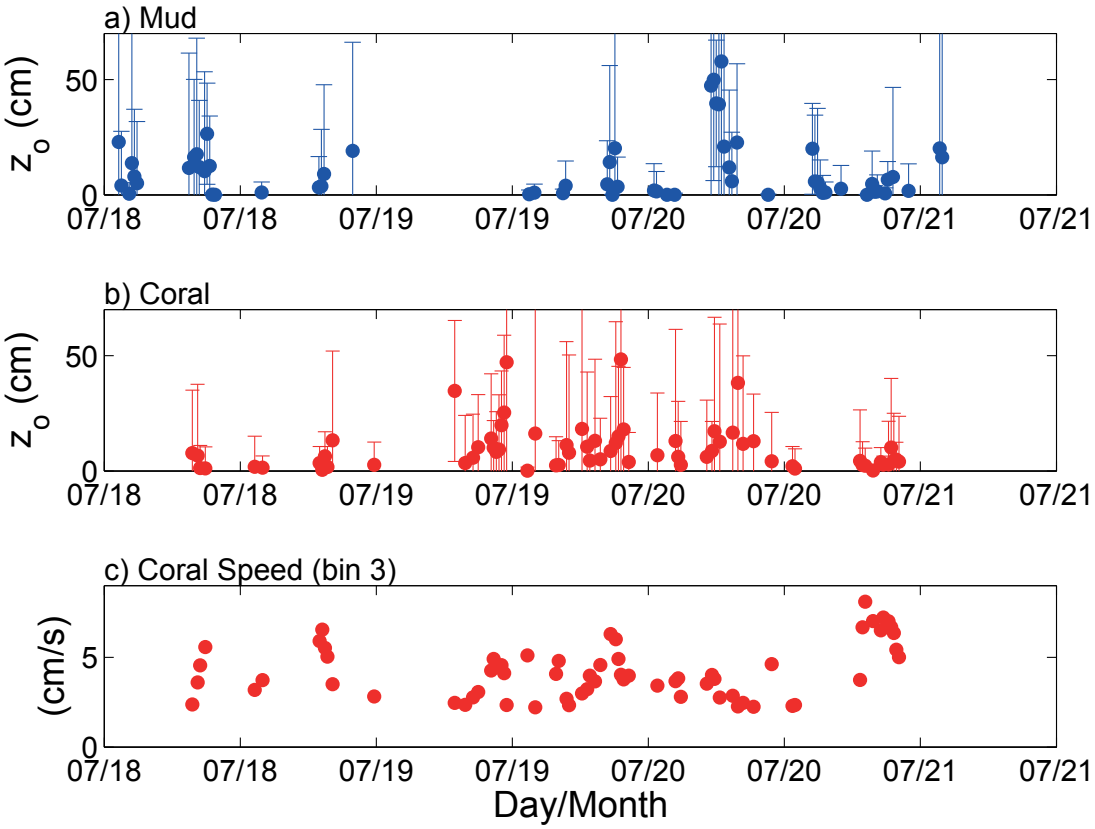


Figure 4.18: Drake Method: Comparison of bottom roughness parameters for a) Mud Site, b) Coral Site, which meet the regression criteria, and c) Coral Site representative speed in bin 3 (3.46 m above the bottom).

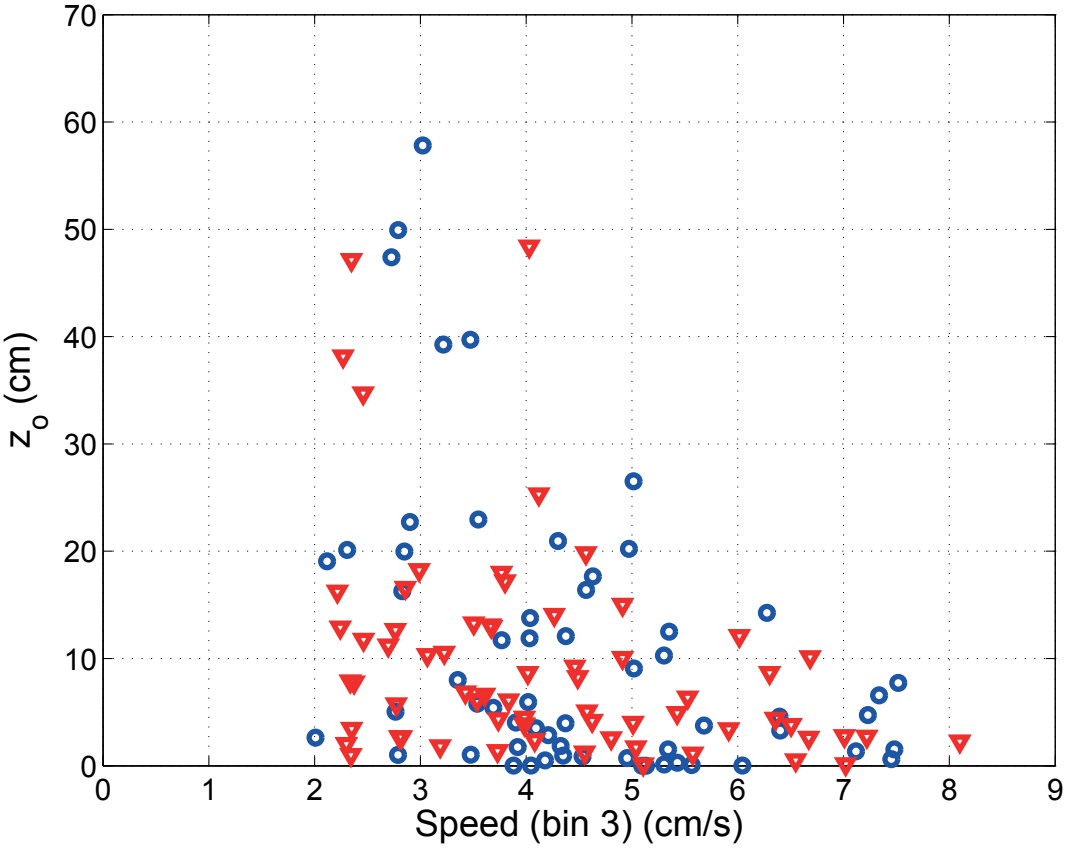


Figure 4.19: Drake Method: Bottom roughness parameter $z_o$ estimates for the Mud Site (Blue circles) and Coral Site (Red triangles).

### 4.5.3 Drake Approach: Regression of $u_*$ and Speed

The set of $u_*$ values obtained from the log-linear fit were plotted versus the mean flow speed at a height of 3.46 m and a line of best fit was found. The results are shown in Figure 4.20 for both the Mud and Coral Site. Both sites show a linear agreement between between $u_*$ and the flow speed which is consistent with the dependence of friction velocity and turbulence, on mean flow conditions. The slope at the Coral Site (slope = $0.064 \pm 0.019$) is steeper than at the Mud Site (slope = $0.047 \pm 0.032$), but the difference is not significant given the measurement uncertainty. Data at the Mud Site show more scatter and this would tend to flatten the slope of the line of best fit. The data at the Coral Site show less relative scatter and suggest the presence of a better formed bottom boundary layer. However, for this data, the Drake approach does not produce a convincing difference between the two sites in terms of turbulent effects due to the presence of corals.

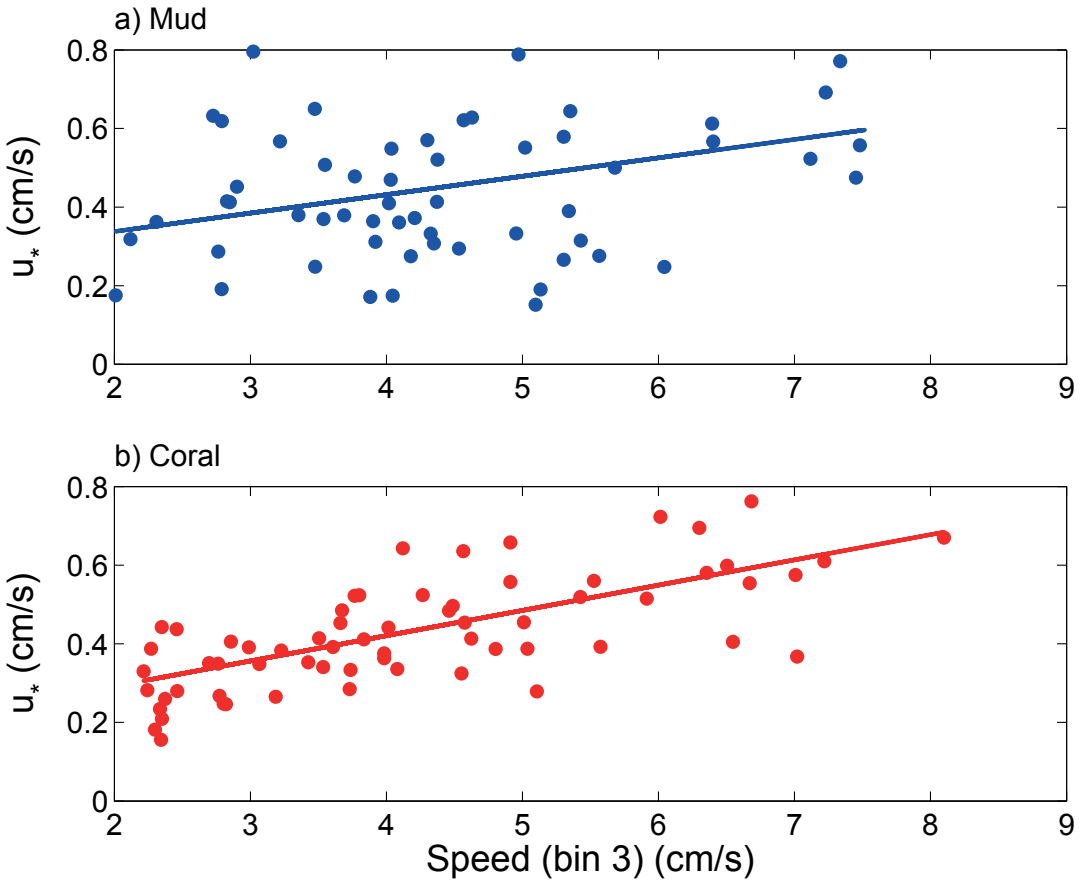


Figure 4.20: Drake Method: $u_*$ versus mean flow speed at 3.46 m above the bottom for a) Mud Site (Blue) (slope = 0.047 $\pm$ 0.032), and b) Coral Site (Red) (slope = 0.064 $\pm$ 0.019). Only friction velocity values where the log linear fit to the speed profile had an $r^2 \geq 0.8$ and $Q > 0.001$ were used in this regression. Note also that the 2 cm s$^{-1}$ minimum speed threshold is used here as well.

### 4.5.4 All Data Binned Approach

The second data processing approach, referred to as the All Data Binned Method, differs from the Drake Approach in that it foregoes temporal averaging of the speed data to produce velocity profiles. Instead, the entire speed data set is sorted into speed categories, and velocity profiles are created for each speed category. Speed data for each measurement point above the bottom are divided into speed categories based on an average of speed values from bins 1 through 3, beginning with 2 cm $s^{-1}$ and increasing by 1 cm $s^{-1}$ steps for each successive category (i.e. 2-3, 3-4, 4-5 cm $s^{-1}$, etc.). An average of bins 1 to 3 for speed category binning reduces overall uncertainty, suppresses errors from any one bin contribution and leads to a more consistent binning of the data with this larger, noisier data set. All data points in each speed category at height Z above the bottom are averaged to create a mean speed profile for each speed bin. This method of speed binning was also used by *Reidenbach et al.* (2006a) and *Lacy and Sherwood* (2004) to create average velocity profiles, as opposed to creating profile time series. The resultant speed profiles are then used in the log profile technique to obtain $u_*$ and $z_o$ parameters. While many more temporal velocity profiles are created using the Drake Approach (see Table 4.2), the number of data points averaged together to create each profile is small whereas here in the All Data Binned approach, many more individual speed data points were averaged to produce each of the five speed category velocity profiles.

The average speed profiles for five speed categories, for both the Mud Site (Blue) and Coral Site (Red), are plotted in Figure 4.21. Bottom roughness parameters for each speed range are shown for both sites in Figure 4.22. Mean $z_o$ at the Mud Site is $z_o = 0.27 \pm 0.40$ cm, and at the Coral Site is $z_o = 0.51 \pm 0.28$ cm. The bed roughness at the Coral Site is consistently higher, and does not change with speed, as compared

to the Mud Site. This difference could be due to noise alone, as higher noise biases $z_o$ upward. A comparison of the $u_*$ estimates for both the Mud and Coral Site are shown in Figure 4.23. Regression fits for $u_*$ versus speed give the Mud Site slope = 0.08 $\pm$ 0.03, and Coral Site slope = 0.06 $\pm$ 0.02. Large uncertainties in the values preclude any other meaningful analysis.

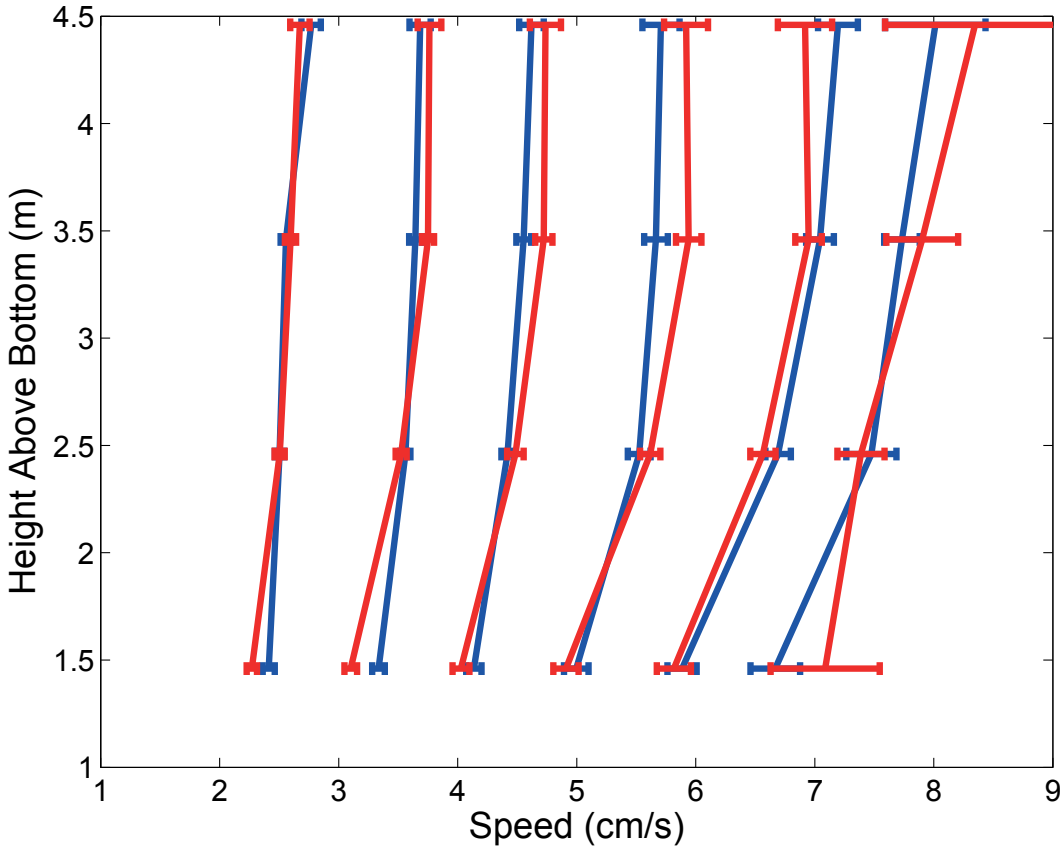


Figure 4.21: Speed profile comparison for the Mud Site (Blue) and Coral Site (Red) using the All Data Binned approach.

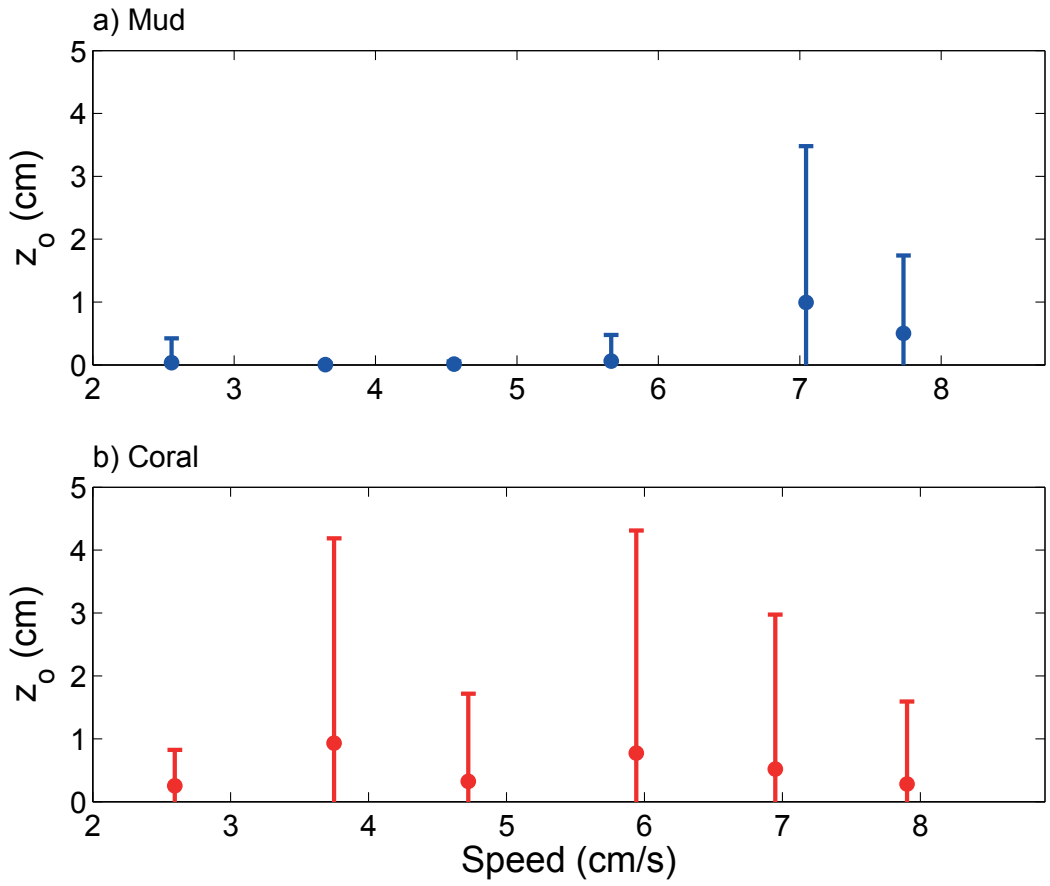


Figure 4.22: Bottom Roughness Parameters as a function of speed for a) Mud Site (Blue) mean $z_o = 0.22 \pm 0.67$ cm, and b) Coral Site (Red) mean $z_o = 0.56 \pm 2.2$ cm, using the All Data Binned Approach.

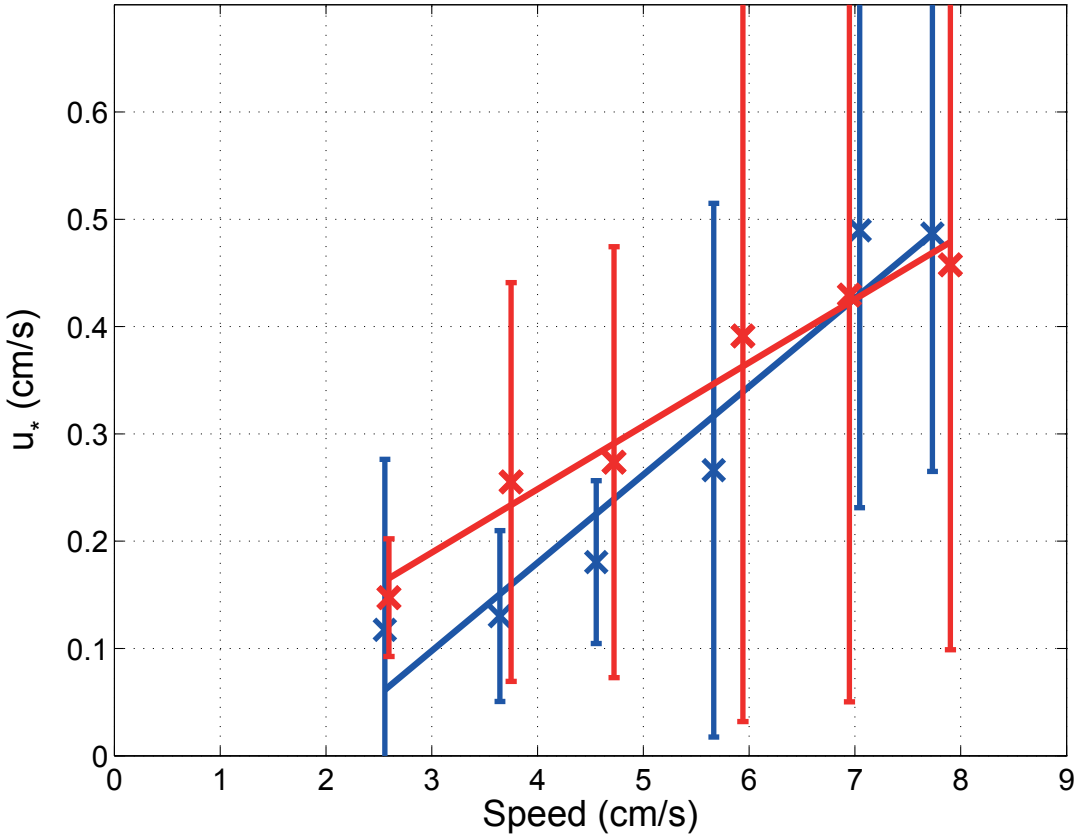


Figure 4.23: Comparison of linear regressions of $u_*$ versus bin 3 mean speeds for the Mud Site (Blue) (Slope = 0.08 $\pm$ 0.03), and Coral Site (Red) (Slope = 0.06 $\pm$ 0.02) using the All Data Binned approach.

### 4.5.5 Binned Drake Method

For the present data, the Drake approach suffered from high uncertainties due to poor data quality. The Binned Drake approach provides a means of averaging greater data to improve accuracy. A two step process is taken to the log-linear regression. Like the Drake Method, for the Binned Drake approach it was determined that the 13.75 minute average was the most acceptable interval. The 13.75 minute averaged speed data were then subjected to the same log-linear regression as in the Drake Method with the same regression criteria ($r^2 \geq 0.8$ and Q $> 0.001$). Those averaged speed data meeting the regression criteria were then selected for use as the speed data set for further processing. In effect, the initial regression step is used to inform as to which speed data will yield the best speed profiles, thereby high grading the data prior to proceeding with further processing.

The high graded speed data for each measurement point above the bottom are divided into speed categories based on the speed in bin 3, beginning with 2 cm $s^{-1}$ and increasing by 1 cm $s^{-1}$ steps for each successive category (i.e. 2-3, 3-4, 4-5 cm $s^{-1}$, etc.).

The average speed profiles for five speed categories, for both the Mud (Blue), and Coral Site (Red), are plotted in Figure 4.24. The boundary layer at both sites appears to become more well defined as the mean speed increases. Near the bottom, at low speeds, the Coral Site profiles seem to indicate lower speeds, suggesting higher drag effects.

Bottom roughness parameters for each speed range are shown for both the Mud (Blue) and Coral Site (Red) in Figure 4.25. Mean $z_o$ at the Mud Site is $z_o = 2.5 \pm 2.1$ cm, and at the Coral Site is $z_o = 6.5 \pm 4.2$ cm . Data at the Mud Site suggest that bottom roughness increases as a function of speed, while roughness values at the Coral

Site are higher at lower speeds. However, uncertainty increases with speed at the Mud Site, while at the Coral Site uncertainty were more uniform with speed. Given that larger uncertainties lead to larger $z_o$ values, the trends here might be driven by these uncertainty values. There is significant error in the bottom roughness estimates due to the combined uncertainties associated with the calculation of $z_o$ from the log profile technique. Since estimates of $z_o$ depend on both the slope and intercept of the log fit the associated errors in both contribute to higher uncertainties in bottom roughness. Bed roughness values at the Coral Site are generally higher at low speeds compared to the Mud Site, possibly indicating that the coral are affecting the hydrodynamic roughness at low speeds. As in the Drake Method, friction velocity ($u_*$) values are plotted against the speed data (bin 3 mean speeds), shown in Figure 4.26. Rather than plotting $u_*$ against a bin centered value, $u_*$ is plotted against mean bin velocity for the bin profile category. Notice in Figure 4.26, at higher speed categories, where there is less data in the bin category, the mean speeds do not fall at the middle of the speed bin, as the distribution of speeds within the bin is not uniformly centered within the bin. Regression fits for $u_*$ versus bin 3 mean speeds give the Mud Site slope = 0.1 $\pm$ 0.04, and Coral Site slope = 0.07 $\pm$ 0.06. While $u_*$ values for six speed categories are shown in Figure 4.26 for the purposes of completeness, for the Coral Site, only the first five data points are used to calculate the line of best fit. The data point for the highest speed category (7-8 cm $s^{-1}$) was not included in the fit calculation due to excessively large error bars. At low speeds, $u_*$ values at the Coral Site are consistently higher compared with the Mud Site, indicating increased turbulence due to the presence of coral.

The advantages of the Binned Drake approach compared with the Drake Method are that the initial regression step in the Binned Drake approach is used to pre-screen the speed profiles based on the regression criteria. This pre-screening provides better

quality data for the log-linear fit and thus more confidence in the resulting parameters. The binning of this high graded speed data based on speed ranges then allows for the averaging of more data into a single profile which should provide a better fit to the law of the wall, compared with a mean speed profile based on a temporal average of a smaller number of points.

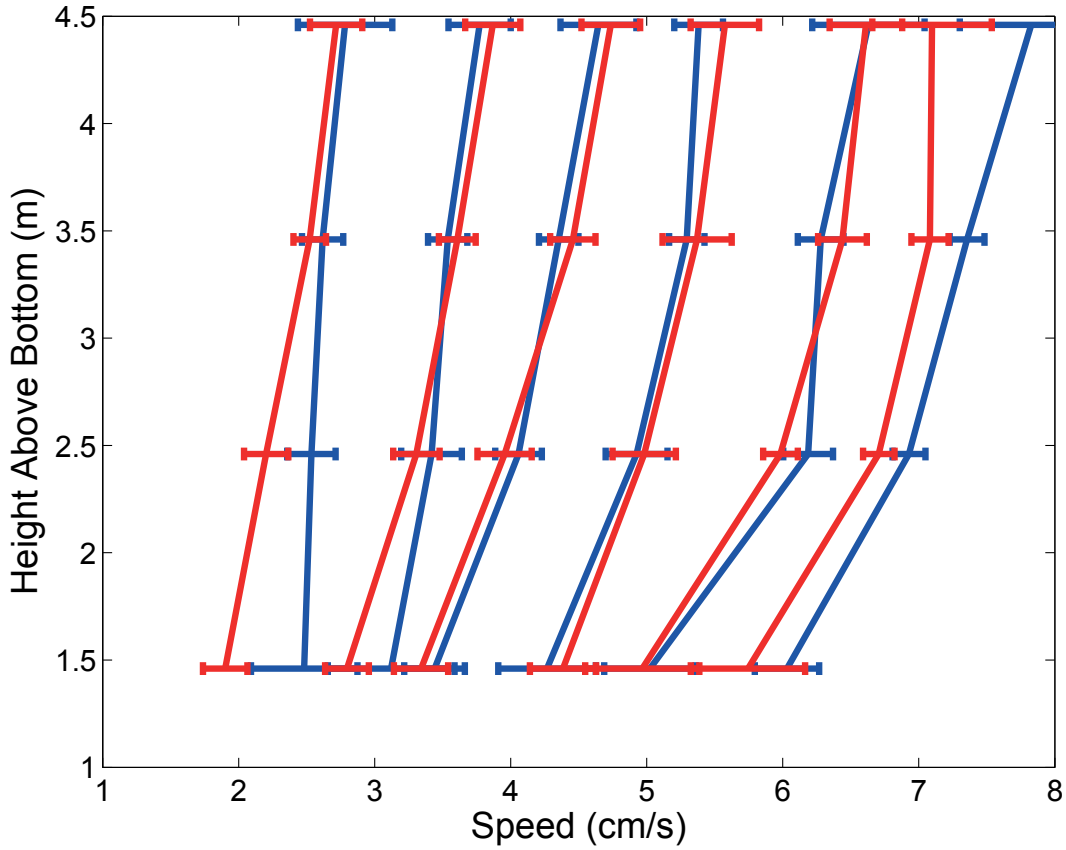


Figure 4.24: Binned Drake Method: Comparison of speed profiles for each speed category for both the Mud Site (Blue) and Coral Site (Red).

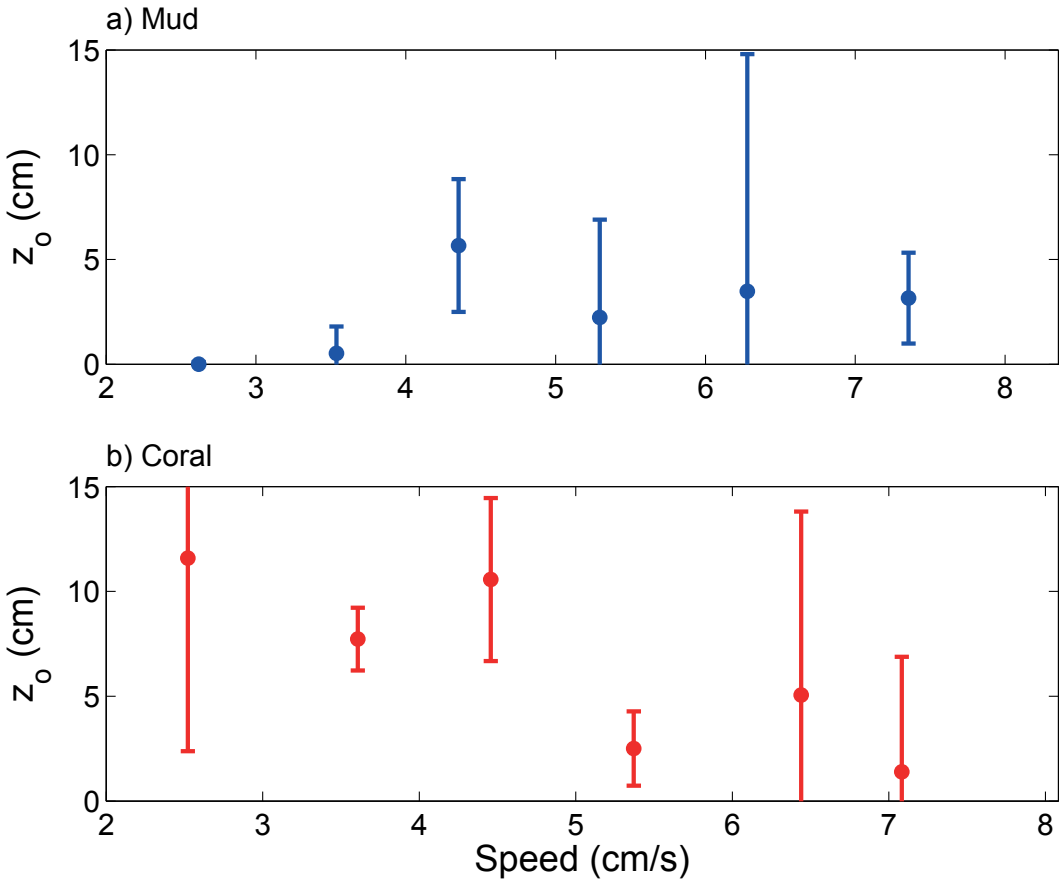


Figure 4.25: Binned Drake Method: Bottom Roughness Parameters as a function of mean speeds in bin 3 for both the Mud Site (Blue) and Coral Site (Red).

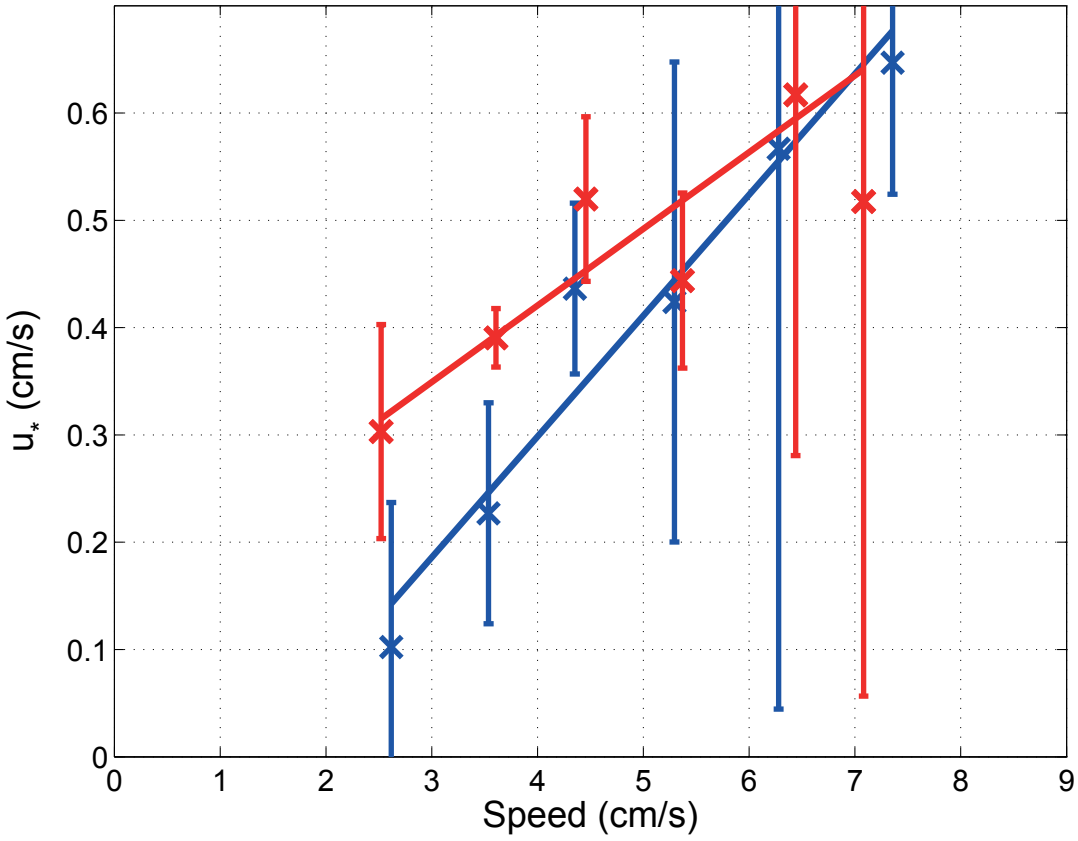


Figure 4.26: Binned Drake Method: Comparison of linear regressions of $u_*$ versus bin 3 mean speeds for both the Mud Site (Blue) (Slope = 0.1 $\pm$ 0.04), and Coral Site (Red) (Slope = 0.07 $\pm$ 0.06).

## 4.6 Comparison of All 3 Methods

Results of $u_*$ versus speed bit fits from all three methods are shown in Figure 4.27. Panels a and d are results of the Drake Method, (Mud Site (Blue) and Coral Site (Red)), b and e the Binned Drake Method, and c and f are the All Data Binned results. The Coral Site fits are also plotted as a red dashed line on the Mud Site panels to aid in comparison. At low speeds, $u_*$ values are consistently higher at the Coral Site, suggesting increased turbulence relative to the Mud Site. As flow speeds increase, the enhancement of turbulence due to the coral structure appears less significant, as friction velocities at both sites appear more closely matched, with less appreciable difference between the two sites.

## 4.7 Comparison of Results from studies in other Cold-Water Coral Areas

At the time of the deployment and recovery of instruments in Haddock Channel described in this thesis there were admittedly few studies or reports involving direct in situ current measurement within cold-water and or deep-water coral areas (thickets, reefs, carbonate mounds) however several studies have since been published detailing such measurements in relation to understanding coral habitat characteristics, food supply mechanisms, and coral impacts on the bottom boundary layer and current regime. The primary hot spot for this type of deep-water coral research has been the Northeast Atlantic, with current measurements obtained on or above coral mounds, reef complexes, and submarine canyons off the coast of Ireland, Scotland, Norway, and France (*Duineveld et al.*, 2007; **?**; *Lavaleye et al.*, 2009; *Guihen et al.*, 2013; *Khripounoff et al.*).

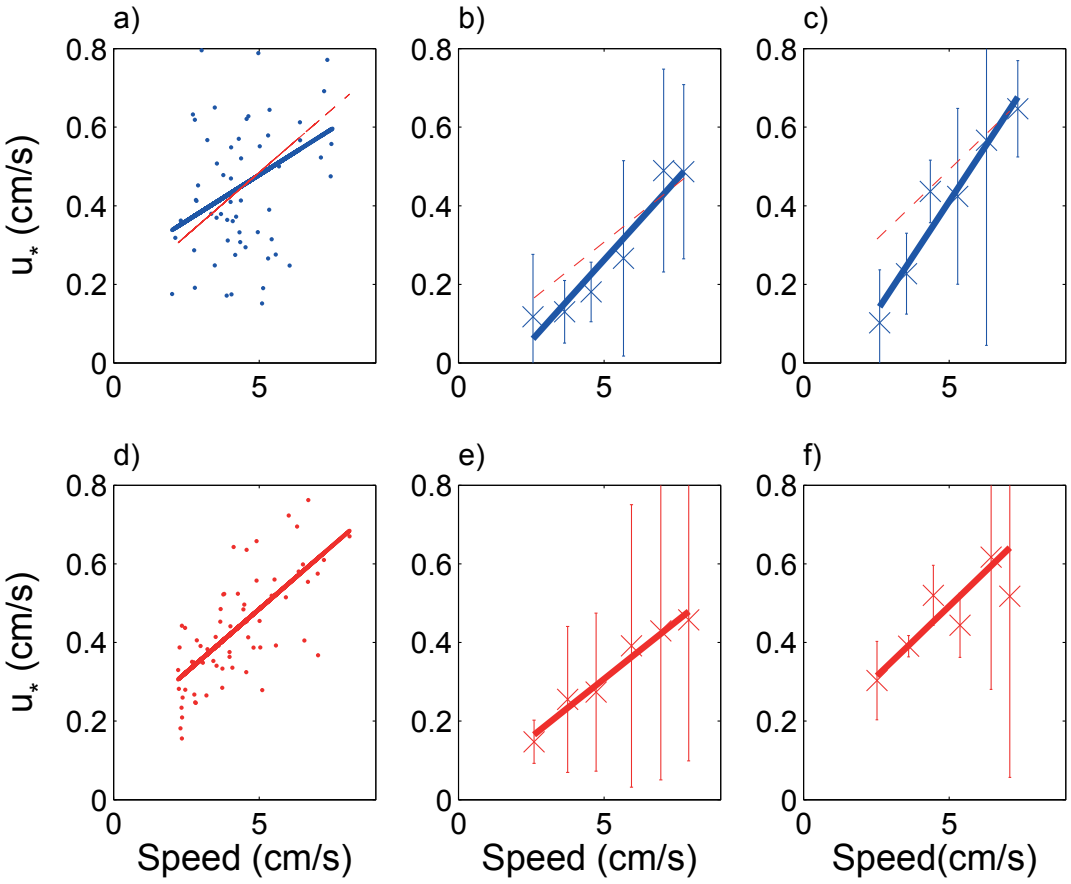


Figure 4.27: Comparison of fits of $u_*$ versus speed from a) & d) Drake Method, Mud (Blue) Coral (Red), b) & e) All Data Binned, and c) & f) Binned Drake. The Coral Site fits are also plotted as a red dashed line on the Mud plots to aid in comparison.

Additionally, in the Gulf of Mexico, at least one set of direct current measurements using an ADCP have been obtained around cold-water corals in the Gulf of Mexico as part of proof of concept instrumentation platform (mini-lander) deployment (*Fogel and Dullo*, 2011). This study involved a short (28 hour) deployment of an upward looking ACDP in which four distinct current direction phases were observed.

*Duineveld et al.* (2007) reports on the trophic structure of a cold-water coral mound community of *Lophelia pertusa* and *Madrepora oculata* in Rockall Bank, NE Atlantic, with relation to the near-bottom particle supply and current regime. As with the experiment described in this thesis, previous current data on the cold-water coral area was limited. As part of the *Duineveld et al.* (2007) study the differences between bottom currents over coral mounds and non-coral sites (gully or plain) were examined. For the study point source current measurements were collected using a Aanderra current meter situated 0.5 m above coral mound (depth 750-778 m), attached to a benthic lander. The authors report that near bottom current speeds on the coral mound were lower than in the non-coral habitat (**?**). The most frequent near bottom current speeds observed were between 2 and 10 cm $s^{-1}$ (*Duineveld et al.*, 2007). The authors suggest that more moderate currents on the coral mound, relative to the gully or plain areas could be the result of flow deceleration by the dense coral framework. They also did not find substantial differences in turbidity between the coral mound and non coral sites *Duineveld et al.* (2007). The authors also indicate that their results may point to an optimum intermediate current speed for feeding cold-water corals. The authors also state that the similarity in suitable coral substrate in the non-coral areas, as well as the observed reduction in flow speeds on the coral mound, suggests that the higher current speeds in the non-coral areas prevent coral from colonizing off-mound habitat.

At present the studies situated on the coral reef carbonate mounds in the Skagerrak

Strait area of Norway (Tisler Reef) offer the best opportunity for boundary layer flow dynamics comparison they also used the logarithmic law of the wall approach for data analysis Guihen2013,Lavaleye2009. Unlike the work described in this thesis the authors were able to use two different approaches to estimating the magnitude of the near seabed shear stress (friction velocity), the first being the logarithmic law of the wall approach and the second being direct measurement of the Reynolds stress, with results being comparable for both approaches. *Guihen et al.* (2013) found that for any given flow speed, higher shear stresses were observed within the live coral area than in the area comprised of dead coral. Acoustic backscatter data was also used as a proxy for relative suspended particulate matter concentrations. The results indicated that re-suspension of suspended material was more likely to occur in the live coral area. *Guihen et al.* (2013) indicate that the high measured shear stress inside the coral area may enhance the level of re-suspension for a given flow speed, thereby providing more food for the corals.

# Chapter 5

# Backscatter Intensity and Suspended Material

## 5.1 Introduction

The doppler shift of the acoustic backscatter signal is used by the Doppler Profiler to determine the velocity of the water. Signal amplitude or backscatter intensity can be used as a proxy for estimating the concentration and size of suspended material such as organic matter, sediment, or other particulates, in the water column. As flow speeds increase, turbulence is expected to increase. This increase in turbulence can result in resuspension of material on the bottom into the water column, leading to higher backscatter amplitudes. Increased backscatter intensity as a function of flow speed may therefore result from an increase in turbulent activity. Such events are important because they may influence the amount of organic material available to be captured by coral polyps as well as highlighting the coral structure's ability to induce turbulence and therefore impact available the food supply.

## 5.2 Calibration of Backscatter Intensity

Acoustic backscatter data must be calibrated in order to estimate the suspended material in the water. Relative calibration involves first converting the data from the internal instrument units of backscatter (counts) to a linear or log scale (decibels) using an instrument specific conversion factor. Secondly, the data must be normalized by range to account for the attenuation of signal amplitude due to 1) acoustic spreading of the signal as it propagates through the water column, 2) water or chemical absorption of the signal, and 3) particle attenuation.

From *Lohrmann* (2001), the amplitude of the range normalized echo level (EL) or backscatter, in units of dB, is approximately:

$$EL = 0.43A + 20log_{10}(R) + 2\alpha_w(R) + 20R\int \alpha_p dr \tag{5.1}$$

where $A$ is the instrument recorded amplitude in counts, 0.43 is the conversion factor in dB/count, R is the range in meters along the transducer beam, $\alpha_w$ is the absorption coefficient due to water, and $\alpha_p$ is the loss due to particle attenuation.

The second term in Equation 5.1 represents spherical spreading, which is a purely geometric effect due to reduction of intensity as the scattered signal propagates away from the scatterers. Spherical spreading loss associated with propagation toward the scatterers (i.e. away from the transducer), is countered by an increase in sample volume.

The third term represents water or chemical absorption, this occurs due to the change in pressure associated with the propagation of sound through the water. As the signal propagates through the water energy is lost as the water is compressed. The salt magnesium sulfate and its ions, and to a lesser extent boric acid, are the predominant contributors to the absorption of sound in seawater (*Medwin and Clay*,

1998). The magnesium sulfate, boric acid, and their respective ions, exist in equilibrium in the water, which is dependent upon temperature and pressure. Chemical relaxation occurs when magnesium sulfate and boric acid undergo an equilibrium shift, due to the change in pressure, from salt to ions (ionic dissociation), and then return to equilibrium. The factor of 2 in the third term takes into account the fact that signal attenuation occurs twice: once as the outgoing signal propagates away from transducer and again when the backscatter signal returns.

The fourth term in Equation is 5.1 is amplitude loss via particle attenuation. If the number of scatterers in the water column is high, the amplitude of the signal will be reduced significantly due to increased scattering and absorption of acoustic energy by the particles. At low concentrations of suspended material, particle attenuation is small and the last term in Equation 5.1 can be ignored.

## 5.3 Backscatter and Speed

Comparison of the backscatter intensity as a function of speed at the Mud, and Coral sites is useful for understanding how the coral thicket structure affects the turbulent characteristics of the local bottom boundary layer. Figure 5.1 shows the normalized backscatter for the Mud (Blue), and Coral (Red) Site. Backscatter intensity values used in Figure 5.1 are an average from all three transducer beams. Speed data was sorted into 1 cm $s^{-1}$ bins, backscatter values in each speed category were sorted into corresponding bins. Binned data were then averaged to yield a mean backscatter value for each speed category. Mean backscatter values were normalized by subtracting the value of the backscatter in the first bin. The resulting plot indicates backscatter values relative to levels at the lowest speed (2.5 cm $s^{-1}$).

In Figure 5.1 backscatter intensity increases more quickly at the Mud Site than

at the Coral Site. This does not indicate the presence of greater concentrations of suspended material at one site versus the other since absolute calibration of the instruments has not been possible. In fact, this behaviour is consistent with the results from the friction velocity analysis, which shows friction velocity increasing faster with flow speed at the Mud Site relative to the Coral Site (see Figure 4.27). Below 7 cm $s^{-1}$ there is clearly an increase in scattering at both sites associated with increased flow speeds which is indicative of increased resuspension of material, with more resuspension at the Mud Site relative to the Coral Site for a given speed. Above 7 cm $s^{-1}$, the backscatter at the Coral Site increases significantly relative to the Mud Site which decreases.

Events occurring above 7 cm $s^{-1}$ are tantalizing, and suggestive of something happening at the Coral Site. It appears as if a trend becomes apparent in the last two data points (highest speeds), with backscatter increasing rapidly as speed increases at the Coral Site, and decreasing backscatter at the Mud Site. Either this is caused by insufficient sample size; limited backscatter data quantities in the two highest bins, or at these speeds we enter a new flow regime. If we presume that the data is accurate above 7 cm $s^{-1}$, there is evidence of a different flow regime with backscatter increasing at the Coral Site and decreasing at the Mud Site. It is worth noting that the graph might mix flow speed and flow direction such that speed data in one interval (i.e. 7-8 cm $s^{-1}$), might all come from the same period in the speed data set.

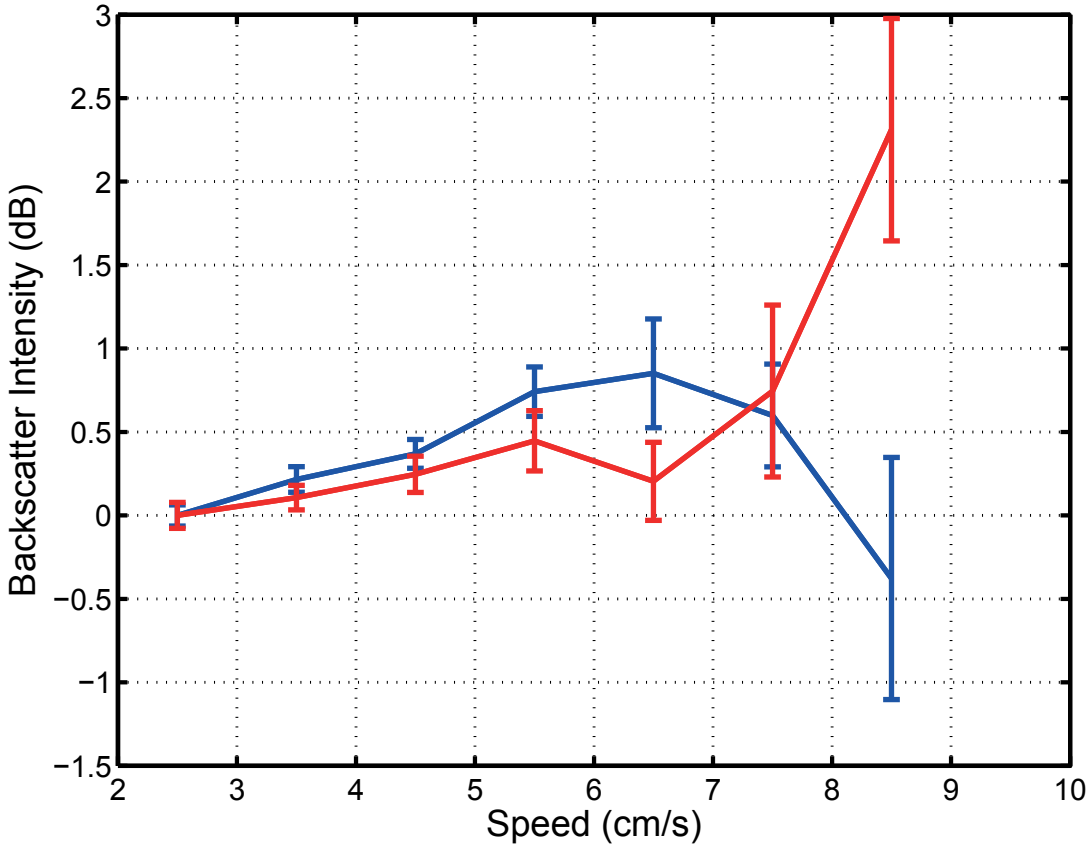


Figure 5.1: Relative backscatter intensity versus speed for both the Mud (Blue), and Coral Site (Red). Error bars are 95% confidence intervals. Only two backscatter data points were averaged in the highest speed bin for the Mud Site, and eight data points averaged for the Coral Site, compared with 396 and 349 backscatter points for the lowest speed bin, for the Mud and Coral sites, respectively.

# Chapter 6

# Conclusions

The work presented in this thesis is part of a larger, ongoing study of deep sea corals and their habitat in Atlantic Canadian waters. Deep sea corals have been identified as important parts of the marine ecosystem, both in terms of the diversity of coral species, and serving as habitat for other species, which also contributes to increased ecosystem bio-diversity. The need to better understand all aspects of deep sea corals is driven not only by pure scientific pursuit, but also to inform policy makers involved in conservation efforts intended to protect deep sea corals and their habitat.

Since deep sea corals are benthic organisms, their interaction with currents in the bottom boundary layer is an important factor for understanding many aspects of their biological and physical processes. As well, understanding the structure and flow of bottom currents is necessary for predicting which areas may be suitable habitat for a given coral species. The interaction of bottom currents with the characteristically rough topography of coral reefs and thickets allows for the application of turbulent bottom boundary layer theory to determine if, and how, the coral influence the local current regime, which as stated, has implications for biological aspects of coral ecology such as nutrient supply and uptake. An experiment was carried out in Haddock

Channel, Southwest Grand Banks, off the coast of Newfoundland, to characterize the bottom boundary layer in an area containing the deep water coral species *Keratoisis ornata* (now synonymized with *Keratoisis grayi*).

Two Doppler Profilers were deployed via remotely operated vehicle (ROV) to make measurements of the bottom boundary layer currents; one instrument was placed in an area characterized as suitable coral habitat, but containing no corals (Mud Site), the other in a *Keratoisis ornata* thicket (Coral Site). This arrangement allowed for a comparison of the bottom boundary layer with and without the presence of deep water corals. The two primary questions we sought to answer were:

*1. Based on the values of the flow parameters, does the local bottom boundary layer at the Coral Site agree with the logarithmic "law of the wall" theory which is used to describe turbulent boundary layers?*

*2. Does the presence of corals and their characteristic roughness affect the velocity profile, friction velocity, and mixing properties in a turbulent bottom boundary layer flow?*

The instrument deployment was limited to three days due to the need to recover the Doppler Profilers via ROV and the available ship time schedule. The short deployment allowed for a comparatively high sampling rate, but unfortunately, this high sampling rate gave rise to data collection and data quality issues. Specifically, because of the short deployment time the instruments were configured for maximum high sampling rate, necessitating higher demands on the instrument power supply and less time for battery cell chemistry recovery. Ordinarily, this high duty cycle would not be a critical issue, however, because the battery chemistry is sensitive to low temperatures, such as those in the cold water environment ($4°C$) of the Grand Banks, the batteries were eventually unable to maintain adequate voltage levels leading to a change in sample intervals and unusable data.

The Doppler Profilers were configured to collect one profile every five seconds (12 profiles per minute, later averaged to one profile every 2.7 minutes) with data in 1 meter depth bins, eight bins total. Due to backscatter conditions and the instrument configuration, the maximum number of useable bins came to 4 and often, depending on the backscatter conditions, only 3 bins provided usable data. Bin 4 data was identified as acceptable if backscatter levels were above a minimum intensity threshold.

An additional data quality issue that arose was the presence of an obvious velocity offset in the first data bin of transducer beams 1 and 3 on the Mud Site Doppler Profiler (AQD1): this bias was removed by making the mean (component of velocity measured by the beam) velocity in bin 1 (centered about 1.46 meters above the bottom) to be consistent with the mean velocity in bin 2 of affected beams. This approach assumes that the mean (component) velocity is consistent with depth: obviously greater speeds are seen at greater heights above the bottom, but with the observed average component speed near zero, this approach should reasonably remove the observed bias.

Mean velocity profiles for both the Mud and Coral Site show velocity decreasing as a function of depth, as expected. Normalized speeds at the Mud Site appear higher than those at the Coral Site for the lowest two bins, suggesting possible drag effects due to the presence of corals. Overall, the two profiles did not reveal significant insight into differences between the two locations.

Although data was collected at only two sites, it was possible to simulate conditions at locations with different mean flow conditions by sorting the data according to direction. Velocity profiles for four directional quadrants were examined. At the Mud Site, speed profiles in three of the four quadrants are generally self similar for the North East, South West, and South East which supports the assertion of bottom homogeneity. At the Coral Site, speed profiles in the North East and South East are

considered accurate due to sufficient directional data (percentage of total data set) and good distribution of speeds over a range of values. Comparison of flows at both sites for the North East and South East quadrants show evidence of increased drag due to the presence of corals (see Figure 4.15). Overall, consistent behaviour between quadrants supports the conclusion that there is no strong directional dependence in this data at either site.

Once the data had been sorted for quality, three different averaging and data sorting approaches, labeled the Drake Method, the All Data Binned Method, and the Binned Drake Method were explored. The basic objective was to create velocity profiles averaged or sorted in some way so that the resulting profile could be fit to the law-of-the-wall profile thereby extracting friction velocity $u_*$ and bottom roughness values $z_o$.

In the Drake Method, profile quality was assessed based on the number of velocity profiles with acceptable correlation coefficients $r^2$ and goodness-of-fit $Q$ values. Data was averaged over 5.5, 13.75, 27.50 and 57.75 minute intervals. More averaging creates smoother overall data, but provides fewer profiles for further analysis. The final analysis was based 13.75 minute averaging intervals which was the optimal compromise between the number of velocity profiles and the requirements for high $r^2$ and $Q$, which, when combined with other data high grading criteria, yielded 60 velocity profiles for the Mud Site and 66 for the Coral Site. Profiles were then fitted to the law of the wall to obtain friction velocity and bottom roughness parameters for each individual profile. To demonstrate that $u_*$ evolves with flow speed as expected and is consistent with independent observations (*Reidenbach et al.*, 2006a), the friction velocity estimates were then regressed against speed.

Results from the Drake Method showed little differentiation between the Mud and Coral Site and it is not convincing in terms of the impact of coral presence

on boundary layer flows. Friction velocity and bottom roughness parameters are comparable at both locations. There is significant uncertainty in parameters at both sites and $z_o$ values are likely overestimated: it is mathematically impossible to have negative $z_o$ values so noise leads to a bias toward larger $z_o$ values. Regression of friction velocity against speed for both sites does show a linear agreement between $u_*$ and speed. This is consistent with the dependence of friction velocity and turbulence on mean flow conditions, and supports agreement with the law of the wall theory.

In the All Data Binned Method, temporal averages are eschewed in favour of sorting all the speed data for each measurement bin into five speed categories based on the average speed from the bottom three measurement bins. Velocity profiles are then created by averaging data from each speed category for each of the four measurement bins. An average of bins 1 to 3 is used for sorting to reduce overall uncertainty and suppresses errors from any one bin contribution. Resulting profiles are then fitted to the law of the wall using the log profile regression technique. While the number of profiles created is small (i.e. only five speed categories), the number of data points averaged together to create each profile point is an order of magnitude higher than in the Drake Method.

The All Data Binned Method yields bottom roughness values that are consistently higher at the Coral Site (mean $z_o = 0.51 \pm 0.28$ cm), compared to the Mud Site (mean $z_o = 0.27 \pm 0.40$ cm). As for analysis of friction velocity, the fit of $u_*$ and speed shows that friction velocity values are higher overall at the Coral Site for low speeds, but $u_*$ increases faster at the Mud Site as speed increases. These differences are not significant given the stated uncertainties.

In the Binned Drake Method, speed data are again sorted into speed categories to produce speed profiles. The Binned Drake approach relies on sorting speeds based on the mean speeds in bin 3. This sometimes results in entire speed profiles being binned

into the wrong speed category as bin 3 speeds by themselves suffer measurement uncertainties. At times, the corresponding values at other measurement heights would actually indicate an overall higher speed category for the data. An average of bins 1 to 3 was considered but was shown to yield no appreciable improvement in the final analysis. Average speed profiles at the Coral Site show lower speeds relative to the Mud Site near the bottom, suggesting higher drag effects due to the presence of Corals. Bed roughness values at the Coral Site are generally higher at low speeds compared to the Mud Site, possibly indicating that the coral are affecting the hydrodynamic roughness at low speeds. Friction velocity values plotted against speed (Figure 4.26) show that at low speeds, $u_*$ estimates are consistently higher at the Coral Site; Mud Site $u_*$ values are $\sim 30\%$ to $80\%$ of Coral Site estimates, again pointing to increased turbulence due the presence of coral. However, friction velocity increases faster at the Mud Site (Slope $= 0.1 \pm 0.04$) compared to the Coral Site (Slope $= 0.07 \pm 0.06$) as speeds increase, suggesting that at higher speeds coral induced bottom roughness is less important to friction velocity. The Binned Drake method results in the lowest overall error in the fits and was considered the most reliable of the three approaches used to analyze the data. While the All Data Binned method supplied more data for the analysis, the quality of data in the Binned Drake method resulting from a more rigorous screening process yields marginally better results.

The All Data Binned and Binned Drake method both show the same trend of higher friction velocities at low speeds at the Coral Site, with $u_*$ increasing faster at the Mud Site. The higher $u_*$ values at low speeds at the Coral Site are consistent with the hypothesis that enhancement of turbulence due to coral structure is significant only at low flow speeds, enabling coral polyps greater opportunities to extract organic material from the water column i.e. improving coral feeding opportunities due to resuspension of organic material from the sea bed due to turbulence.

In conclusion, we find that the Binned Drake method yields better results by virtue of having smaller error bars on the fits of $u_*$ versus speed compared to the All Data Binned method, and showed a more appreciable difference between Coral and Mud Site $u_*$ values at low speeds, albeit still the same within error. As for bottom roughness parameters, the All Data Binned method presents a more interesting scenario since it appears to show more static and very small $z_o$ values (error bars are also very small) at the Mud Site compared to larger $z_o$ values at the Coral Site (larger error bars). Additionally, we conclude that the Binned Drake method is favourable in terms of speed profile comparisons, since it shows lower speeds at Coral Site compared to the Mud Site, closer to the bottom, which is consistent with an increase in drag caused by the presence of coral colonies, the caveat being that the All Data Binned method has tighter error bars.

The backscatter intensity as a function of speed for both sites was examined, in addition to the law of the wall approach and fits of friction velocity versus speed. As flow speeds increase, turbulence is expected to increase. Increased turbulence can lead to an increase in resuspension of material from the sea bed into the water column, which would be indicated in the data as an increase in backscatter intensity. Normalized backscatter values as a function of speed (Figure 5.1) increased faster at the Mud Site relative to the Coral Site for speeds between 2.5 and 7 cm $s^{-1}$, which is consistent with the results of the log liner regressions (Figure 4.27) where friction velocity increases faster at the Mud Site. Backscatter results from both locations suggest increased resuspension of material as speeds increase, as expected, up to 7 cm $s^{-1}$. It is impossible to make relative absolute comparisons between the two sites in the absence of calibrated backscatter values.

Events occurring above 7 cm $s^{-1}$ show a dramatic increase in backscatter intensity at the Coral Site, and a similar decrease in intensity at the Mud Site. The reason for

this change in trend is unclear. Possible causes include a transition into a different flow regime whereby increased flow speeds interact favourably with the rough topography of the Coral Thicket, enhancing turbulence and increasing the resuspension of material from the seabed. Alternatively, the results could be due to the low number of data points available for averaging at the two points above 7 cm $s^{-1}$ at both sites. As well, this trend is not reflected in the log linear regression technique results. However, the data used in the backscatter versus speed analysis is subject to less overall data averaging or processing, compared to the log linear approach, which makes us more confident that the result was actually observed and not an artifact of data processing.

The areas in Haddock Channel involved in this study were considered good representations of cold water coral habitat. It is possible that the control site had previously experienced bottom trawling thereby creating an area of coral habitat devoid of coral, given the close proximity of the coral thicket involved in the study. The area of coral habitat in Haddock Channel was characterized as a low speed current regime. An area with higher flow speeds would provide a different environment in which to characterize the response and interaction of rough coral topography with a broader range of speeds. Additionally, a longer duration deployment would have likely meant a slower sampling rate, ironically eliminating some of the data quality issues resulting from the combination of high duty cycle and low temperature effects on the battery chemistry.

Suggestions for a follow up study involve a longer deployment and sampling of a higher energy environment. In 2010, the two Acoustic Doppler Profilers used in this study were deployed 50 meters apart in the the Gully Marine Protected Area, a well documented coral habitat, at a depth of approximately 600 m, again via the ROPOS ROV. Two weeks of data was collected, with a sampling rate of 5 minutes/profile, using fifteen 10 cm bins. Maximum observed speeds were 30 cm $s^{-1}$. Velocity profiles

were logarithmic and conformed to the law of the wall. Analysis of this data is ongoing.

# Bibliography

Armi, L., and J. Robert C. Millard (1976), The Bottom Boundary Layer of the Deep Ocean, *Journal of Geophysical Research*, *31*(27), 4983–4990.

Baillon, S., J.-F. Hamel, V. E. Wareham, and A. Mercier (2012), Deep cold-water corals as nurseries for fish larvae, *Frontiers in Ecology and the Environment*, *10*, 351356.

Baker, K. D., P. V. R. Snelgrove, and E. N. Edinger (2009), *Summary of Ongoing Coral Recruitment Experiments. In: Gilkinson, K. and Edinger, E. (Eds.), The ecology of deep-sea corals of Newfoundland and Labrador waters: biogeography, life history, biogeochemistry, and relation to fishes.*, pp. 36–38, 2830, Canadian Technical Report in Fisheries and Aquatic Sciences.

Baker, K. D., V. E. Wareham, P. V. R. Snelgrove, and E. N. E. K. D. G. R. L. Haedrich, D. A. Fifield (2012), Distributional patterns of deep-sea coral assemblages in three submarine canyons off newfoundland, canada., *Marine Ecology Progress Series*, *445*, 235–249.

Breeze, H., and D. G. Fenton (2007), Designing management measures to protect cold-water corals off nova scotia, canada, *Bull. Mar. Sci.*, *81*(S1), 123–133.

Breeze, H., D. S. Davis, M. Butler, and V. Kostlyev (1997), *Distribution and status*

*of deep sea corals off Noval Scotia.*, Marine Issues Committee Special Publication 1, Ecology Action Centre, Halifax.

Bryan, T. L., and A. Metaxas (2007), Predicting suitable habitat for deep-water gorgonian corals on the Atlantic and Pacific Continental Margins of North America, *Marine Ecology Progress Series*, *330*, 113–126.

Cacchione, D. A., and D. E. Drake (1982), Measurements of Storm-Generated Bottom Stresses on the Continental Shelf, *Journal of Geophysical Research*, *87*(C3), 1952–1960.

Cairns, S. D. (2007), Deep-water corals: an overview with special reference to diversity and distribution of deep-water scleractinian corals, *Bulletin of Marine Science*, *81*(3), 311–322.

Cheng, R. T., C.-H. Ling, J. W. Gartner, and P. F. Wang (1999), Estimates of bottom roughness length and bottom shear stress in South San Francisco Bay, California, *Journal of Geophysical Research*, *104*(C4), 7715–7728.

Cogswell, A. T., E. L. R. Kenchington, C. G. Lirette, K. MacIsaac, M. M. Best, L. I. Beazley, and J. V. (Editors) (2009), The current state of knowledge concerning the distribution of coral in the maritime provinces., *Canadian Technical Report in Fisheries and Aquatic Sciences 2855*, Science Branch, Department of Fisheries and Oceans, Government of Canada.

Costello, M. J., et al. (2005), *Role of cold-water Lophelia pertusa coral reefs as fish habitat in the NE Atlantic. In Cold-water corals and ecosystems*, pp. 771–805, Springer-Verlag, Berlin Heidelberg.

D'Asaro, E. (1982), Velocity Structure of the Benthic Ocean, *Journal of Physical Oceanography*, *12*(4), 313322.

Davies, A., G. Duineveld, M. Lavaleye, M. Bergman, and J. van Haren, H. & Roberts (2009), Downwelling and deep-water bottom currents as food supply mechanisms to the cold-water coral *Lophelia pertusa* (Scleractinia) at the Mingulay Reef Complex., *Limnology and Oceanography*, *54*(2), 620–629.

Drake, D. E., D. A. Cacchione, and W. D. Grant (1992), Shear Stress and Bed Roughness Estimates for Combined Wave and Currents Flows Over a Rippled Bed, *Journal of Geophysical Research*, *97*(C2), 2319–2326.

Duineveld, G. C. A., M. S. S. Lavaleye, M. J. N. Bergman, H. de Stiger, and F. Mienis (2007), Trophic structure of a cold-water coral mound community (Rockall Bank, NE Atlantic) in relation to the near-bottom particle supply and current regime, *Bulletin of Marine Science*, *81*(3), 449–467.

Edinger, E., K. Baker, R. Devillers, and V. Wareham (2007), *Coldwater corals in Newfoundland and Labrador waters: distribution and fisheries impacts*, WWF-Canada, , 41 p. plus enclosed map CD.

Edinger, E. N., and O. A. Sherwood (2012), Applied taphonomy of gorgonian and antipatharian corals in atlantic canada: experimental decay rates, field observations, and implications for assessing fisheries damage to deep-sea coral habitats, *N. Jb. Geol. Paläont. Abh.*, *265*(2), 199–218.

Edinger, E. N., O. A. Sherwood, D. J. W. Piper, V. E. Wareham, K. D. Baker, K. D. Gilkinson, and D. B. Scott (2011), Geological features supporting deep-sea coral habitat in Atlantic Canada, *Continental Shelf Research*, *31*(2), S69–S84.

Fogel, S., and W.-C. Dullo (2011), High-resolution water mass measurements around cold-water corals: a comparative test study between repeated Conductivity-Temperature-Depth (ctd) casts and continuous data acquisition of bottom waters from the West Florida Slope, Gulf of Mexico, *Ann. Naturhist. Mus. Wien, Serie A*, *209-224*(113).

Frechette, M., C. A. Butman, and W. R. Geyer (1989), The Importance of Boundary-Layer Flows in Supplying Phytoplankton to the Benthic Suspension Feeder, *Mytilus edulis* L., *Limnology and Oceanography*, *34*(1), 19–36.

Friewald, A., and J. M. Roberts (Eds.) (2005), *Cold-Water Corals and Ecosystems*, Springer-Verlag, Berlin Heidelberg.

Gass, S. E., and J. M. Willison (2005), *An assessment of the distribution of deep-sea corals in Atlantic Canada by using both scientific and local forms of knowledge. In Cold-water corals and ecosystems.*, pp. 223–245, Springer-Verlag, Berlin Heidelberg.

Gilkinson, K., and E. N. Edinger (2009), The ecology of deep-sea corals of newfoundland and labrador waters: biogeography, life history, biogeochemistry, and relation to fishes., *Canadian Technical Report in Fisheries and Aquatic Sciences 2830*.

Grant, W. D., and O. S. Madsen (1979), Combined Wave and Current Interaction with a Rough Bottom, *Journal of Geophysical Research*, *84*(C4).

Grant, W. D., and O. S. Madsen (1982), Moveable Bed Roughness in Unsteady Oscillatory Flow, *Journal of Geophysical Research*, *87*(C1).

Grant, W. D., and O. S. Madsen (1986), The Continential-Shelf Bottom Boundary Layer, *Annual Reviews Fluid Mechanics*, *18*.

Grant, W. D., A. J. W. III, and S. M. Glenn (1984), Botom Stress Estimates and their Prediction on the Northern California Continental Shelf during CODE-1: The Importance of Wave-Current Interaction, *Journal of Physical Oceanography*, *14*(3).

Gross, T. F., and A. R. M. Nowell (1983), Mean flow turbulence scaling in a tidal boundary layer, *Continential Shelf Research*, *2*(2).

Guihen, D., M. White, and T. Lundälv (2013), Boundary layer flow dynamics at a cold-water coral reef, *Journal of Sea Research*, *78*, 36–44.

Hall-Spencer, J., V. Allain, and J. H. Fossa (2002), Trawling damage to northeast atlantic ancient coral reefs, *Proceedings of the Royal Society London B: Biological Sciences*, *269*(1490), 507–511.

Henry, L. A., and J. M. Roberts (2007), Biodiversity and ecological compsition of macrobenths on cold-water coral mounds and adjacent off-mound habitat in the bathyal porcupine seabight, ne atlantic, *Deep-Sea Research*, *54*(4), 654–672.

Khripounoff, A., J.-C. Caprais, J. L. Bruchec, P. Rodier, P. Noel, and C. Cathalot (), Deep cold-water coral ecosystems in the Brittany submarine canyons (Northeast Atlantic.

Kundu, P. K., and I. M. Cohen (2004), *Fluid Mechanics*, third edition ed., Elsevier Academic Press, San Diego, California, USA.

Lacy, J. R., and C. R. Sherwood (2004), Accuracy of a pulse-coherent acoustic doppler profiler in a wave-dominated flow, *Journal of Atmospheric and Oceanic Technology*.

Lavaleye, M., G. Duinveld, T. Lundalv, M. White, D. Guihen, K. Kiriakoulakis, and G. A. Wolff (2009), Cold-water corals on the tisler reef: Preliminary observations on the dynamic reef environment, *Oceanography*, *22*(1), 76–84.

Lohrmann, A. (2001), Monitoring sediment concentration with acoustic backscattering instruments, *Nortek Technical Note TN-003*, Nortek AS.

Medwin, H., and C. S. Clay (1998), *Fundamentals of Acoustical Oceanography*, illustrated ed., Academic Press.

Metaxas, A., and J. E. Davis (2005), Megafauna associated with assemblages of deep-water corals on teh scotian slope, *J. Mar. Biol. Assoc. U.K.*, *85*(6), 1381–1390.

Mills, M. M., and K. P. Sebens (2004), Ingestion and assimilation of nitrogen from benthic sediments by three specied of coral, *Marine Biology*, *145*(6), 1097–1106.

Monismith, S. G. (2007), Hydrodynamics of coral reefs, *Annual Review of Fluid Mechanics*, *39*, 37–55.

Mortensen, P. B., and L. Buhl-Mortensen (2004), Distribution of deep-water gorgonian corals in relation to benthic habitat freatures in the northeast channel (atlantic canada), *Marine Biology*, *144*(6), 1223–1238.

Mortensen, P. B., and L. Buhl-Mortensen (2005a), *Deep-water corals and their habitat in The Gully, a submarine canyon off Atlantic Canada In Cold-water corals and ecosystems.*, pp. 223–245, Springer-Verlag, Berlin Heidelberg.

Mortensen, P. B., and L. Buhl-Mortensen (2005b), Morphology and growth of the deep-water gorgonians *Primnoa resedaeformis* and *Paragorgia arborea*, *Marine Biology*, *147*(3), 775–788.

Press, W., B. Flannery, S. Teukolsky, and W. Vetterling (1986), *Numerical Recipes, The Art of Scientific Computing*, Cambridge University Press.

Reidenbach, M. A. (2004), Boundary layer dynamics in coral reef systems, Department of civil and environmental engineering, Stanford University.

Reidenbach, M. A., S. G. Monismith, J. R. Koseff, G. Yahel, and A. Genin (2006a), Boundary layer turbulence and flow structure over a fringing coral reef, *Limnology and Oceanography*, *51*(5), 1956–1968.

Reidenbach, M. A., J. R. Koseff, S. G. Monismilth, J. V. Steinbuck, , and A. Genin (2006b), The effects of waves and morphology on mass transfer within branched reef coral, *Limnology and Oceanography*, *51*(2), 1134–1141.

Reidenbach, M. A., J. R. Koseff, and S. G. Monismith (2007), Laboratory experiments of fine-scale mixing and mass transport within a coral canopy, *Physics of Fluids*, *19*(075107).

Reidenbach, M. A., J. R. Koseff, and M. A. R. Koehl (2009), Hydrodynamics forces on larvae affect their settlement on coral reefs in turbulent, wave-driven flow, *Limnology and Oceanography*, *54*(1).

Ribes, M., and M. J. Atkinson (2007), Effects of water velocity on picoplankton uptake by coral reef communities, *Coral Reefs*, *26*(2), 413–421.

Roberts, J. M., A. Wheeler, A. Freiwald, and S. D. Cairns (2009), *Cold-water Corals: The Biology and Geology of Deep-sea Coral Habitats*, Cambridge University Press.

Sebens, K. P., B. Helmuth, E. Carrington, and B. Agius (2003), Effects of water flow on growth and energetics of the scleractianian coral *Agaricia tenuifolia* in Belize, *Coral Reefs*, *22*(1), 35–47.

Sherwood, O. A., and E. N. Edinger (2009), Ages and growth rates of some deep-sea gorgonian and antipatharian corals of newfoundland and labrador, *Canadian Journal of Fisheries and Aquatic Sciences*, *66*(1), 142–152.

Sherwood, O. A., R. E. Jamieson, E. N. Edinger, and V. E. Wareham (2008), Stable c and n isotopic composition of cold-water corals from the newfoundland and labrador continental slope: Examination of trophic, depth and spatial effects., *Deep Sea Research I*, *55*(10), 1392–1402.

Wareham, V. E. (2009), *Updates on deep-sea coral distribution in Newfoundland, Labrador, and the Artic regions, Northwest Atlantic. In: Gilkinson, K. and Edinger, E. (Eds.), The ecology of deep-sea corals of Newfoundland and Labrador waters: biogeography, life history, biogeochemistry, and relation to fishes.*, pp. 4–22, 2830, Canadian Technical Report in Fisheries and Aquatic Sciences.

Wareham, V. E., and E. N. Edinger (2007), Distribution of deep-sea corals in the Newfoundland and Labrador region, Northwest Atlantic Ocean, *Bulletin of Marine Science*, *81*(supplement 1), 289–313.

Wheeler, A. J., M. Kozachenko, D. G. Masson, and V. A. I. Huvenne (2008), Influence of benthic sediment transport on cold-water coral bank morphology and growth: the example of the Darwin Mounds, north-east Atlantic, *Sedimentology*, *55*(6), 1875–1887.

White, M. (1994), Tidal and subtidal variability in the sloping benthic boundary layer, *Journal of Geophysical Research*, *99*(C4), 7851–7864.

White, M. (2007), Benthic dynamics at the carbonate mound regions of the Porcupine Sea Bight continental margin., *International Journal of Earth Sciences*, *96*(1), 1–9.

White, M., C. Mohn, H. de Stigter, and G. Mottram (2005), *Deep-water coral development as a function of the hydrodynamic and surface productivity around the submarine banks of the Rockall Trough, NE Atlantic. In Cold-water corals and ecosystems*, pp. 503–514, Springer-Verlag, Berlin Heidelberg.

White, M., J. Roberts, , and T. van Weering (2007), Do bottom-intensified diurnal tidal currents shape the alignment of carbonate mounds in the NE Atlantic?, *Geo-Marine Letters*, *27*(6), 391–397.